Carbon nanotubes for nanoscale electronics and nanoelectromechanical systems

by

Thomas David Yuzvinsky

B.A. (University of California, Berkeley) 2001
M.A. (University of California, Berkeley) 2003

A dissertation submitted in partial satisfaction of the

requirements for the degree of

Doctor of Philosophy

in

Physics

and the Designated Emphasis

in

Nanoscale Science and Engineering

in the

Graduate Division

of the

University of California, Berkeley

Committee in charge:

Professor Alex Zettl, Chair
Professor Steven G. Louie
Professor Kristofer S. J. Pister

Fall 2006

The dissertation of Thomas David Yuzvinsky is approved:

Chair Date

Date

Date

University of California, Berkeley

Fall 2006

Carbon nanotubes for nanoscale electronics

and nanoelectromechanical systems

by

Thomas David Yuzvinsky

Abstract

Carbon nanotubes for nanoscale electronics

and nanoelectromechanical systems

by

Thomas David Yuzvinsky

Doctor of Philosophy in Physics

University of California, Berkeley

Professor Alex Zettl, Chair

This dissertation describes our experimental studies of the electronic and mechanical properties of carbon nanotubes. To obtain repeatable results from these very small structures, we have fabricated electronic and electromechanical devices which can then be tested in controlled environments. We correlate measurements performed on these devices with nanotube structure through simultaneous high resolution electron microscopy. Our measurements reveal valuable insights into both the nature of electronic conduction in multiwalled carbon nanotubes and their dynamic, mechanical bearing structure. Finally, by studying the fabrication processes themselves, we have developed numerous techniques to manipulate and modify individual carbon nanotubes, including methods to attach, clean, cut, shrink, peel, and place carbon nanotubes in specific locations and orientations.

Professor Alex Zettl
Dissertation Committee Chair

To my parents.

Contents

List of Figures **v**

I Introduction and Background **1**

1 Carbon Nanotubes **2**
1.1 Introduction . . . 2
1.2 Physical properties of carbon nanotubes . . . 3
1.2.1 Structure and geometry . . . 3
1.2.2 Mechanical properties . . . 4
1.2.3 Electronic properties . . . 6
1.2.4 Electronic transport . . . 11
1.3 Applications of carbon nanotubes . . . 14

II Nanotube modification **16**

2 Removing individual shells of multiwalled carbon nanotubes **17**
2.1 Introduction . . . 17
2.2 Electron transparent devices . . . 18
2.3 *In situ* observation of electrical breakdown . . . 20
2.4 Transport data and analysis . . . 26
2.4.1 Evaluation of existing models . . . 26
2.4.2 Lathe model . . . 27
2.5 Breakdown in air . . . 28

3 Shrinking carbon nanotubes **30**
3.1 Introduction . . . 30
3.2 Shrinking process . . . 31
3.3 Mass loss analysis . . . 35
3.4 Control of shrinking process . . . 35
3.5 Electronic characterization . . . 37
3.5.1 Resistance measurements . . . 37
3.5.2 Lathe model . . . 38

3.6 Zero diameter limit . . . 40
3.6.1 Atomic carbon chains and negative differential resistance . . . 41

4 Precise cutting of nanotubes with a low-energy electron beam 44
4.1 Introduction . . . 44
4.2 Cutting nanotubes . . . 45
4.3 Other cutting methods and their drawbacks . . . 45
4.4 Cutting process . . . 46
4.5 Analysis and physical processes . . . 48

III Device integration 54

5 Nanotube nanomotor 55
5.1 Multiwalled carbon nanotube bearings . . . 55
5.2 Nanoelectromechanical systems . . . 56
5.3 Nanomotor design and fabrication . . . 57
5.3.1 Architecture . . . 57
5.3.2 Fabrication process . . . 58
5.4 Operation and characterization . . . 60
5.4.1 Initial bearing release . . . 60
5.4.2 DC stepping . . . 64
5.4.3 AC driving . . . 64
5.5 Other methods for bearing release . . . 67
5.5.1 Electrically driven vaporization . . . 68
5.5.2 Reactive ion etching . . . 72
5.5.3 Mechanical shearing . . . 75
5.5.4 Electron beam cutting . . . 76

6 Highly aligned nanotube arrays for large scale device fabrication 77
6.1 Introduction . . . 77
6.2 Existing methods and their limitations . . . 78
6.2.1 Chemical vapor deposition . . . 78
6.2.2 Fluidic techniques . . . 78
6.3 Fabrication process . . . 79
6.3.1 Overview . . . 79
6.3.2 Alignment . . . 80
6.3.3 Localized deposition . . . 83
6.3.4 Array fabrication . . . 87
6.4 Conclusions . . . 88

7 Manipulation of individual nanotubes 89
7.1 Introduction . . . 89
7.2 Atomic force microscopy probes . . . 90
7.2.1 Fabrication of nanotube-tipped probes . . . 91
7.2.2 Characterization of nanotube-tipped AFM probes . . . 94
7.3 Scanning tunneling microscopy probes . . . 94

7.4 Manipulation and integration of individual nanotubes into prefabricated devices 97

Bibliography **100**

A Acronyms and Chemical Names **109**

B Nanomanipulator **111**

B.1 Nanomanipulator Design 111

B.1.1 Overview 112

B.1.2 Main stage elements 113

B.1.3 Sample holders 116

B.1.4 AFM and STM tip holders 120

B.1.5 Dovetail 123

List of Figures

1.1 Conceptual formation of a carbon nanotube from a graphene sheet 4
1.2 Plot of the dispersion relation for a single graphene sheet 6
1.3 Dispersion relation and density of states of graphene near the K points . . . 7
1.4 Chiral vector $\mathbf{C_h}$ of a carbon nanotube 9
1.5 The quantization of allowed $\mathbf{k}$ vectors in a carbon nanotube 10
1.6 Armchair and zigzag nanotubes 11

2.1 TEM transparent membranes for in situ transport measurements 19
2.2 TEM micrographs showing the time evolution of a MWCNT device 21
2.3 TEM micrographs of contact erosion during device operation 23
2.4 Wall-by-wall breakdown of a MWCNT 25
2.5 TEM micrographs and current vs. time for nanotube breakdown in air . . . 28

3.1 Illustration of the shrinking process 31
3.2 TEM micrographs of a nanotube undergoing the shrinking process 33
3.3 Diameter control of a carbon nanotube 36
3.4 Calculated and measured resistance of the shrinking CNT vs. time 38
3.5 Calculated resistance vs. measured resistance of the CNT 40
3.6 Current-voltage characteristics of the nanotube device 42
3.7 Theoretical calculation of I-V characteristics for a C_4 atomic wire 43

4.1 TEM micrographs of a nanotube before and after cutting 48
4.2 Plot of cutting time vs. atmosphere 49
4.3 Plot of cutting time vs. beam current and atmosphere 52
4.4 Plot of cutting time vs. acceleration voltage 53

5.1 A silicon-based microelectromechanical motor 56
5.2 Conceptual drawing of nanotube rotational actuator 58
5.3 Nanomotor fabrication process 59
5.4 SEM micrograph of nanotube rotational actuator 60
5.5 Calculated electric fields in the vicinity of the nanomotor device 62
5.6 Deflection vs. gate voltage for consecutive runs 63
5.7 SEM micrographs of a nanomotor at different angular displacements 65
5.8 SEM micrographs of a rapidly driven nanomotor device 66

5.9 Temporary metal bridge for symmetric wall-by-wall breakdown 70
5.10 Telescopic failure of a nanomotor device after wall-by-wall breakdown . . . 71
5.11 SEM micrographs of a nanomotor treated by reactive ion etching 73
5.12 Model of bearing creation by various methods 74
5.13 SEM micrographs of mechanical deflection prior to bearing release 75
5.14 A nanomotor device after being cut by the SEM electron beam 76

6.1 Array fabrication process 80
6.2 An array of nanotube devices 81
6.3 Fluidic alignment of nanotubes by spinning the substrate 82
6.4 Electron beam activated controlled deposition of nanotubes 84

7.1 SEM micrograph of an AFM tip next to a nanotube-coated razor blade . . 91
7.2 SEM micrographs of a partially cut carbon nanotube severed by tensile stress 93
7.3 SEM micrographs of nanotube-tipped AFM tips of varying length 95
7.4 Nanotube-tipped AFM images of double-stranded DNA on mica 96
7.5 TEM micrograph of a nanotube-tipped STM probe 97
7.6 SEM micrograph of a nanotube placed on a microfabricated thermal test fixture 99

B.1 Overview of the assembled nanomanipulator 112
B.2 Schematic drawing of the main body of the nanomanipulator stage 113
B.3 Schematic drawing of the “S”-stage 114
B.4 Schematic drawing of the “Z-stop” 115
B.5 Schematic drawing of the DIP connector 116
B.6 Schematic drawing of the Vespel DIP socket 117
B.7 Schematic drawing of the PLCC connector 118
B.8 Schematic drawing of the stand-alone stage 119
B.9 Schematic drawing of the standard AFM tip holder 120
B.10 Schematic drawing of the inverted AFM tip holder 121
B.11 Schematic drawing of the STM tip holder 122
B.12 Overview of the Dovetail assembly 123
B.13 Schematic drawing of the Dovetail slot 124
B.14 Schematic drawings of Dovetail slot modifications for spring-retention system 125
B.15 Schematic drawings of Dovetail accessories. 126
B.16 Schematic drawing of the Dovetail slide for the Nanomanipulator 127
B.17 Schematic drawing of the Dovetail slide for SEM accessories 128

Acknowledgments

First and foremost, I would like to thank my research advisor, Alex Zettl, for his unending support and encouragement. Alex is an excellent teacher and his dedication to his students is rivaled only by his skill as a white water guide. I feel very fortunate to have been able to work with him for the past five years.

I am grateful to Mike Crommie for many enlightening conversations since my undergraduate days and for chairing my qualifying exam committee. Likewise, I greatly appreciate the time and effort that Steven Louie and Kris Pister have devoted to my research by being on both my qualifying exam and dissertation committees.

Many thanks to the past and present members of the Zettl Group with whom I have worked, including Willi Mickelson, Gavi Begtrup, Shaul Aloni, Chris Regan, Kenny Jensen, Andras Kis, Steve Konsek, Cristian Esquivias, Weiqiang Han, Noah Bodzin, Haibing Peng, Henry Garcia, Brian Kessler, Masa Ishigami, Andrei Afansiev, and anybody else I may have forgotten. Most of all, I am indebted to Adam Fennimore, who taught me much of what I know and was always a pleasure to work with. I wish him and his rapidly growing family all the best.

Most of my research would not have been possible without the expertise (and hard labor) provided by the Physics Department Machine Shop. I would especially like to thank Marco Ambrosini, Dave Murai, Pete Thuesen, Steve Butler, Abel Gonzalez, Dave Nguyen, and George Weber for their assistance in designing and machining countless gadgets over the years. Thanks also to Joseph Kant, whose patient instruction enabled me to machine many of the parts myself.

David Gallegos and LeVern Garner of the Electronics Shop always went out of

their to way to help me with any questions I might have. Thanks to Ron Wyckoff for fixing whatever electronics I managed to break, and to John Davis for teaching the summer electronics course.

A big thank you to Anne Takizawa, Claudia Trujillo, and Donna Sakima for always being helpful and knowing the answers to seemingly everything. Thanks also to the support and purchasing staff (Eleanor Crump, Katalin Markus, Lynne Pelosi, Anthony Vitan, Caroline Day, Gretchen Sanderson, Davina Abram, and Rosemary Williams), who play a vital role in our research programs but too often only get noticed when something goes wrong.

Finally, my deepest gratitude to Olya, who inspired,
encouraged, and challenged me every step of the way.

Part I

Introduction and Background

Chapter 1

Carbon Nanotubes

1.1 Introduction

Carbon nanotubes [1] have fascinating physical properties. They possess an extremely high strength-to-weight ratio, exhibit exceptional thermal conductivity, and, extraordinarily, their intrinsic electronic structure can be either semiconducting or metallic. Perhaps most exciting is that each of these properties can be tuned by appropriate chemical or structural modifications.

These unique features have fueled an immense effort into the study of carbon nanotubes over the past fifteen years. Many important questions have been answered, but there are still several fundamental gaps in our understanding of carbon nanotube physics. For example, both the nature and distribution of electrical current through a multiwalled carbon nanotube are hotly debated and widely varying theories have been proposed. Much of the controversy arises from the difficulty of obtaining consistent results when working with nanometer-scale structures.

In an attempt to address these questions, we have fabricated electronic and electromechanical devices which we then test in controlled environments. By performing simultaneous, high resolution electron microscopy, we are able to correlate measurements performed on these devices with nanotube structure. Our measurements reveal valuable insights into both the nature of electronic conduction in multiwalled carbon nanotubes and their dynamic, mechanical bearing structure. In addition, by studying the interaction of carbon nanotubes with focused electron beams, we have identified the distinct physical mechanisms responsible for low energy beam damage and high energy structural reformation. Armed with this new knowledge, we have developed methods to precisely tailor the physical properties of carbon nanotubes, both for a wide variety of technological applications and for further experiments in nanoscale physics.

1.2 Physical properties of carbon nanotubes

1.2.1 Structure and geometry

Carbon nanotubes are hollow, nanometer-scale tubes composed of carbon atoms bonded together in a hexagonal sp^2 configuration. They are chemically similar to other sp^2-bonded allotropes of carbon, such as fullerenes and graphene. Indeed, in calculations of physical properties, it is often useful to think of a single-walled carbon nanotube as a single graphene sheet rolled up into a tube (see Figure 1.1).

Typical outer diameters of single-walled carbon nanotubes are 1 to 2 nm, although they can range from as small as 4 Å to 10 nm or greater. There does not appear to be any fundamental limit on the length of carbon nanotubes, with recent measurements of single-walled nanotubes synthesized by a catalytic chemical vapor deposition (CVD)

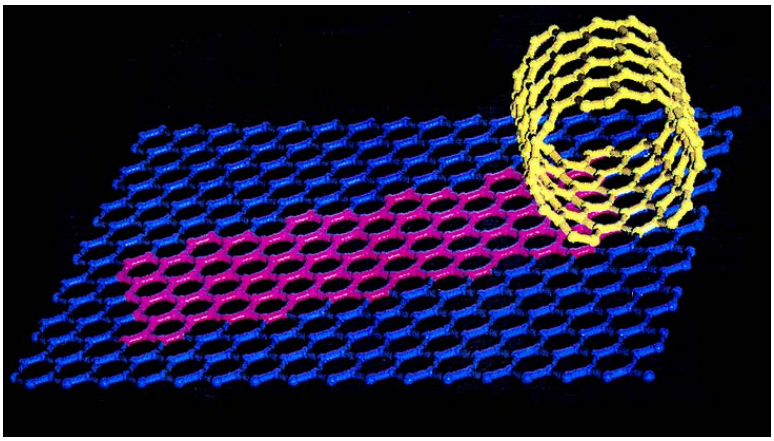

Figure 1.1: Conceptual formation of a carbon nanotube from a graphene sheet.

method reporting lengths in excess of 4 cm [2]. These long lengths, however, have only been obtained by the CVD synthesis process: the typical lengths of nanotubes grown by other methods, such as electric arc discharge [3] or laser ablation [4], are generally limited to several microns.

Just as multiple layered sheets of graphene comprise a single crystal of graphite, multiple coaxially nested single-walled carbon nanotubes comprise a single multiwalled carbon nanotube. As in graphite, the bonding between layers in multiwalled carbon nanotubes is due to van der Walls interactions and exhibits similar layer spacing (~ 3.4 Å). The outer diameter of a multiwalled carbon nanotube depends in part on how many layers it has and can vary greatly. The highest quality multiwalled carbon nanotubes are produced by electric arc discharge and generally have diameters in the tens of nanometers.

1.2.2 Mechanical properties

Due to their network of carbon-carbon sp^2 bonds, carbon nanotubes are extremely stiff and strong.[†] They have a Young's modulus on the order of 1 TPa, and a tensile

[†]The sp^2 bonds in graphite are stronger than the sp^3 bonds in diamond. Graphite appears softer than diamond only because the c-axis van der Walls bonds between graphene sheets are easy to overcome.

strength of approximately 100 GPa, making them one of the strongest materials known to man. As such, carbon nanotubes are an ideal candidate for use as reinforcement material and have been employed in various high-strength composites [6]. Their strength-to-weight ratio exceeds that of all other known materials [7].

Carbon nanotubes also have a high shear modulus, although the exact value is hard to pin down. In multiwalled nanotubes of varying quality, for example, it is not always clear to what extent individual walls interact with each other, so with different assumptions reported measurements can range from 33 GPa to over 5 TPa [8]. Using high quality nanotubes in a torsional actuator geometry, we have narrowed this range down to 100 to 300 GPa (see Chapter 5).

High quality multiwalled nanotubes, in which the interaction between neighboring shells is very weak, also exhibit a fascinating dynamic property: individual shells can be made to slide independently of each other. This effect was first reported in the creation of linear carbon nanotube bearings *in situ* in a transmission electron microscope [9]. The frictional response to such motion is negligible. Detailed molecular dynamics simulations have shown that the dissipation in an oscillating, nested nanotube linear bearing arises mainly from the discontinuities at the edges of the outer nanotube [10], and no dissipation was measured in the original experiment [9]. Following the linear bearing work, we have harnessed the unique structure of multiwalled carbon nanotubes to create rotational bearings, in which one nanotube shell rotates freely about another. These devices are described in detail in Chapter 5.

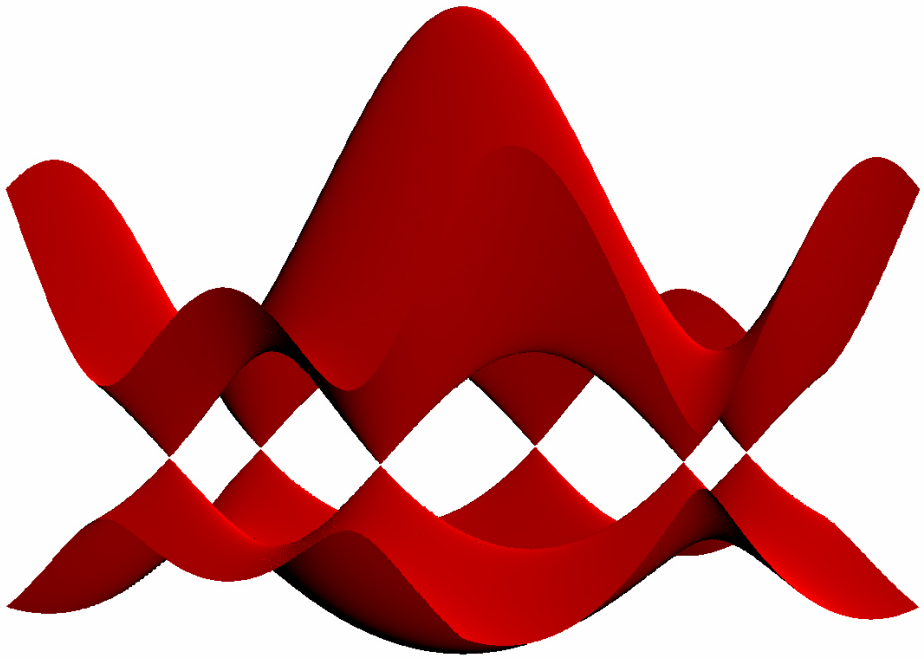

Figure 1.2: A three dimensional plot of the dispersion relation for a single sheet of graphene. The conduction band (upper half) and valence band (lower half) intersect at the six corners of the first Brillouin zone (the K points).

1.2.3 Electronic properties

Graphene

Carbon nanotubes inherit many of their electronic properties from graphene sheets. In graphene, the four valence electrons of each carbon atom form sp^2 bonds. Three valence electrons (occupying the s, p_x, and p_y orbitals) form σ bonds which hybridize to establish the hexagonal sp^2 network. The remaining valence electron occupies the p_z orbital, which is orthogonal to the hexagonal plane and forms a delocalized π bond. Because of the strong, localized nature of the σ bonds, it is the delocalized π bonds which far and away dominate electronic conduction in graphene.

The energy dispersion of a single layer of graphene can be calculated using a

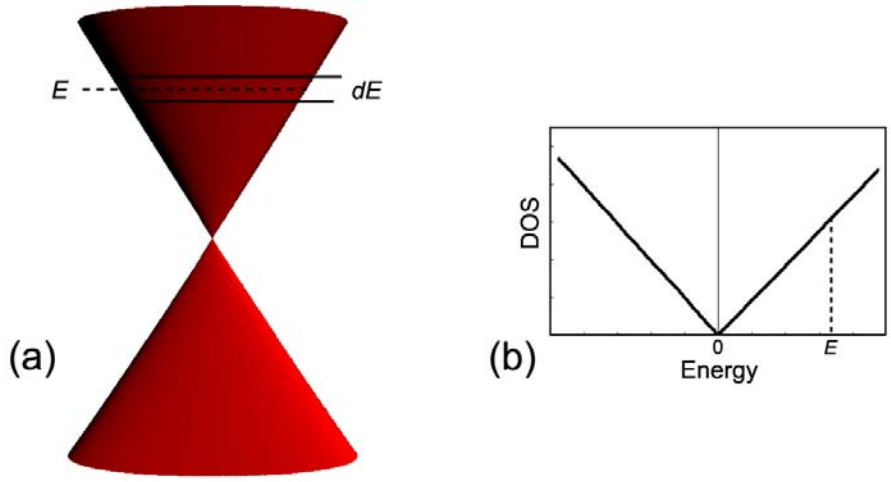

Figure 1.3: Dispersion relation (a) and density of states (b) of graphene in the vicinity of the K points.

tight-binding approximation and is shown in Figure 1.2. A simple analytic approximation (following the Slater-Koster scheme, in which the p_z orbital overlap for neighboring atoms is assumed to be zero) is given by

$$E(\mathbf{k}) = \pm t\sqrt{1 + 4\cos\left(\frac{\sqrt{3}k_x}{2}\right)\cos\left(\frac{k_y a}{2}\right) + 4\cos^2\left(\frac{k_y a}{2}\right)} \tag{1.1}$$

Figure 1.2 shows the conduction and valence bands in k (momentum) space over a region slightly larger than the first Brillouin zone. The two bands touch at six points (the K points) which are the corners of the hexagonal first Brillouin zone.[†] As Figure 1.3 (a) shows, the dispersion relation is conical near the K points, giving rise to the linear density of states (DOS) shown in Figure 1.3 (b). Since the bands touch but not overlap, and since the density of states vanishes at the K points, we deduce that a sheet of graphene will behave as a zero-gap semiconductor.

[†]Note that all six K points are not equivalent (they cannot all be connected to each other by reciprocal lattice vectors). There are in fact two distinct sets, often called K and K', each containing three equivalent points. If we allow for two spin orientations, these two sets give rise to four independent subbands.

Carbon nanotubes

While all graphene sheets of infinite extent exhibit the same electronic structure, the same cannot be said of all carbon nanotubes. Instead, the particular structure of each nanotube (as indexed by its chiral vector) determines its electronic properties. The chiral vector of a nanotube is simplest to define in reference to the imaginary graphene sheet from which the nanotube was rolled: it is the vector that connects one point on the edge of the sheet to the matching point on the opposite edge, such that those two points coincide when the sheet is rolled up (see Figure 1.4). The lattice vectors of the graphene sheet ($\hat{\mathbf{a}}_1$ and $\hat{\mathbf{a}}_2$) are used as a basis for the chiral vector $\mathbf{C}_h$, which is usually denoted $\mathbf{C}_h = n\hat{\mathbf{a}}_1 + m\hat{\mathbf{a}}_2$ or simply (n, m). Since, when the sheet is rolled up, an atom on one edge must be mapped onto the position of an atom on the other edge (as otherwise the nanotube could not be continuous), n and m must have integer values.

Rolling the imaginary sheet of graphene into a nanotube introduces two important corrections to its electronic properties. The first is quantization of the allowed $k_\perp$ values (where $k_\perp$ is the component of electron momentum $\mathbf{k}$ perpendicular to the nanotube axis and $k_\parallel$ is the component parallel to the axis). Since the wavefunction of an electron in the nanotube must be single-valued upon going once around the circumference, only those $\mathbf{k}$ that satisfy $k_\perp \pi d = 2\pi q$ (where q is an integer) are allowed.[†] The chiral vector determines which $k_\perp$ are allowed, and, in particular, whether or not the K points are accessible (see Figure 1.5). If no allowed $\mathbf{k}$ value coincides with the K points, then the dispersion relation of the nanotube will have a gap around zero energy, and the nanotube will be semiconducting.

[†]So much is true for a nanotube of infinite length. If the length is finite, quantization of $k_\parallel$ is introduced as well. This quantization is usually negligible due to the high aspect ratio of most nanotubes, but can become important at short lengths or very low temperatures.

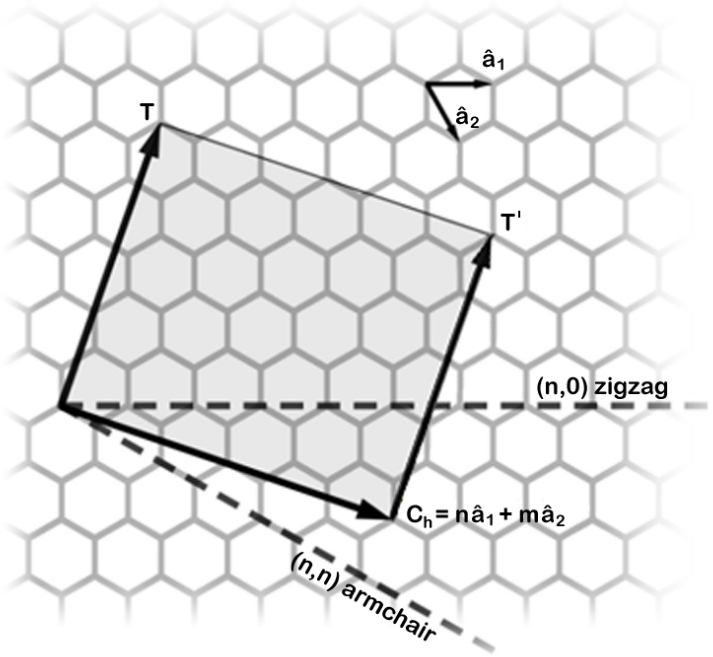

Figure 1.4: The chiral vector $\mathbf{C_h}$ of a nanotube as shown on an unrolled graphene sheet. The perpendicular vectors $\mathbf{T}$ and $\mathbf{T}'$ point in the axial direction and coincide on the rolled-up nanotube. The shaded area indicates the unit cell of the nanotube and can be repeated along the axial direction to form a nanotube of arbitrary length. The dashed lines indicate the directions the chiral vector would follow in a zigzag $(n, 0)$ or armchair (n, n) nanotube, in which cases $\mathbf{T}$ and $\mathbf{T}'$ would point in the corresponding perpendicular directions.

On the other hand, if the K points are accessible, the nanotube will be metallic. The band gap of semiconducting nanotubes varies inversely with diameter, with $E_g = 0.9\ eV/(d\ [nm])$ [11].

(Unlike graphene, which is a zero-gap semiconductor, metallic nanotubes have a non-zero density of states at zero energy. We demonstrate this by examining the limit as energy approaches zero. In graphene, the $\mathbf{k}$ states available within a range dE of energy E are located within a ring of height dE on the conical dispersion relation (see Figure 1.3). As the energy E is shifted towards zero, the ring slides down towards the apex of the cone, and the area contained on the surface of the ring (and the number of available states)

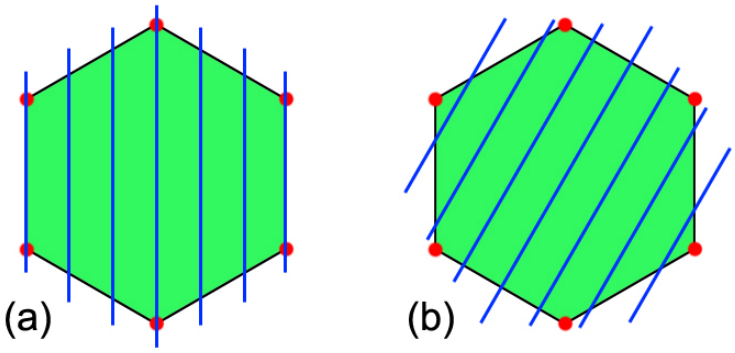

Figure 1.5: The quantization of allowed **k** vectors in a carbon nanotube. The green area is the first Brillouin zone of graphene, with K points labeled in red. The blue lines identify the **k** vectors allowed in a carbon nanotube, which are restricted by the quantization of $k_\perp$. Depending upon the chiral vector of the nanotube, the K points can either be (**a**) accessible, yielding a metallic nanotube, or (**b**) inaccessible, yielding a semiconducting nanotube.

shrinks to zero. For metallic nanotubes, the dispersion relation is obtained by taking the vertical cross-section through the origin of graphene's conical dispersion relation, yielding two straight lines that cross at zero energy. The states available within a range dE of energy E are contained within two short line segments of height dE. The length of these line segments stays constant as the energy E is shifted towards zero. Thus, the number of states stays constant and is nonzero at zero energy.)

The determination of which indices correspond to metallic or semiconducting nanotubes is not hard to derive. Another way to write the momentum quantization constraint mentioned above is $\mathbf{C_h} \cdot \mathbf{k} = 2\pi q$, where q is an integer. Substituting in the **k** vector of the point of intersection between valence and conduction bands (use, for example, the K' point at $\frac{\mathbf{b_1}-\mathbf{b_2}}{3}$) immediately yields $n-m = 3q$. Thus we have a surprisingly simple selection rule: an (n, m) nanotube is metallic if $n - m$ is a multiple of 3; otherwise, it is semiconducting. In particular, all (n, n) nanotubes (known as "armchair" nanotubes because the shape of an armchair can be reproduced by tracing the bond lines about the circumference) and one

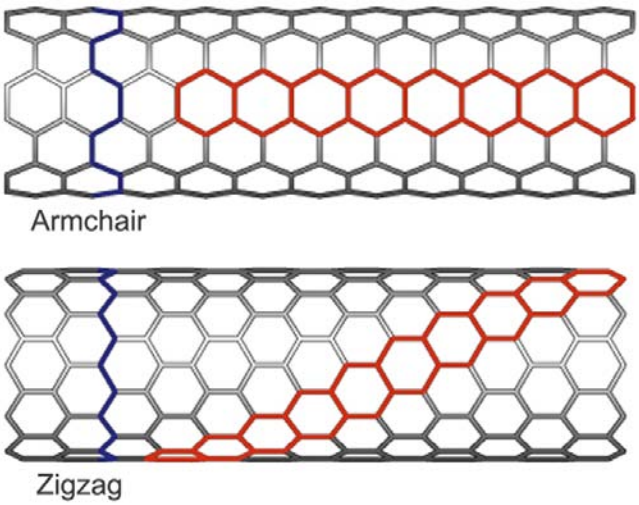

Figure 1.6: Examples of armchair and zigzag nanotubes. Adapted from [12].

third of all $(n, 0)$ nanotubes (known as "zigzag" nanotubes for a similar reason) are metallic.

The second correction induced by rolling up a graphene sheet is due to the non-zero curvature. Curvature induces a change in the overlap integrals between p_z orbitals, with small band gaps (scaling as $1/d^2$) predicted to appear in non-armchair metallic nanotubes[13]. This effect only appears in small-diameter (high-curvature) nanotubes, however, and even then plays an important role only at low temperatures and biases.

1.2.4 Electronic transport

Metallic single-walled carbon nanotubes

Metallic single-walled carbon nanotubes can be either ballistic or diffusive conductors, depending upon the length of the nanotube in question and its effective mean free path. At low bias ($\leq$ 0.2 V), the scattering is believed to be caused by absorption and emission of low-energy acoustic phonons, and can yield mean free paths as long as several microns at room temperature [11]. Thus, the low bias resistance of short, high quality

nanotube segments is entirely due to the quantized conductance of ballistic channels (plus any additional contact resistance). From the Landauer formalism we know that a single ballistic channel has conductance equal to $e^2/h = 38.7\ mS$. Nanotubes have four conducting subbands (two for spin degeneracy, two for K and K' degeneracy), so their fundamental resistance should be 6.45 kΩ. Actual measured values are generally higher due to imperfect contacts, which makes it difficult to determine the quality of a nanotube solely from electronic measurements.

At higher biases of several volts, the current in a substrate-bound metallic nanotube is found to saturate at approximately 25 μA. This saturation is believed to be due to scattering of electrons by the emission of high-energy optical or zone-boundary phonons [14]. In suspended nanotubes, electronic transport saturates at a lower bias due to the lack of optical phonon relaxation and heat dissipation that a substrate provides. Suspended nanotubes can even exhibit negative differential resistance (NDR) [15]. The observation of NDR raises the tantalizing possibility of electronic oscillators and more complex circuits fabricated out of single nanotubes.

In either case, increasing the applied bias further eventually causes failure of the metallic nanotube. This provides a simple way to remove the metallic nanotubes from a mixed sample when only semiconducting nanotubes are desired [16]. Nonetheless, before failure, metallic nanotubes have been reported to carry current densities as high as $10^9\ A/cm^2$, orders of magnitude larger than the current densities found in present-day interconnects [11].

Semiconducting single-walled carbon nanotubes

Semiconducting single-walled nanotubes behave quite differently from metallic nanotubes. While metallic nanotube conduction is not strongly affected by electrical or chemical gating, the conductivity of semiconducting nanotubes can be tuned through many orders of magnitude, from nearly metallic to highly insulating. Even simple exposure to air (specifically, oxygen) can through chemical doping induce a $10 - 15\%$ change in resistance, making semiconducting nanotubes quite promising for chemical sensing applications [17].

Transport measurements on semiconducting nanotubes generally exhibit Schottky barriers due to the metal-semiconductor interfaces at the nanotube contacts. This phenomenon has been harnessed in ambipolar nanotube-based field effect transistors, which operate by modulating the size of the Schottky barriers [18]. Indeed, much effort has gone into capturing and controlling the semiconducting properties of semiconducting nanotubes, with dozens of transistors, diodes, and logic circuits reported in the literature. With recent measurements reporting the highest mobility values for any known semiconductor, in excess of $100,000\ cm^2/Vs$ at room temperature [19], this trend is likely to continue.

Multiwalled carbon nanotubes

The presence of multiple nanotubes in close contact with each other changes their individual behavior and complicates the situation dramatically. Indeed, despite the many studies of multiwalled carbon nanotubes [20, 21, 22, 16, 23, 24, 25, 26], there are still outstanding fundamental questions regarding the mode of electronic transport, the radial distribution of the current density, and the relationship between this distribution and the failure modes of multiwalled nanotubes.

Based upon conflicting measurements, several different electronic transport mechanisms for multiwalled nanotubes have been proposed. These include reports of purely diffusive conduction [27], reports of a single ballistic channel [21], and, recently, reports of several hundred ballistic channels [28]. The distribution of current among the walls is also disputed, with various reports concluding that equal amounts of current are present in each wall [23], that current is constrained to the outermost walls [26], or that current is carried solely by the outer wall [21]. It is important to note that these measurements were performed without detailed knowledge of the nanotube structure or of its contact to the measurement electrodes. As I discuss in later chapters, structural defects, surface coatings, and poor contact geometry can strongly affect the measured transport through a carbon nanotube.

To better understand the nature of electronic conduction in multiwalled carbon nanotubes, we have developed methods to precisely change their atomic structure while simultaneously performing both electronic transport measurements and high resolution transmission electron microscopy (TEM). Thus we are able to correlate changes in atomic structure with changes in electronic transport. From multiple measurements, we find that at room temperature and above, electronic conduction is diffusive and current is in fact uniformly distributed across the entire cross section of multiwalled carbon nanotubes (excluding the hollow core). These measurements are described in detail in Chapters 2 and 3.

1.3 Applications of carbon nanotubes

The carbon nanotube is perhaps the most versatile nanoscale building block discovered to date. It has been incorporated into devices ranging across multiple disciplines,

including electronic transistors [29], chemical sensors [17], mechanical memory elements [30], biological probes [31], linear bearings [9], rotational actuators [32], high frequency oscillators [8, 33], light emitting devices [34], etc. Some proposed applications are in fact so demanding (such as the super-strong, lightweight cable needed for a "space elevator" [7]) that carbon nanotubes remain the only possible material candidate.

Their widespread application is limited, however, by the difficulty of manipulating, modifying or even making contact to carbon nanotubes on an individual basis. As a result, carbon nanotubes are usually grown or deposited in bulk quantities, in the hope that some number of nanotubes with the desired diameter, length, and number of walls are ultimately located in the desired location and orientation. The subsequent integration schemes rely almost exclusively upon the parallel fabrication of many devices, which must be individually tested and reviewed for operation within desired parameters. This process also applies to many experimental studies of carbon nanotubes, adding a layer of complication and variability to experimental results.

To overcome these difficulties, over the course of our studies we have developed numerous techniques to modify and manipulate individual carbon nanotubes. These include methods to attach, clean, cut, shrink, peel, and place carbon nanotubes in specific locations and orientations. In the following chapters, along with the results of our physical measurements, I discuss these methods and their possible applications.

Part II

Nanotube modification

Chapter 2

Removing individual shells of multiwalled carbon nanotubes

2.1 Introduction

As discussed in the preceding chapter, there exist conflicting reports regarding the nature of electronic transport and the distribution of current in multiwalled carbon nanotubes (MWCNTs). This controversy is in large part due to the difficulty of measuring both the electronic transport and the geometrical structure of the same nanoscale sample. We have developed a straightforward method to simultaneously measure both properties. In addition, by performing these measurements on the same samples before and after inducing structural changes in the MWCNTs, we are able to correlate changes in structure with changes in electronic properties. In this chapter, I describe electronic measurements before, during, and after the use of electrical breakdown to remove material from the outside of MWCNTs.

MWCNTs can carry very large current densities, with maximum amounts on the order of $10^8 - 10^9 A/cm^2$. When excessive current is applied, however, the MWCNT fails in a sequential step-wise manner, increasing in resistance and getting thinner with each step [23]. While earlier studies have measured this change in resistance, they were only able to measure the outer dimensions of the MWCNT, and even then could not unequivocally identify how many shells were being removed [23, 16]. We simultaneously measure electronic transport and identify MWCNT structure with atomic precision by incorporating MWCNTs into electron transparent devices which can be imaged by transmission electron microscopy (TEM) during operation.

2.2 Electron transparent devices

Due to their thick substrate layer, standard electrically-connected device architectures do not allow electron transmission as necessary for TEM imaging. Silicon nitride (Si_3N_4) membranes, on the other hand, have been used as electron-transparent supports for TEM imaging of isolated nanostructures [35, 36, 37]. We have adapted this technique to construct electrically connected electron-transparent devices that can be operated inside a TEM.

Design and fabrication of the electron transparent membranes used in these devices was initiated by Adam Fennimore, who developed the first operational prototypes. The process has since been refined by Steve Konsek, Andras Kis, and Gavi Begtrup.

The fabrication process consists of a combination of deposition and etching processes. Initially, 500-800 nm of silicon oxide is grown on a silicon wafer, after which 10-20 nm of silicon nitride is deposited. The silicon is then selectively back-etched with KOH. The

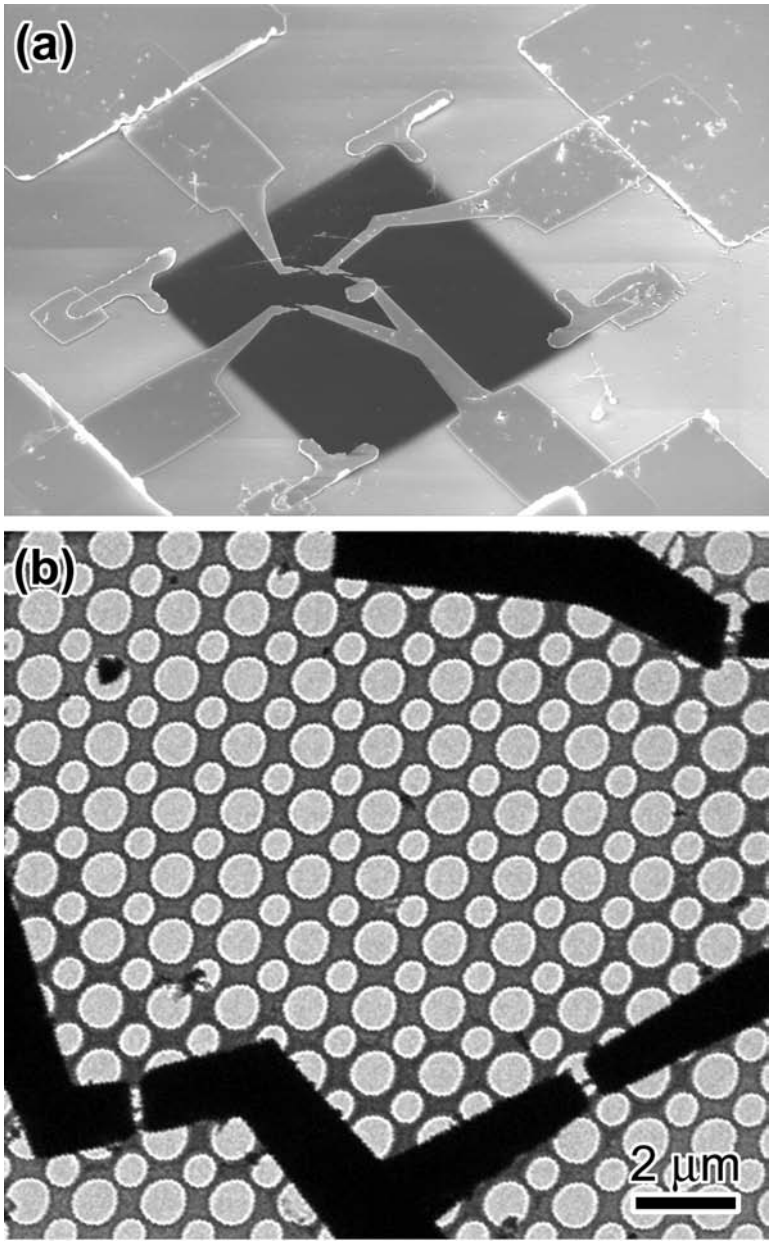

Figure 2.1: (a) An SEM image of a membrane device with several MWCNTs contacted by gold electrodes. The membrane itself is not visible in the SEM and appears black. (b) A TEM image of a membrane with three MWCNT devices indicated by arrows. A regular array of holes is pre-etched into the membrane to allow higher resolution imaging. The scale bar is 2 μm.

oxide and nitride layers are exposed to HF, which removes silicon oxide and leaves the silicon nitride intact. Nanostructures are placed on the resulting membrane and located with scanning electron microscopy (SEM). Contacts to the nanostructures are patterned by electron beam lithography and deposited via electron-beam evaporation of gold. Figure 2.1 (a) shows an SEM image of several devices. For the higher imaging resolution, holes can be etched in the membrane before the nanostructures are deposited, as shown in Figure 2.1 (b).

This device architecture provides a framework for the study of different response functions (magnetic, electronic, mechanical, chemical) of a wide variety of nanostructures.

2.3 *In situ* observation of electrical breakdown

To observe MWCNT electrical breakdown *in situ* we fabricated batches of two-contact MWCNT devices. Throughout our studies, we find that initially the MWCNT is invariably decorated with residue from the device fabrication process. This residue can be isolated surface debris, or, in extreme cases, an almost complete blanketing with gold nanoparticles. Studying the response of the device to progressively larger applied voltages, we observe cleaning of the MWCNT, annealing and erosion of the contacts, substrate alteration, and finally, failure of the MWCNT. By monitoring the electronic transport while simultaneously imaging via TEM, we are able to correlate structural modifications with changes in electronic properties.

Figure 2.2 follows a representative MWCNT device through the entire sequence of testing. As fabricated (Figure 2.2 (a)), the device is decorated with gold nanoparticles. The nanoparticle coverage on the surrounding continuous membrane serves as a useful temperature diagnostic.

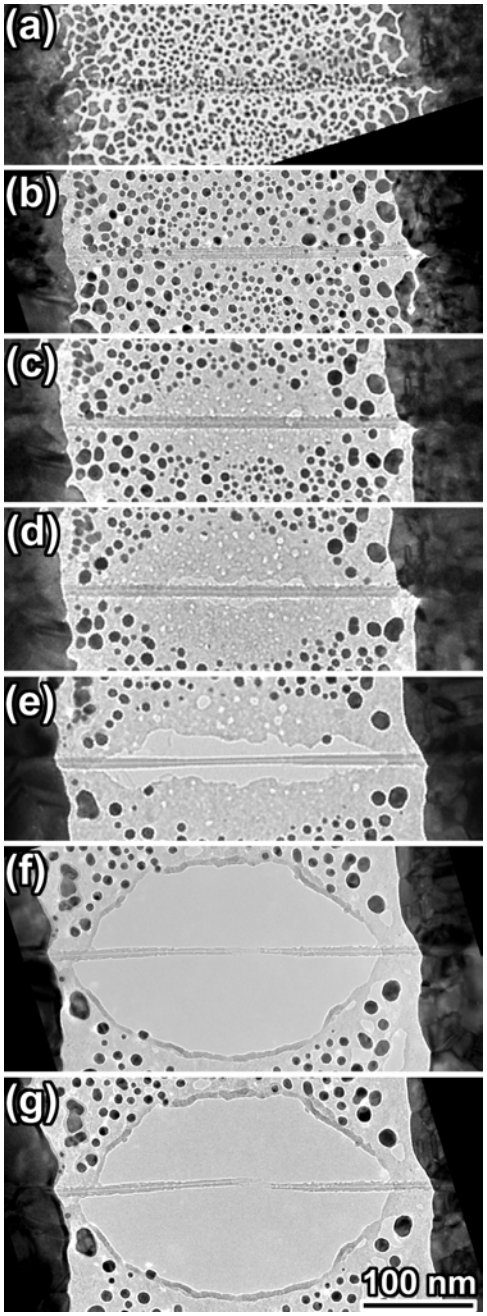

Figure 2.2: A series of TEM micrographs showing the evolution of a MWCNT device over time. (a) Gold nanoparticles cover the as-fabricated device. (b) The device is partially cleaned by the application of 1.7 V ($\sim 190\mu$A). (c) Increasing the voltage to 1.72 V cleans the device further. The Si_3N_4 membrane begins to deteriorate. (d) Raising the voltage to 1.9 V cleans the device of all gold nanoparticles. The membrane under the center section of the MWCNT is gone. (e) The MWCNT has undergone wall-by-wall breakdown and five walls have been removed from the center section. (f) Further breakdown removes all but two complete walls and one partial wall from the center of the MWCNT. (g) The final walls have failed and the MWCNT is now broken into two sections. The scale bar is 100 nm.

Device operation begins in the low-bias regime (< 200 mV), which produces no apparent structural modification on the short time scale of this experiment. In this limit, our devices typically exhibit a linear current-voltage (I-V) relationship, with resistances on the order of 10 kΩ. As the voltage is increased, however, nonlinearities start to appear in the I-V, and at approximately 1 V the contact edges smooth and recede, with a corresponding increase in resistance. We continue to raise the applied voltage and observe cleaning of the MWCNT, as seen in Figure 2.2 (b). Heat dissipation in the MWCNT causes nearby gold nanoparticles to evaporate, while nanoparticles further away coalesce into larger particles.

Annealing of the contacts begins shortly thereafter and is accompanied by a reduction in the resistance of the device. Both contacts become smoother and the grain size approximately doubles, as seen in Figure 2.2 (c). Generally, the MWCNTs also become much cleaner at this stage, although some gold nanoparticles may still adhere at the edges. Applying current sufficient to anneal the contacts and clean off surface contamination can change the total device resistance without modifying the nanostructure itself. Afterwards, repeatability during normal operation is improved. Manufacturing processes incorporating similar heat treatment may produce more uniform, reliable devices.

To simulate prolonged device operation while avoiding excessive beam damage, we continue to increase the input power, which results in localized disintegration of the silicon nitride membrane. Figure 2.2 (d) shows a hole forming beneath the center of the MWCNT. Where the substrate is absent, images of the MWCNTs can be obtained with higher resolution. Suspending nanostructures also eliminates coupling to the substrate during transport measurements.

The evaporation of nanoparticles and the decomposition of the membrane reveal a

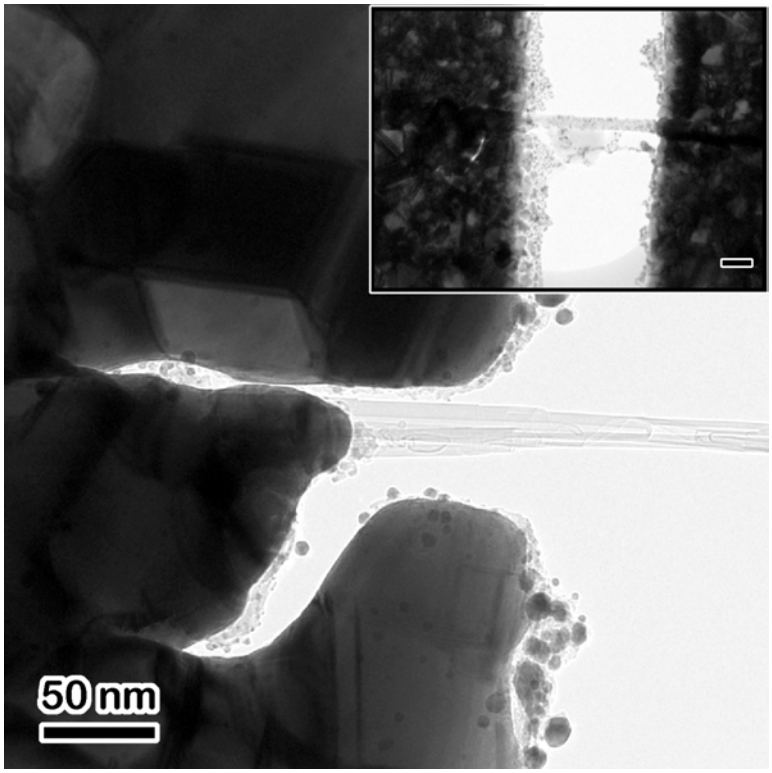

Figure 2.3: TEM micrographs of contact erosion during operation of a device incorporating a bundle of MWCNTs. The inset shows the as-fabricated device prior to the application of any electrical current. After passing 450 μA, the gold contact is eroded. Gold grains in the contact have more than doubled their size, demonstrating annealing of the contact. We also observe significant cleaning of the surface of the MWCNT bundle.

temperature distribution that peaks on the MWCNT midway between the contacts. From the melting point of gold nanoparticles [38], we estimate that by Figure 2.2 (d) the MWCNT has reached temperature in excess of 1200 K, and yet it still shows no damage and continues to function as an effective conductor. The location of the temperature peak clearly indicates that the MWCNT is a diffusive conductor, since ballistic conduction would show dissipation only at the contacts.

Further increasing the voltage drives the MWCNT into current saturation and initiates failure of the MWCNT. As seen in Figures 2.2 (e) and (f), the MWCNT first becomes thinner, with a corresponding discrete resistance increase (to be discussed in greater

detail below). Decreasing the applied voltage interrupts the failure process, allowing time for the acquisition of high magnification images. If the process is allowed to continue, the MWCNT ultimately fails, as seen in Figure 2.2 (g).[†]

The electrically-driven thinning of MWCNTs seen in Figure 2.2 was first observed in TEM studies of bare MWCNTs [39]. This phenomenon has been explored both for its physical implications [24, 26, 39, 25] and as a method to modify MWCNTs for use in nanoelectromechanical systems (NEMS) [40, 41]. Upon first observation in planar devices it was attributed to the sequential removal of individual walls, due to the apparent correlation with discrete, equal decreases in current. The previous reports, however, used intrinsically limited imaging methods such as SEM and atomic force microscopy (AFM) and could not unambiguously correlate each current step to the removal of an individual wall.

Figure 2.4 (a) details the time development of the electronic transport corresponding to the thinning effect seen in Figures 2.2 (d) and 2.2 (e). From time $t = 0$, the voltage is slowly increased in 10 mV steps to 2.56 V. A discrete step in the current response occurs at 2.55 V, followed by four more at 2.56 V. The voltage is then decreased, and the current decreases proportionally. The first current step, from 213.5 μA, is $\sim$25% smaller than the following four ($\sim$13.5 μA). Live imaging during this time period showed five discrete thinning events of the MWCNT, each simultaneous with a step down in current. Figure 2.4 (b) is a high-resolution image taken immediately after the steps were observed, showing that the five outermost walls have been removed from the MWCNT. These data give clear indication of discrete wall-by-wall failure, in which each current step corresponds exactly to the removal of the outermost intact wall.

[†]Figures 2.2 (f) and (g) exhibit beam damage caused by extensive high-zoom imaging during the final stages of MWCNT breakdown. Similar beam damage is not evident in the earlier images because of the annealing effects of the applied bias, discussed further in Chapter 3.

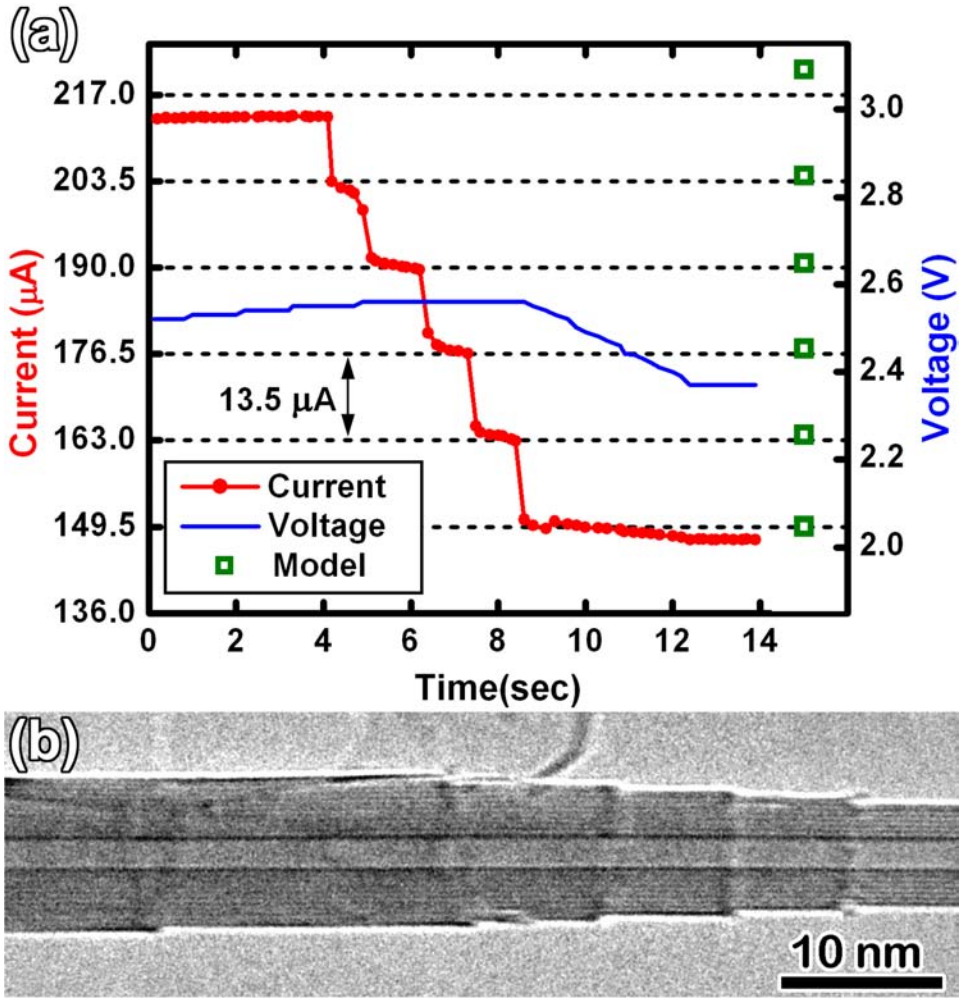

Figure 2.4: Wall-by-wall breakdown of a MWCNT. (a) The current and voltage across the device shown as a function of time. The current decreases in a step-wise fashion with remarkably equal current steps of approximately 13.5 μA. Current steps calculated from a geometric model are shown on the right side of the plot. (b) A TEM image of the MWCNT shows the loss of five walls. The scale bar is 10 nm.

The mechanism by which these walls are removed is unclear. Studies [16, 23, 24, 26, 39, 25] of similar devices in ambient atmosphere have attributed wall removal to oxidation. However, the failure documented here occurs in high vacuum, where oxidation is unlikely to play a significant role. Furthermore, Joule heating of MWCNTs essentially halts oxidation in similar vacuum conditions [42]. Consequently, in the absence of air, an alternate mechanism must be responsible for wall removal. Electron backscattering in

nanotubes at high bias generates optical and zone-boundary phonons [14], which may lead to structural failure in the high current limit.

2.4 Transport data and analysis

Our ability to correlate electronic transport with high-resolution imaging allows for quantitative examination of competing models of MWCNT transport. In previous studies of thinning in MWCNT devices, the imaging was performed after the fact and only determined the external dimensions of the MWCNT. The internal structure of the nanotube, including the core size and number of walls, could not be determined. We directly observe how many walls are removed, when they are removed, and over what length.

2.4.1 Evaluation of existing models

One model attributes the current steps to the wall-by-wall failure of a saturated MWCNT, and posits that each wall carries the same current. This model implies proportionality between the current and the number of remaining walls. [†] Figure 2.4 (b) shows five walls removed from a total of twelve. Extrapolating the observed current staircase for seven more steps from ~ 150 μA, this model predicts a current of ~ 50 μA remaining even after all the walls have been destroyed.

Another model for MWCNT conduction is one in which current is carried solely by the outer wall, as was reported in measurements of the Aharonov-Bohm effect in MWCNTs at low temperatures. Adapting this model, which was developed for the low bias limit, to our case, we assume that as each wall fails, conduction passes to the outermost intact

[†]In the original study in which this model was proposed, the number of remaining walls could not be measured and had to be inferred from transport data [23].

wall. To explain the equal current steps, we assume that the current carrying capacity of each wall is linearly proportional to its circumference. For an outer diameter of 9.5 nm (as measured from TEM images) and the measured initial current of 213.5 μA, this model predicts current steps of 15.3 μA, which is substantially higher than the measured value of 13.5 μA. From the examination of these two models we conclude that under these operating conditions, the conduction through the MWCNT is neither solely in outermost wall, nor is it equally divided among the walls.

2.4.2 Lathe model

Analyzing the MWCNT as if it were a tube of bulk material with a hollow inner core gives competitive agreement with the data. In this case, the electronic breakdown process is equivalent to the nonuniform removal of material from the outside of the tube as if done with a lathe. Using the high resolution images, we measure the MWCNT geometry and calculate the expected resistance assuming an isotropic conductivity tensor. The resistivity of the material ($\sim 1.9 \cdot 10^{-6}$ Ωm) is calculated from the final resistance and geometry. We allow for one other free parameter, the contact resistance (2.2 kΩ). Surprisingly, this simple model fits the data rather well, as shown in Figure 2.4 (a). The singular exception is the first current step, but this step is anomalously small according to all three of the models considered here. The reduced current carrying capacity of the original outer wall may be attributable to damage by TEM beam exposure or surface contaminants.

Confirmation of the lathe model and more detail on the fitting procedures can be found in Section 3.5.2.

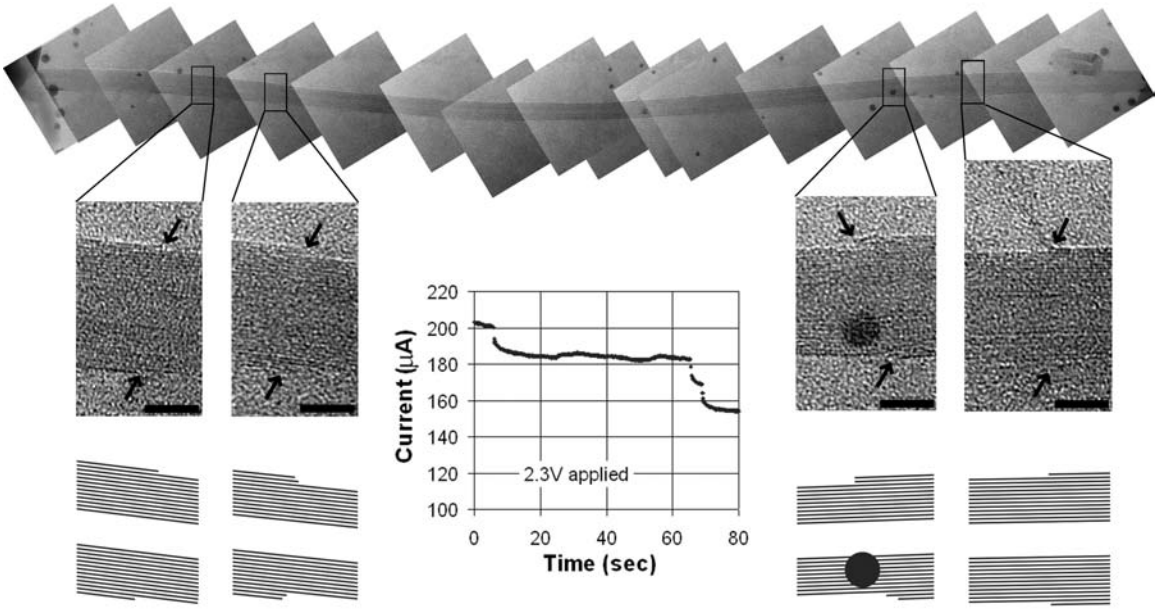

Figure 2.5: TEM micrographs and current vs. time for nanotube breakdown in air. The TEM micrographs were taken after breakdown and clearly show three walls removed from the center section of the nanotube. Three corresponding steps in the current passing through the nanotube were observed during breakdown.

2.5 Breakdown in air

We have also studied the failure of MWCNTs when subjected to high currents while exposed to air at ambient conditions. The presence of air should both increase the rate of heat transfer away from the MWCNT and allow for the oxidation of the MWCNT at approximately 700°C. Although one would expect dramatically different behavior in air and in vacuum, we obtain results that are surprisingly similar to the results discussed above.

Figure 2.5 details the removal of three walls from a MWCNT in air. We gradually increase the voltage across the MWCNT until we reach 2.3 V, at which point we observe three steps in the current passing through the MWCNT. We ramp down the voltage and load the sample into the TEM, where we obtain the micrographs shown in Figure 2.5.

The similarity of the applied voltage and current at the threshold of breakdown

both in air and in vacuum is striking, and raises several distinct possibilities. The first is that when exposed to air, the hot MWCNT oxidizes, as suggested by Collins [23]. To reach the same range of applied voltages and currents that can be reached in vacuum, however, the MWCNT must be strongly cooled by collisions with air molecules, and the apparent match between thresholds in air and in vacuum is merely a coincidence. This seems unlikely, however, since in a large number of measurements (performed both by us and by others [23, 43]), MWCNT failure tends to occur in the same voltage and current range regardless of atmosphere.

Another possibility is that the breakdown in either case is purely voltage or current driven and is independent of temperature. Here, cooling due to the presence of atmosphere must keep the MWCNT below oxidation temperatures so that it may carry the applied current without burning. Future experiments to identify the exact nature of MWCNT breakdown are necessary to resolve this issue.

Chapter 3

Shrinking carbon nanotubes

3.1 Introduction

The diameter d of a carbon nanotube determines several of its key physical characteristics. These include electronic properties (the band gap of a semiconducting singlewalled nanotube is proportional to $1/d$) and mechanical properties (the bending stiffness of a multiwalled nanotube is proportional to d^3). Despite many experimental studies, however, the relationship of diameter to the electrical resistance or current capacity of a multiwalled carbon nanotube is not well established.

To resolve this issue, we have developed a method to shrink an individual carbon nanotube to any desired diameter, as illustrated schematically in Figure 3.1. As the nanotube shrinks, we monitor its electrical resistance. A model is presented which accurately predicts the resistance for arbitrary geometry. In the limit of vanishing nanotube diameter, negative differential resistance is observed, as expected for a carbon chain.

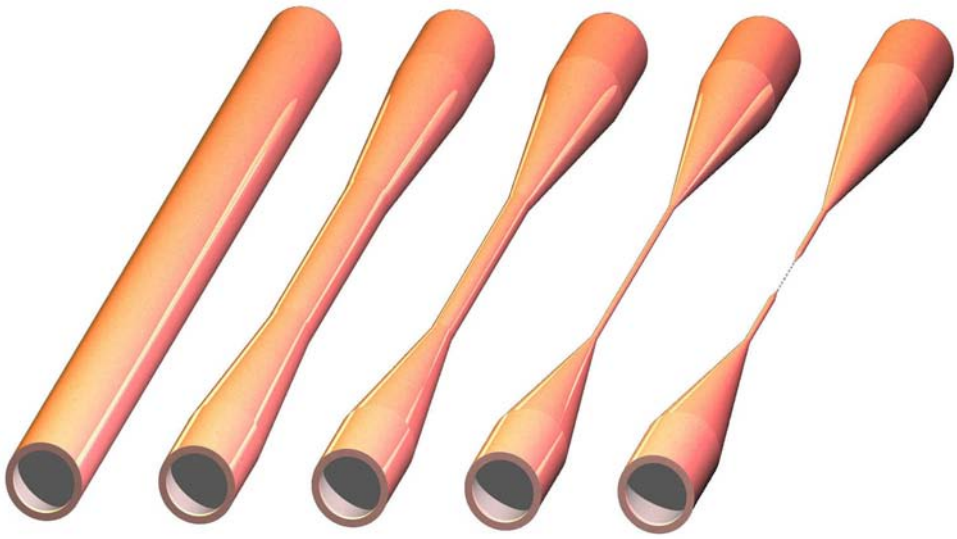

Figure 3.1: Illustration of the shrinking process.

3.2 Shrinking process

The geometrical tailoring process starts with a multiwalled carbon nanotube (CNT) of arbitrary wall number and diameter. First entire shells are successively removed until a CNT with the desired wall number is achieved. Carbon atoms are then selectively removed from the CNT walls, leaving substantial atomic vacancies. A high temperature anneal/electromigration treatment shrinks and reforms the CNT into a high quality tube of smaller diameter. The process can be repeated in a highly controlled fashion, yielding a high quality CNT of any pre-selected and precise diameter. The modification is performed in situ in a transmission electron microscope (TEM) which permits high-resolution real-time monitoring of the CNT geometry, as well as simultaneous dc electrical measurements of the shrinking CNT which can be correlated to the CNT geometry. Importantly, throughout the entire shrinking process the electrical contacts to the CNT remain the same and undisturbed, eliminating the contact variances which have plagued virtually all earlier attempts to correlate CNT geometry and conductance.

We prepare the CNT for simultaneous TEM imaging and electronic characterization by employing a two-probe device architecture with an electron transparent membrane. The membrane is prepared by growing 10-20 nm of silicon nitride on a Si/SiO_2 wafer, which is then back-etched to selectively remove the silicon and silicon oxide layers. Arc-grown nanotubes are deposited onto the membrane out of isopropyl alcohol and located by scanning electron microscopy (SEM). Electrical contacts are patterned by electron beam lithography and deposited via electron beam evaporation of 30 nm of gold. The device is then loaded into a JEOL 2010 TEM with *in-situ* transport capability operating at 100 keV. A Keithley 2410 SourceMeter is used to apply voltages and measure resistance across the two-terminal CNT devices.

Figure 3.2 shows TEM micrographs of the time evolution of a nanotube device. The initial CNT as shown in Figure 3.2 (a) has four walls and an outer diameter of 21.5 nm. An applied voltage to the nanotube causes the outer two walls to fail, an effect that has been observed both in vacuum [39, 44, 43] and under ambient conditions [16].

To shrink the (in this case two-walled) CNT we more selectively remove carbon atoms from the remaining CNT walls by exploiting knock-on damage induced by the 100 keV TEM electron beam. Such atomic displacement causes numerous vacancy and other defects and a general loss of the perfect nanotube wall graphitic structure [45, 46, 47, 48], and the displaced carbon atoms are either ejected outright or are migrated along the tube [48]. Since we are here most interested in the properties of a high-quality CNT, we require a method to reform the (fewer) remaining "tube" carbon atoms into a near-perfect graphitic CNT. This is achieved by the simultaneous application of an electrical current through the CNT device via the electrical contacts, which has two main effects. First, via Joule heating, it increases

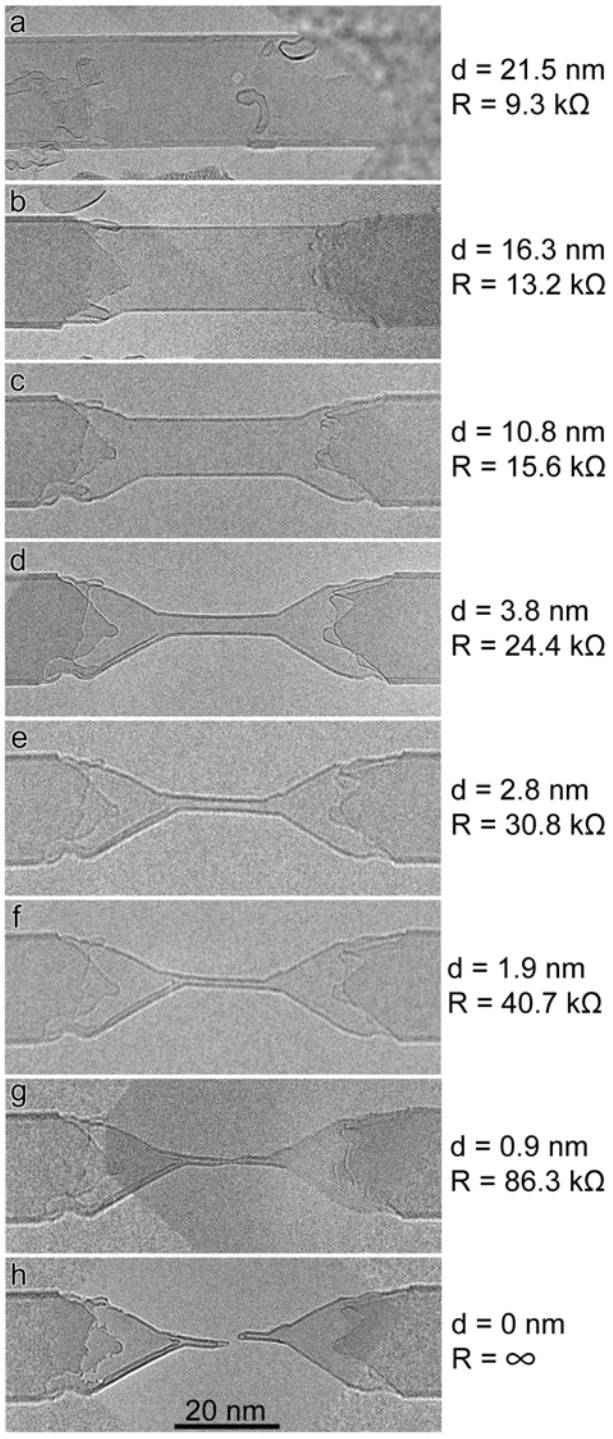

Figure 3.2: Transmission electron micrographs of a CNT device as it evolves under transport current bias and exposure to the TEM beam. Reducing the applied bias can halt the shrinking process at any time. The minimum CNT diameter and high-bias resistance associated with each image are shown to the right.

the temperature of the entire nanotube, allowing for thermal annealing of structural damage [49]. Second, via electromigration of carbon ions, it affords a more rapid reshaping into a defect-free tube (sourcing limited carbon ions where they are needed and sinking them where they are not). The reduced-diameter CNT remains structurally and electrically connected to the original contacts via strain-energy-minimized cones. As shown in the sequentially acquired frames of Figures 3.2 (b-f) and in the inset of Figure 3.3, the shrinking CNT remains clean and retains its distinct, parallel two-wall structure throughout the process. These features distinguish the high quality of the CNT, especially when compared to TEM images of inferior CNTs, which may show surface contamination, corrugations, discontinuities, or interwall defects [50].

Two competing factors influence how much current should be applied to the nanotube during the shrinking process. First, the applied current must not exceed the threshold for electrical breakdown of the CNT after the desired number of walls has been reached. For arc-grown CNTs, we observe the onset of electrical breakdown at applied voltages in the range 2 – 3 V. Second, if maximal shrinkage of the nanotube is to occur, the current must be kept as high as possible so as to keep the largest possible length of nanotube at temperatures high enough to anneal out beam damage (comparison with previous studies shows that the maximum CNT temperature is at least 1200 K [44]). In practice, the applied voltage is incrementally increased above 2 V until shrinkage is observed, with the ultimate threshold dependent upon the selected intensity and acceleration voltage of the electron beam. Once the shrinking process begins, the applied voltage must be tuned to compensate for the changing resistance of the CNT.

3.3 Mass loss analysis

We consider briefly the dynamics of the shrinking process. The susceptibility to radiation damage of an atomic lattice can be characterized by the threshold displacement energy E_{thr}, the minimum kinetic energy transfer which can permanently displace an atom from its lattice site. While studies of multiwalled CNTs at room temperature report values of E_{thr} in the range of 15 - 20 eV [51], we expect E_{thr} of the shrinking CNT to be much smaller, since in this high temperature regime CNTs become superplastic and can easily be deformed [49].

We determine E_{thr} by measuring the atomic displacement rate p. A comparison of the 15 nm center region in parts B and F of Figure 3.2 indicates a loss of $\sim$88% of the carbon atoms, corresponding to an exponential decay with time constant $1/p \approx 1000$ seconds. The displacement cross section (for simplicity assumed to be isotropic) is given by $\sigma = p/j$, and, for a beam current density $j \approx 1$ A/cm^2, we obtain $\sigma \approx 160$ barns. Using the analytical approximation in [51] which relates to E_{thr}, we estimate the threshold displacement energy under these conditions to be $\sim$5.5 eV, a much smaller value which approaches the E_{thr} of amorphous carbon at room temperature [51].

3.4 Control of shrinking process

As an example of the detailed diameter control of the CNT during the shrinking process, we show in Figure 3.3 the time evolution of the CNT between two diameter "set points." The initial diameter (equal to 3.7 nm as targeted from an earlier shrinking process) is stable until the current bias is applied. The diameter then decreases smoothly until the new set point of 2.8 nm is reached, whereupon the bias is immediately switched off, and the

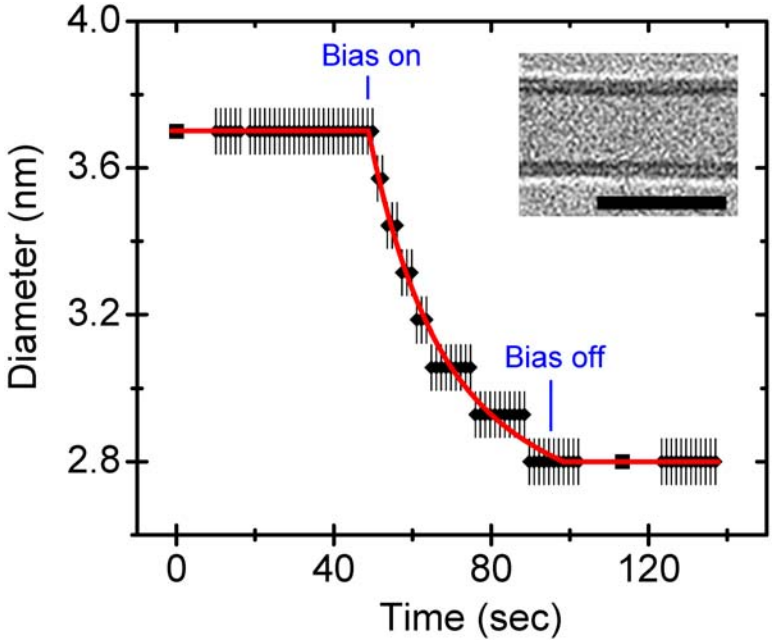

Figure 3.3: Diameter control of the CNT. Raising (or lowering) the applied bias initiates (or halts) the reforming process. The two square points are obtained from high resolution TEM still images, while the remaining data are binned by discrete numbers of pixels obtained from a low resolution video recording. The curved red line is the sum of two exponentially decaying terms (see text). Inset: A digitally magnified TEM image of the center section of the CNT. The scale bar is 5 nm.

new diameter is locked in. The two square points on the flat parts of the curve in Figure 3.3 are obtained from high resolution TEM still images, while the remaining diamond data are obtained from lower resolution video recordings (the discreteness of these data is artificial and due to the inevitable binning of discrete numbers of pixels in the video recording analysis). The curved red line in Figure 3.3 is a sum of two exponentially decaying terms, with respective time constants 16 seconds and 1000 seconds. The faster initial reforming rate (16 s) is due to an increased initial defect density from prior exposure to the TEM beam without an applied bias high enough to initiate reforming. The slower rate (1000 s) matches the calculated rate for the entire process and is limited by beam-induced defect formation.

The inset to Figure 3.3 is a TEM image of the tube during the shrinking process, and the well-formed wall images attest to a high tube quality. At a given diameter, blanking of the TEM beam prevents further defects, while continued exposure to the high energy electrons can be used to increase the number of CNT defects in accordance with the model described above. Thus, our tailoring process allows us not only to select precisely the ultimate diameter of the CNT but also to tune its defect density.

3.5 Electronic characterization

3.5.1 Resistance measurements

Of prime interest is the connection between the precise CNT geometry and the corresponding electrical conductance. Previous studies of electronic conduction in CNTs have reported widely varying results, with proposed mechanisms including single ballistic channel conduction, multiple ballistic channel conduction, and fully diffusive transport [21, 28, 27]. For multiwalled CNTs the situation is particularly complex with intertube conduction entering the mix. In particular, the geometrical distribution of high bias current in a multiwalled CNT is in question: reports range from equal amounts of current in each shell [23] to current constrained to the outer shells [21, 26] to current distributed uniformly across the entire cross section [44]. Much of this controversy may stem from the different electrical contacts used in each experiment, as even contacts formed by similar macroscopic processes may vary greatly on the nanoscale. The present study circumvents this problem, as the transport properties of CNTs with many different diameters are investigated while keeping the contacts essentially identical.

As the nanotube shrinks, its resistance increases, as shown by the resistance values

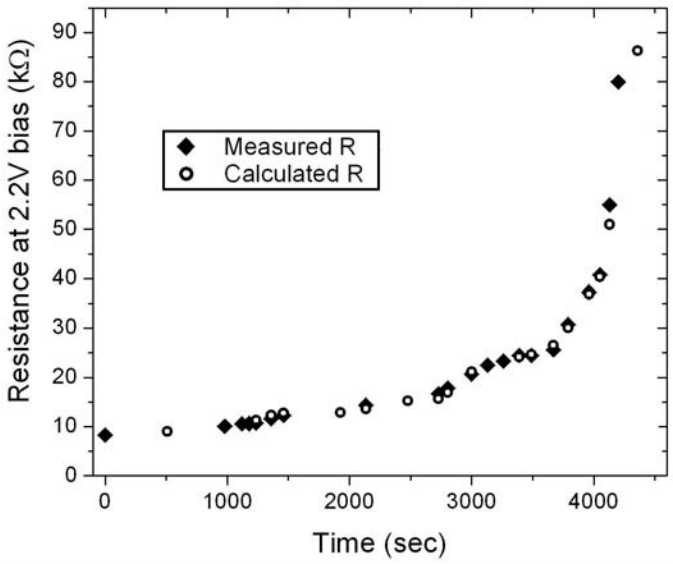

Figure 3.4: Calculated and measured resistance of the shrinking CNT vs. time.

displayed on the right column of Figure 3.2. From the chiral dependence of conduction in single wall carbon nanotubes [5], one might expect discrete changes in conductance as one wall or the other becomes semiconducting or metallic. We do not observe this. In fact, as our analysis below shows, the CNT resistance, irrespective of nanotube diameter, can be accounted for by a simple model that assumes strictly diffusive transport. Figure 3.4 shows an excellent fit between measured resistance values and resistance values calculated from the geometric model. We find that the total CNT resistance is dictated wholly by its geometry, with CNT conductance linearly proportional to its cross sectional area.

3.5.2 Lathe model

We fit the experimental resistance data using Ohm's law by slicing the geometric model into pixel-thick circular cross sections of uniform inner and outer diameter. The

resistance is then calculated from the sum:

$$\int \frac{\rho}{A}\, dL + R_0 \approx \rho \sum \frac{\Delta L}{A_i} + R_0 \tag{3.1}$$

where ρ is the bulk resistivity, R_0 is the contact resistance, A_i is the cross sectional area of each slice and ΔL is the length associated with a single pixel (0.054 nm). This approximation is accurate for a hollow tube with constant diameter (strictly speaking, there is a small error of order 5% introduced in the regions in which the diameter is changing [52], but this does not significantly alter the total resistance values).

We obtain an excellent fit to the measured resistances with bulk resistivity $\rho = 3.8 \cdot 10^{-6}$ Ω·m and contact resistance $R_0 = 6.1$ kΩ. (The calculated contact resistance includes the lengths of nanotube leading from the metal contacts to the region of interest shown in Figure 3.2. Subtracting the resistance of these lengths (calculated from the fitted resistivity) yields a total metal-nanotube contact resistance $R_0 = 1.3$ kΩ.) The calculated resistivity agrees well with high temperature measurements of the basal plane resistivity of pyrolytic graphite, on the order of 10^{-6} Ω·m at 1200 K [53, 54, 55].

Calculated and measured high temperature resistance values for the diameter-selected CNTs are shown in Figure 3.4. To evaluate the fit we calculate the coefficient of determination:

$$r^2 = \frac{\sum_i \left(R_i - \bar{R}\right)^2 - \sum_i \left(R_i - \hat{R}_i\right)^2}{\sum_i \left(R_i - \bar{R}\right)^2} \tag{3.2}$$

where R_i is a calculated value, $\hat{R}_i$ is the corresponding measured value, and $\bar{R}$ is the arithmetic mean of the calculated values. Correlation of measured and calculated

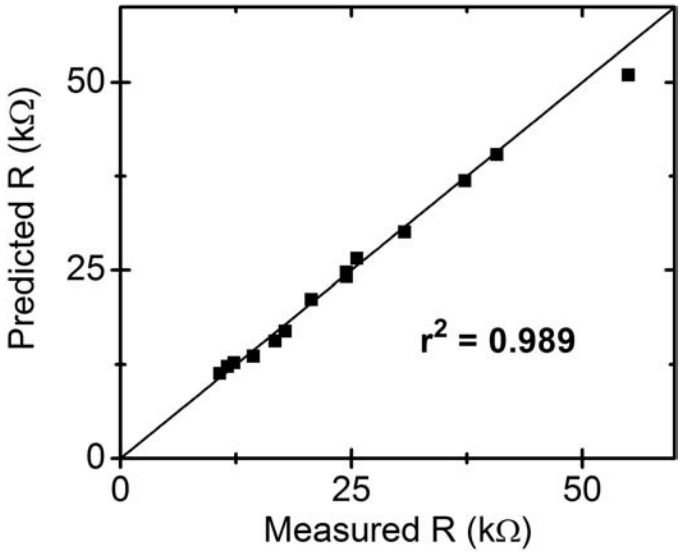

Figure 3.5: Calculated resistance vs. measured resistance of the CNT. The coefficient of determination of the fit is 0.989, which increases to 0.995 if the last point is excluded.

resistances yields a coefficient of determination $r^2 = 0.989$, indicating an excellent fit. The data acquired as the nanotube diameter gets very small deviate from the fit due to the high sensitivity of the calculation to pixel-sized effects at these small diameters. If the last point in Figure 3.5 is excluded, r^2 increases to 0.995.

3.6 Zero diameter limit

If the thinning process is allowed to continue, the nanotube eventually fails. As the diameter shrinks below 1 nm, the inner wall finally breaks and endcaps form on both ends, leaving a very thin bridge connecting the two sections of nanotube. This bridge is not stable under the electron beam and rapidly fluctuates, changing appearance from acquired image to the next. In one instance, shown in Figure 3.2 (g), the bridge appears to be a single wall nanotube (an inner hollow is visible), though in images taken before and after it appears amorphous and the thinnest section cannot be resolved. It is likely that

as the carbon removal progresses the bridge assumes a carbon-chain-like structure. In the atomically segmented bridge regime the geometric-based CNT conduction model described above obviously breaks down.

3.6.1 Atomic carbon chains and negative differential resistance

Theoretical studies of atomic carbon chains can be used predict the electronic transport behavior of an atomic carbon chain. A key prediction is that of negative differential resistance (NDR) at applied voltages of a fraction of a volt [56, 57]. NDR is the basis for a number of semiconductor devices, and the use of components that exhibit NDR can significantly simplify the design of circuits with complicated functions [58]. In recent years, NDR has been observed in a variety of molecular electronics [59, 60, 15].

Figure 3.6 shows transport current-voltage (I-V) behavior for our CNT device in two different regimes. Figure 3.6 (a) is for the device with an intact CNT spanning the contacts, while Figure 3.6 (b) is in the bridge regime where the nanotube is just failing (between panels (g) and (h) in Figure 3.2). In the bridge regime the device exhibits NDR at both positive and negative bias of 0.3V, in agreement with theoretical predictions for an atomic carbon chain (Figure 3.7).

Continued exposure to the electron beam causes any carbon chain bridge to ultimately and permanently fail, and the device becomes electrically insulating, as for Figure 3.2 (h). The permanently closed end caps on both the inner and outer wall of the two nanotube segments are clearly visible. It is interesting to note that even after failure, such membrane-anchored devices could serve as templates for single molecule electronics, with the remaining nanotube sections acting as very closely spaced electrodes [61].

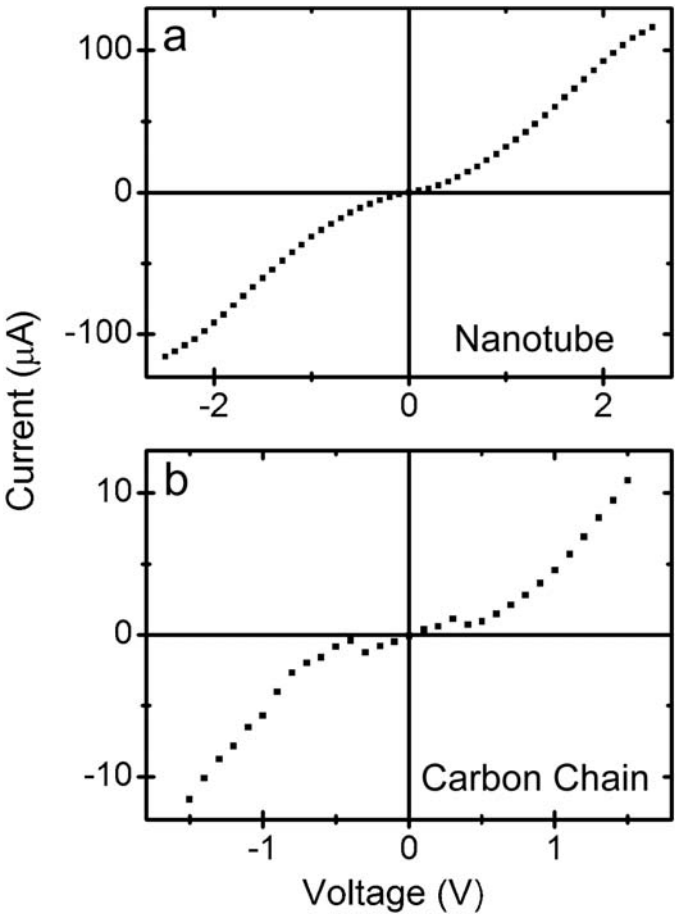

Figure 3.6: Current-voltage characteristics of the nanotube device. Part (a) shows a typical characteristic for an intact CNT. Part (b) shows the characteristic just before failure, in the carbon-chain regime. Negative differential resistance is clearly observed at $\pm$ 0.3 V.

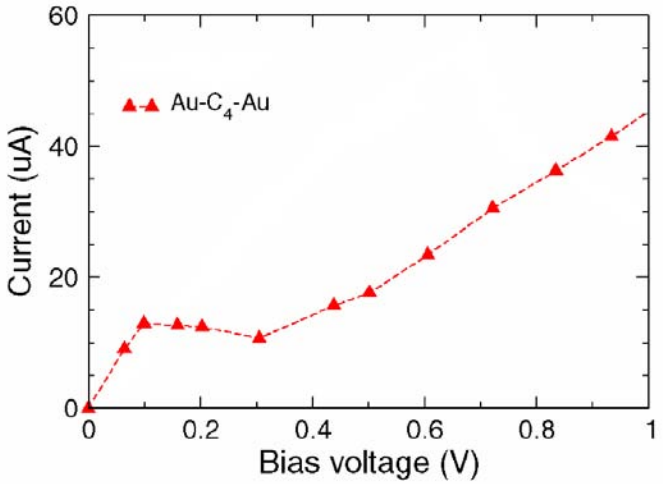

Figure 3.7: Theoretical calculation of I-V characteristics for a C_4 atomic wire suspended between gold contacts. Adapted from [57].

Chapter 4

Precise cutting of nanotubes with a low-energy electron beam

4.1 Introduction

On several occasions during our experimental studies we have observed that the low energy electron beam of a scanning electron microscope (SEM) can cause damage to nanostructures. The mechanism causing this damage is not immediately clear, and must be different from the high energy knock-on damage described in the previous chapter. To study this effect further we have employed a combination of *in situ* SEM beam exposure in varying atmospheres with high resolution transmission electron microscopy (TEM) post-mortem analysis. We find that the atmosphere in the SEM is a key factor in determining how much damage the electron beam will cause. By harnessing this effect we are able to precisely damage or cut through various nanostructures, including carbon and boron nitride nanotubes.

4.2 Cutting nanotubes

At present it is difficult to control the length of nanotubes created by any particular synthesis process. Moreover, the fabrication of nanotube-based devices is often performed with poorly controlled solution deposition or chemical growth techniques, which can easily lead to device components contacting multiple nanotubes where only one is desired. A versatile method for cutting nanotubes is therefore required. Such a method would find immediate use in applications such as carbon nanotube tipped atomic force microscopy (AFM) cantilevers [62] that require nanotubes be cut down to a certain length for optimum device performance (see Chapter 7). A precise cutting mechanism could also aid in the creation of nanotube-based mechanical systems which require nanotubes that have been selectively damaged, such as nanoscale rotational actuators (see Chapter 5).

4.3 Other cutting methods and their drawbacks

Several methods for cutting or damaging nanotubes have been previously reported, each with distinct disadvantages. Chemical etches have been used to shorten nanotubes [63], but these etches indiscriminately damage all high curvature regions of a nanotube and are difficult to control. Highly selective damage has been induced in transmission electron microscopes, using both voltage pulses applied through a nanomanipulator [39] and knock-on damage caused by the high-energy electrons beam [64]. TEM work, however, requires an electron-transparent substrate, which severely limits the types of devices that can be imaged. Similarly, while nanotubes can be cut by voltage pulses applied through a scanning tunneling microscope (STM) tip [65] or AFM tip [66], many nanotube-containing devices are either too delicate or too irregular to be imaged by STM or AFM, or lack a

conductive substrate (which is necessary for STM). Scanning probe methods are also very time consuming. Finally, passing current through an electrically contacted nanotube may cut it [16], but the exact location of the cut is uncontrollable and the current may also damage the primary nanotube used in the device.

4.4 Cutting process

We have developed a technique by which nanotubes are controllably damaged using the low energy focused electron beam of a scanning electron microscope. We are able to cut through nanotubes, or, with smaller doses, to create hinge-like defects. Examination of damaged nanotubes in a TEM reveals that material is removed with minimal damage to surrounding areas. Our method is compatible with most device architectures (the nanotube need only be viewable in an SEM), offers complete control over where the nanotube will be cut, and is relatively fast, requiring only several minutes to load, locate and cut the nanotube in the SEM.

Multiwalled carbon nanotubes synthesized by the standard arc-discharge technique were dispersed in either ortho-dichlorobenzene or isopropyl alcohol (no dependence upon the particular solvent used was seen). The nanotube solution was then deposited either onto TEM grids coated with lacey carbon for TEM imaging or onto a silicon oxide surface for in situ electrical transport studies. Electrical contacts were patterned by standard electron beam lithography and were composed of gold over a thin chromium adhesion layer. The samples were then loaded for cutting into an FEI XL30 Sirion SEM. During cutting, the SEM was operated in line scan mode at maximum magnification (10^6 X), with the nanotube axis perpendicular to the scan line. Several different gasses were introduced through a leak

valve, and partial gas pressures were measured with a Stanford Research Systems SRS200 residual gas analyzer. Absolute pressure was measured using a Bayard-Alpert ion gauge and a Terranova 934 controller programmed with the appropriate gas constants. A Keithley 2400 SourceMeter was used for transport measurements. TEM images were taken before and after cutting in a JEOL 2010 TEM using an acceleration voltage of 100 keV.

We were able to cut through nanotubes at a variety of acceleration voltages, beam currents, and gas pressures within the microscope chamber. The cuts were seen as a gradual decrease in height and width of the nanotube line scan profile, and the decrease accelerated as the cut neared completion. We could interrupt any cut by blanking the beam or switching the microscope out of line scan mode. If the nanotube was suspended, as on a TEM grid, a sufficiently damaged region would often act as a loose hinge, with the nanotube swinging under the charging influence of the electron beam. We have also been able to make oblique cuts by rotating the scan line relative to the nanotube, which may be useful for making sharpened AFM tips.

Figure 4.1 shows a nanotube on a TEM grid before and after cutting. Figure 4.1 (a) shows the uncut nanotube suspended across a gap. The turbulent deposition method displaced the ends of the nanotube perpendicular to its longitudinal axis, subjecting it to a shear strain which was maintained by contact with the grid and other deposited material. This shear strain was released when the nanotube was cut, and the two sections of the nanotube straightened out, as seen in Figure 4.1 (b). Figure 4.1 (c) is a close-up image of a section of the pristine nanotube before cutting. Figure 4.1 (d) shows the same section after cutting, with the two cut sections rotated and aligned to vertically correspond with Figure 4.1 (c). A comparison of these last two images shows that the cut removed

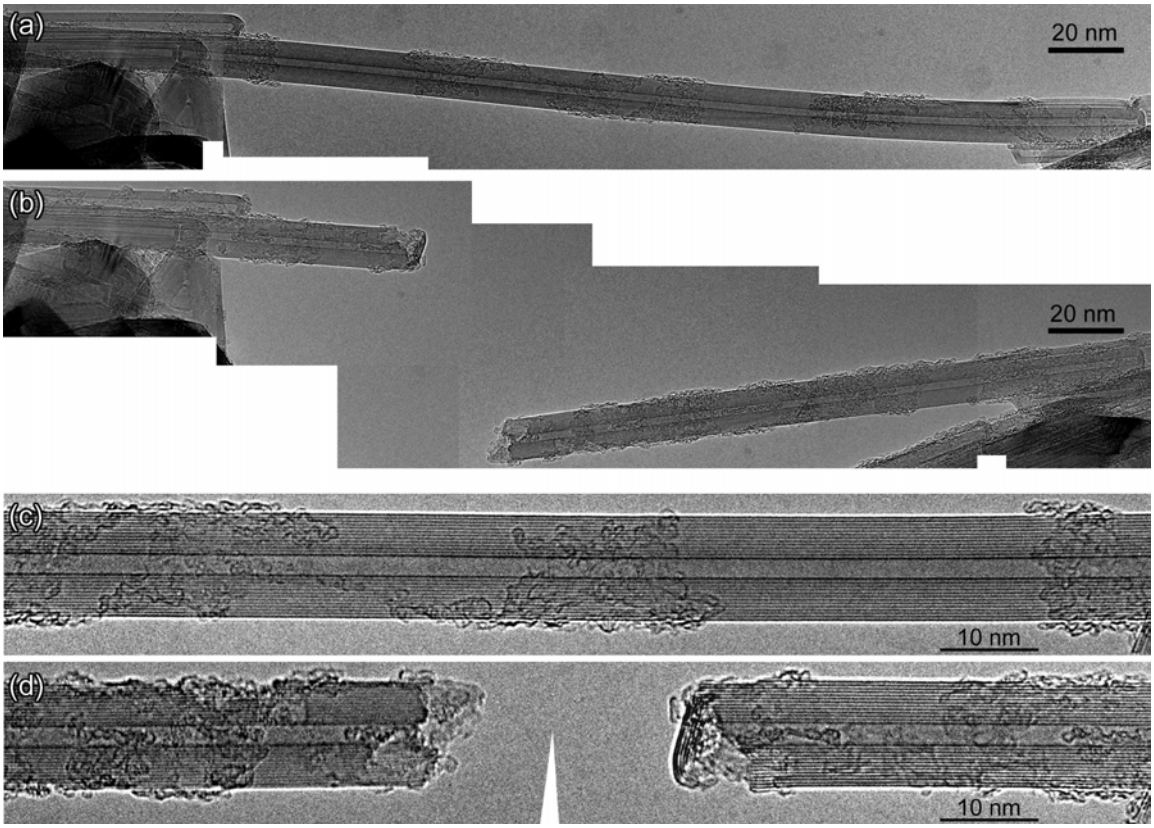

Figure 4.1: Composite TEM micrographs of (a) a nanotube in its pristine state suspended on a TEM grid, (b) the same nanotube after cutting, (c) a close-up image of the same nanotube in its pristine state, and (d) the cut segments of the nanotube, rotated and aligned to vertically correspond with the same sections in (c).

approximately 25 nm of material. This gap is larger than the ∼3 nm beam spot size, most probably due to beam position drifts over the duration of the cutting process. Nonetheless, the damage induced by the electron beam was confined to the immediate region of the cut, with equal damage done to each subsequent layer of the multiwalled nanotube.

4.5 Analysis and physical processes

The most important factor affecting the cutting speed was the presence of water vapor within the chamber. Figure 4.2 shows the results of cutting through a single nanotube

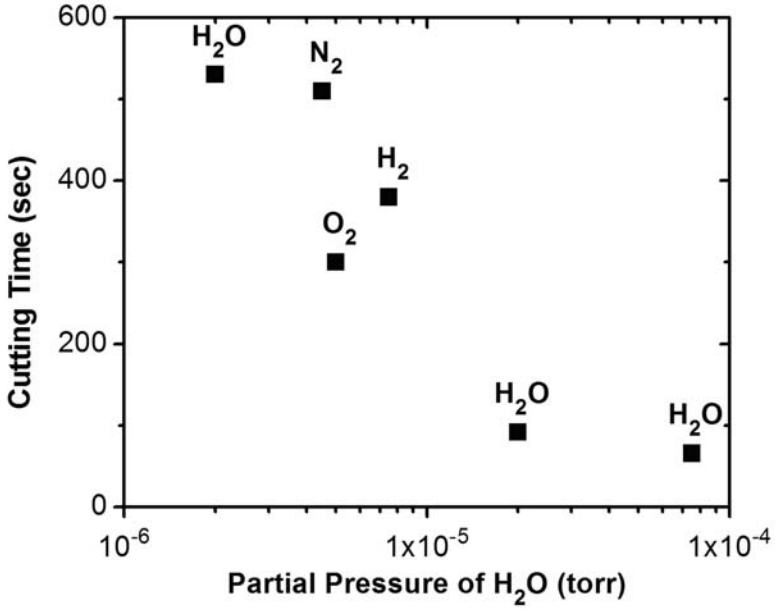

Figure 4.2: Cutting times for multiple cuts on a single nanotube in different atmospheres. The partial pressure of water is shown on the horizontal axis, while the majority gas is shown above the data points. The total pressure was $7.5 \cdot 10^{-}5$ Torr during the N_2, O_2 and H_2 trials.

at several points along its length in different atmospheres, with an acceleration voltage of 1 keV and a beam current of 118 pA. At total pressures below $2 \cdot 10^{-6}$ Torr, where most of the residual pressure was due to water vapor, nanotubes could be exposed to the beam for over 10 minutes and still not be visibly damaged. Bleeding in nitrogen to a pressure of $7.5 \cdot 10^{-5}$ Torr did not significantly affect the cutting time. Bleeding in hydrogen at the same pressure resulted in slightly faster cuts, but this may be due to a higher partial pressure of water (our hydrogen source contained a partial pressure of water over fifty percent higher than in the other gasses). Oxygen consistently increased cutting speed up to twice as fast. Water, at the same pressure, would increase the cutting speed even more, up to ten times as fast.

Electron beam induced mass loss is a well known effect in electron microscopy of biological samples [67]. Studies have found that a common source of mass loss is caused

by the presence of water [68, 69]. Radiolysis of water molecules is the driving force behind this etching mechanism [70]: highly reactive OH·, H·, and HO_2· radicals can react with carbon atoms to form CO, CO_2, various hydrocarbons and hydrogen gas, leading to mass loss of the original carbonaceous specimen (and similar reactions can be expected when oxygen molecules are ionized in the vicinity of the sample). We propose that this etching mechanism is responsible for damaging the nanotubes. This mechanism is fundamentally different from previously reported electron beam irradiation damage of nanotubes as seen in a TEM, where incident electrons eject carbon atoms from the nanotube and must have an incident energy of at least 86 keV [71].

Interestingly, we found that bundles of nanotubes would consistently be cut faster than individual nanotubes, despite the greater amount of material that must be removed. Theoretical calculations of water adsorption on the outside of nanotube bundles have shown, however, that water molecules will be adsorbed first into the groove between two nanotubes and only at higher densities will they then be adsorbed onto the entire nanotube surface [72]. This suggests that bundles will adsorb more water at a given pressure than individual nanotubes. Since the presence of water greatly accelerates cutting, we can therefore expect nanotube bundles to be easier to cut.

Two-contact electrical transport shows a steady increase in the resistance of the nanotube during the cut, with no steps or jumps showing opening or closing of discrete conductance channels. We did find, however, that by passing current through the nanotube during a cut we could reduce the damage done to the nanotube and greatly increase its lifetime under the beam. For example, putting 1.7 V across a nanotube with an initial resistance of 15 kΩ would decrease the cutting rate by a factor of 4 (this cut took 20

minutes, while two separate cuts on the same nanotube with no voltage applied took 5 minutes each).

Resistively heating the nanotube may reduce the damage through two possible mechanisms. It has been shown that raising the temperature of nanotubes to over 300°C reduces knock-on damage by annealing out defects via the increased mobility of interstitial atoms [73]. Also, by increasing the temperature of the nanotube we decrease the sticking coefficient of water molecules impinging on the surface, thus limiting the number of molecules present to aid in the cut.

Figure 4.3 shows the results of cutting two nanotubes exposed to different partial pressures of water at various beam currents. At a higher partial pressure, increasing the beam current speeds up the cutting process. This is simply the consequence of adding more energy to the system, thus increasing the rate of the chemical reaction. At low water vapor pressure ($2 \cdot 10^{-6}$ Torr), however, this effect was greatly suppressed, and even high beam currents ($\sim$ 500 pA) would not significantly increase cutting speed. Therefore we propose that at low pressures the rate is limited by the amount of water present rather than the amount of energy supplied by the electron beam.

Figure 4.4 (a) shows cutting times for multiple cuts on several nanotubes at different acceleration voltages. Contrary to naïve expectation, increasing the acceleration voltage of the electron beam increases the cutting time. This effect is due to the cross section for the ionization of a water molecule decreasing as the incoming electrons become more energetic. Schutten et al [74] have measured the total ionization cross section for water for this range of electron energies. A normalized plot made by rescaling the cutting times of different nanotubes to match at common acceleration voltages is shown in Figure 4.4 (b), together

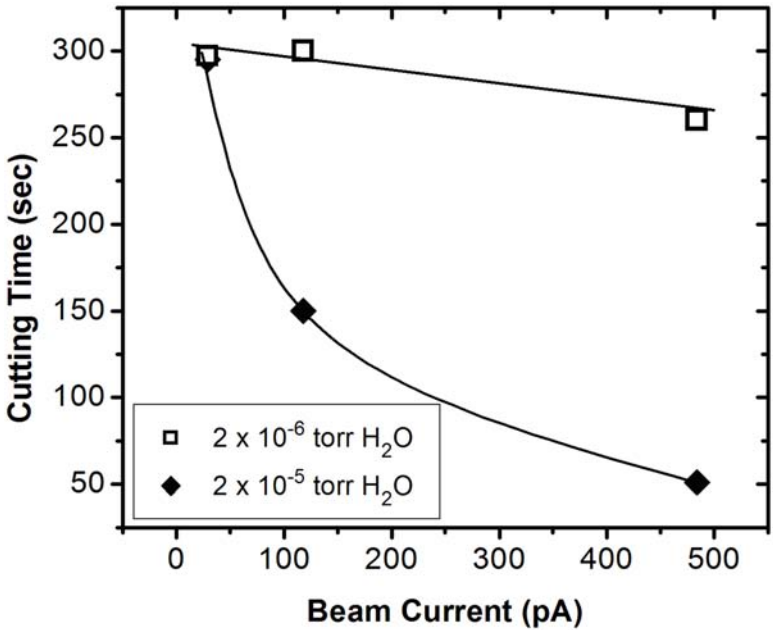

Figure 4.3: Cutting times for multiple cuts on two nanotubes in different atmospheres at different beam currents. In both cases the majority gas was water vapor. The dashed lines are guides for the eye.

with a plot of the inverse of the total ionization cross section.

We were careful to minimize the beam exposure while locating and imaging the nanotubes prior to cutting. From our results it is evident that precautions must be taken during all SEM/nanotube experiments to limit beam-induced damage. We have also been able to damage and cut inorganic nanostructures (boron-nitride nanotubes), extending this caveat to SEM work on all sensitive nanomaterials.

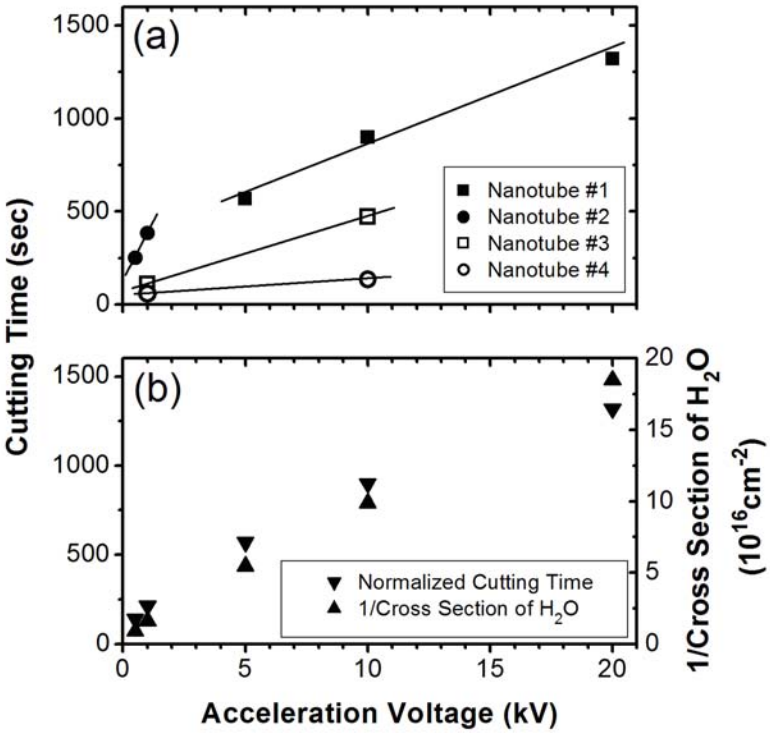

Figure 4.4: Cutting time vs. acceleration voltage. (a) Cutting times for multiple cuts on several nanotubes at different electron beam energies. The dashed lines are guides for the eye. (b) Normalized cutting data from three nanotubes at different electron beam energies. The inverse of the total ionization cross section for water molecules as a function of electron energy is also plotted, and follows the same trend.

Part III

Device integration

Chapter 5

Nanotube nanomotor

5.1 Multiwalled carbon nanotube bearings

The individual shells in a high quality multiwalled carbon nanotube (MWCNT) interact via weak van der Waals bonds that can easily be overcome. This was first demonstrated by the realization of a linear MWCNT bearing by Cumings and Zettl [9], in which several inner shells of a MWCNT were partially extracted along the axial direction. Upon release of the extraction force, the inner walls retracted but exhibited no observable frictional dissipation. The retraction was due to the constant restoring force induced by the van der Waals energy, which is directly proportional to the overlap area between shells.

To further characterize the interlayer interactions in MWCNTs, we have constructed rotational bearings, in which one set of shells rotates about another. Since, in this case, the overlap area between inner and outer shells remains constant, we expect not to observe the restoring force measured in the linear case. To measure the relevant forces and to observe rotational motion, we have integrated MWCNTs into nanoelectromechanical

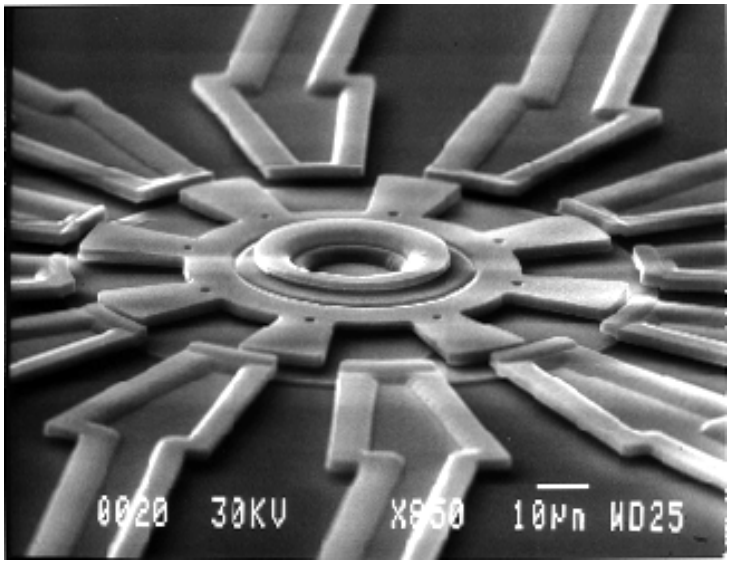

Figure 5.1: A silicon-based microelectromechanical motor developed at Berkeley. The scale bar is 10 μm. Adapted from [75].

systems (NEMS) that can be driven and probed by externally applied electric fields.

5.2 Nanoelectromechanical systems

In recent decades there have been dramatic parallel advances in the miniaturization of mechanical and electromechanical devices [75]. One particularly striking example is the silicon micromotor developed in Richard Muller's group at Berkeley [76], shown in Figure 5.1. Following the development of these microscale devices, an intense interest has developed in the creation of next generation synthetic nanoelectromechanical systems [77, 78].

Although devices have been made by scaling down existing microelectromechanical systems (MEMS), the workhorse methods and materials of MEMS technology are not universally well suited to the nanoscale. Ultra-small silicon-based systems fail to achieve desired high-Q mechanical resonances due to dominant surface effects and thermoelastic damping,

and limitations in strength and flexibility compromise silicon-based high performance actuators [79, 80]. On the other hand, the unusual mechanical and electronic properties of carbon nanotubes (including favorable elastic modulus and tensile strength, high thermal and electrical conductivity, and low inter-shell friction of the atomically smooth surfaces [81, 82]) suggest that nanotubes may serve as important NEMS-enabling materials.

5.3 Nanomotor design and fabrication

We have developed a fully synthetic nanoscale electromechanical actuator incorporating a rotatable metal plate, with a multi-walled carbon nanotube serving as the key motion-enabling element. The overall size scale of our actuator is of order ~ 300 nm and its components are integrated on a silicon chip. Low level externally applied voltages precisely control the operation speed and position of the rotor plate. Repeated oscillations of the rotor plate between positions 180° apart, as well as rotations of 360°, have been demonstrated with no signs of wear or fatigue. Unlike existing chemically driven bio-actuators and bio-motors, our fully synthetic NEMS actuator is designed to operate over a wide range of frequency, temperature, and environmental conditions, including high vacuum and harsh chemical environments.

5.3.1 Architecture

Figure 5.2 shows the conceptual design of the electromechanical rotational actuator. The rotational element (R), a solid rectangular metal plate serving as a rotor plate, is attached transversely to a suspended support shaft. The support shaft ends are embedded in electrically conducting anchors (A1, A2) that rest on the oxidized surface of a silicon

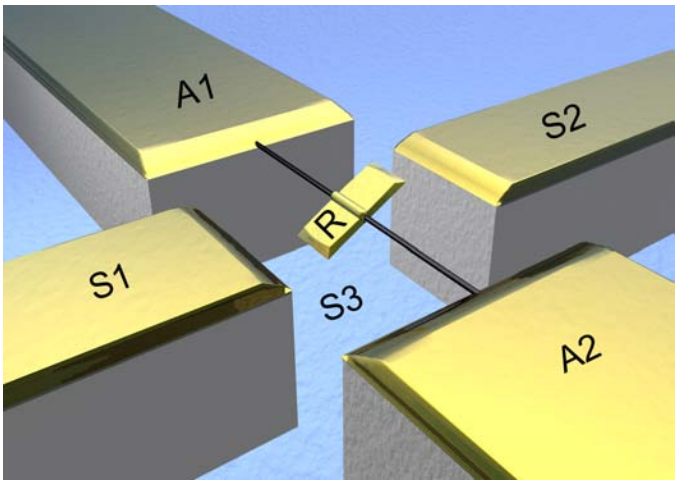

Figure 5.2: Conceptual drawing of the nanotube rotational actuator. A metal plate rotor (R) is attached to a multiwalled carbon nanotube which acts as a support shaft and is the source of rotational freedom. Electrical contact to the rotor plate is made via the nanotube and its anchor pads (A1, A2). Three stator electrodes, two on the SiO_2 surface (S1,S2) and one buried beneath the surface (S3), provide additional voltage control elements. The SiO_2 surface has been etched down to provide full rotational freedom for the rotor plate.

chip. The rotor plate assembly is surrounded by three fixed stator electrodes: two in-plane stators (S1, S2) are horizontally opposed and rest on the silicon oxide surface, and the third gate stator (S3) is buried beneath the surface. Four independent (dc and/or appropriately phased ac) voltage signals, one to the rotor plate and three to the stators, can be applied to control the position, speed, and direction of rotation of the rotor plate. The key component in the assembly is a single MWCNT, which serves simultaneously as the rotor plate support shaft and the electrical feedthrough to the rotor plate; most importantly it is also the source of rotational freedom.

5.3.2 Fabrication process

Our NEMS actuator was constructed using lithographic methods shown schematically in Figure 5.3. MWCNTs, synthesized by the standard arc technique [3], were suspended in 1,2-dichlorobenzene and deposited on degenerately doped silicon substrates cov-

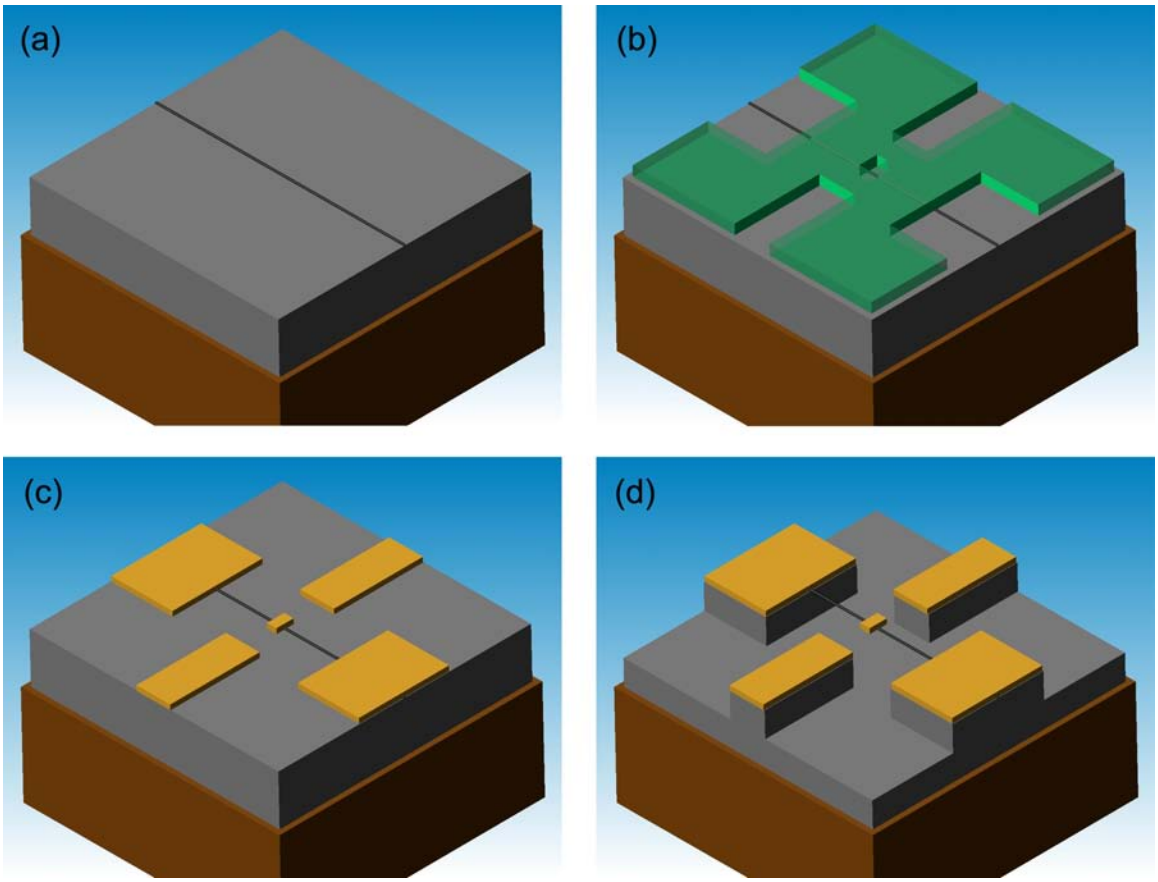

Figure 5.3: The nanomotor fabrication process. (a) Multiwalled carbon nanotubes are deposited on a clean silicon/silicon oxide surface and are located by SEM. (b) Electron beam lithography is used to pattern PMMA into an evaporation mask on the silicon oxide surface in alignment with the deposited nanotubes. (c) Gold (with a chromium adhesion layer) is evaporated onto the surface, and the remaining PMMA is removed. (d) Hydrofluoric acid is used to etch away some of the silicon oxide, suspending the nanotube/rotor assembly.

ered with 1 μm of thermally grown SiO_2. The nanotubes were located with respect to pre-patterned alignment marks on the SiO_2 surface using an atomic force microscope or a LEO 1550 Scanning Electron Microscope (SEM). The remaining actuator components (in-plane rotor plate, in-plane stators, anchors, and electrical leads) were then patterned using electron beam lithography. A single layer of electron beam resist (PMMA 5.5% 950K in chlorobenzene) was spun on the samples at 4kRPM for 45 seconds and subsequently baked in air at 150°C for 2 hours. The resist was then patterned using NPGS software

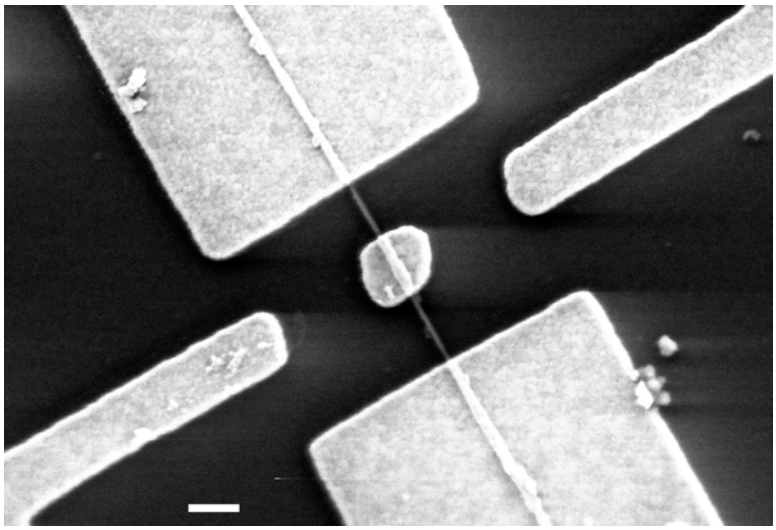

Figure 5.4: SEM micrograph of a nanotube rotational actuator just prior to HF etching. The scale bar is 300 nm.

on a JEOL 6400 SEM, and developed in MIBK:IPA 1:3 for one minute. Gold (∼90 nm) with a chromium adhesion layer (∼10 nm) was then thermally evaporated and lifted off in acetone. The Cr/Au was subsequently annealed at 400°C to ensure better electrical and mechanical contact between the Cr and the MWCNT. An HF etch was used to remove roughly 500 nm of the SiO_2 layer to provide clearance for rotation of the rotor plate. The degenerately doped silicon substrate (typically used as the gate electrode in three-terminal nanotube field effect devices [83, 84]) here serves as the gate stator. Figure 5.4 shows an actuator device prior to etching. Typical rotor plate dimensions were 250-500 nm on a side.

5.4 Operation and characterization

5.4.1 Initial bearing release

Initial actuator characterization was carried out in situ inside the SEM. We found that applying voltages up to 50 Vdc between the (slightly asymmetric) rotor plate and the

gate stator generated a net torque sufficient to visibly rotate the rotor plate (up to 20° deflection). When the applied voltage was removed the rotor plate would rapidly return to its original horizontal position. Using a finite analysis program (FEMLAB, a commercially available plug-in for MATLAB) and a model of our actuator geometry together with the measured deflection and applied voltages, we determine for our devices typical "as produced" effective torsional spring constants of $10^{-}15$ to $10^{-}12$ N·m.

Evaluation of the MWCNT shear modulus (assuming a continuum mechanics model [85]) necessitates knowledge of the outer diameter of the nanotube. We were able to determine the outer diameters of the MWCNTs in our devices to within 20 percent and found that they ranged from 10 to 40 nm, which was consistent with high resolution TEM measurements of MWCNTs from the same preparation batch. TEM imaging also showed the MWCNTs to be of high structural quality, composed of concentrically nested cylindrical tubules with no obvious defects. For a hollow cylinder clamped on both ends, the formula relating spring constant to shear modulus is

$$\kappa = \frac{2\pi(r_{out}^4 - r_{in}^4)G}{l} \tag{5.1}$$

where r_{in} and r_{out} are the inner and outer radii, l is the length, and G is the shear modulus. Since the coupling between walls in our high quality, arc-grown nanotubes is minimal, we use values for the outer wall and assume thickness equal to the interlayer spacing 0.34 nm. For a 10 nm diameter MWCNT with an effective length of 2 μm, our results yield a shear modulus of 100 to 300 GPa. These ranges for torsional spring constant and shear modulus overlap those of more direct measurements employing a suspended MWCNT subjected to torsional deflection via an atomic force microscope tip [86, 87].

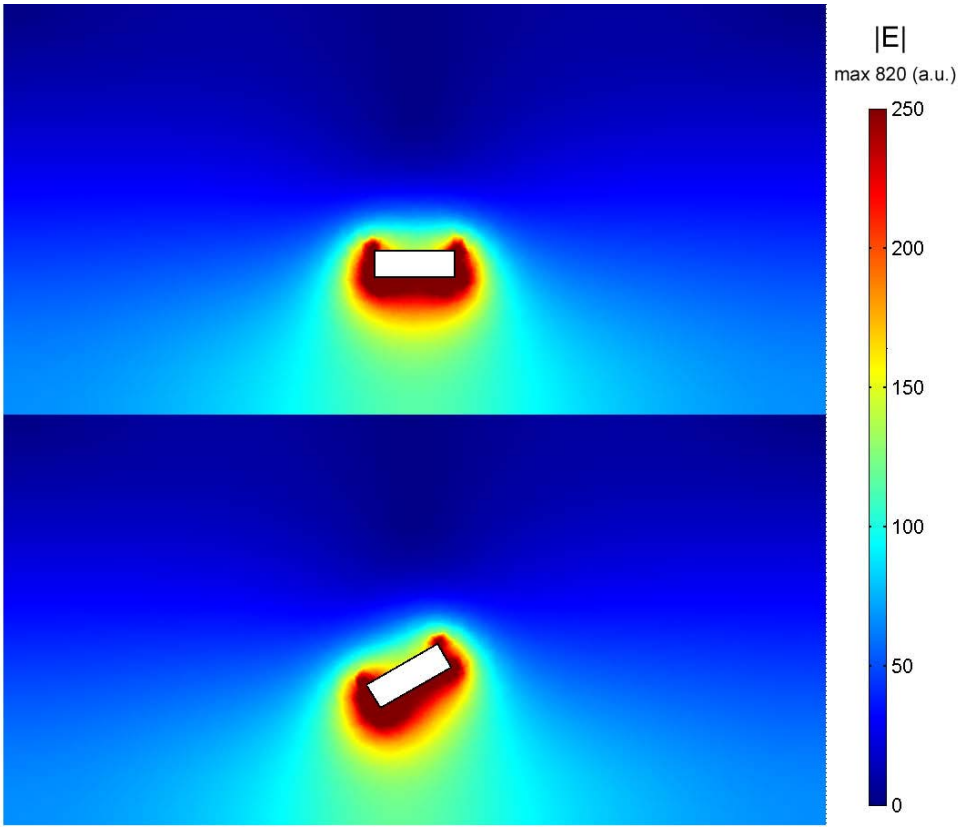

Figure 5.5: Calculated electric fields in the vicinity of the nanomotor device for two angular positions, computed using finite element analysis. By integrating the total electrostatic energy of the system as a function of angular position we are able to calculate the torsional spring constant of the MWCNT.

Although the actuator devices just described have a number of extremely useful characteristics (including predicted torsional oscillator mechanical resonance frequencies of order tens to hundreds of MHz), the strong torsional spring constant effectively prevents large low-frequency angular displacements. For large displacement operation we modified the MWCNT support shaft in an attempt to exploit the intrinsic low-friction bearing behavior afforded by the perfectly nested shells of MWCNTs [81, 82, 9, 88]. The modification consists of removing or compromising one or more outer MWCNT shells in the region between the rotor plate and the anchors. Several methods were used to achieve the modification in the SEM, including reactive-ion etching, application of current through the

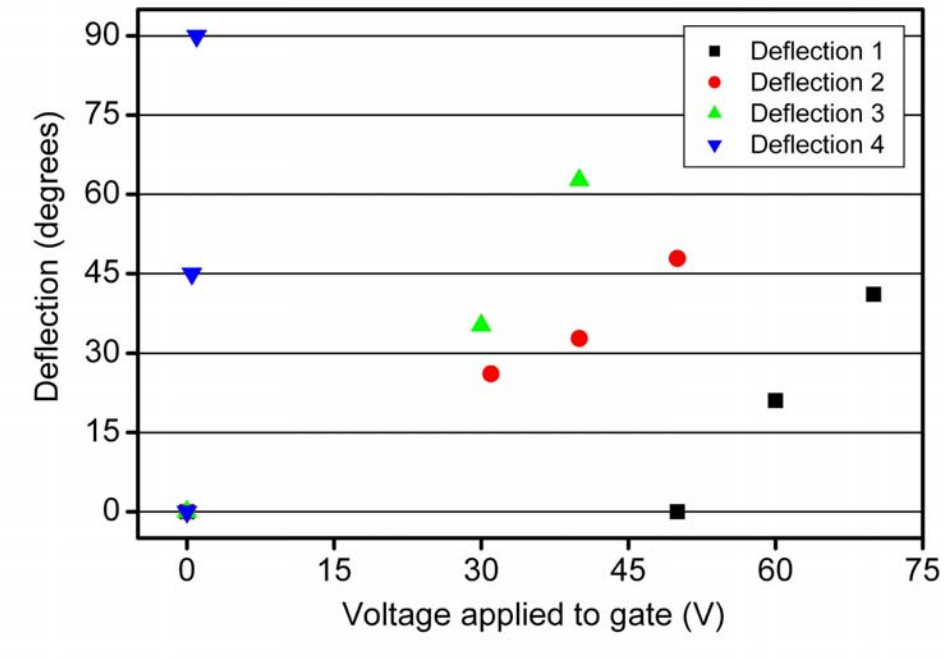

Figure 5.6: Deflection vs. gate voltage for consecutive runs. After deflection 3, the rotor became rotationally free and could be moved through entire rotations by voltages on the order of 1 V.

nanotube to remove outer nanotube shells [39, 16], and selective nanotube bond-damage induced by the SEM electron beam. These methods are described in detail in Section 5.5.

A particularly simple yet effective in situ MWCNT modification method, and the one used on the devices to be described below, was to mechanically fatigue and eventually shear the outer nanotube shells by successive application of very large stator voltages. We found that applied gate stator voltages of order 80 Vdc would torque the outer nanotube shells past the elastic limit, eventually leading to partial or complete failure of the outer nanotube shells and a resulting dramatic increase in the rotational freedom of the rotor plate (see Figure 5.6). In the "free" state, the rotor plate was still held in position axially by the intact nanotube core shells, but could be azimuthally positioned, using an appropriate com-

bination of stator signals, to any arbitrary angle between 0° and 360°. Once so positioned, the rotor plate nominally remained in place even with all stator voltages reduced to zero, eventually drifting to a vertical (0° or 180°) position only under the charging influence of the SEM imaging electron beam.

5.4.2 DC stepping

Figure 5.7 shows a series of still SEM images recorded of an actuator device in the free state, being walked through one complete rotor plate revolution using quasi-static dc stator voltages. The stator voltages, never exceeding 5 V, were adjusted sequentially to attract the rotor plate edge to successive stators. By reversing the stator voltage sequence, the rotor plate rotation could be reproducibly reversed. If the applied voltages were removed, the rotor would remain in the same position for several minutes. Eventually, however, due to the charging influence of the electron beam, the rotor would be pulled back to a vertical position.

5.4.3 AC driving

Finite frequency operation of the actuator was performed by using a variety of suitably phased ac and dc voltage signals to the three stators and rotor plate. In one simple operation mode, we applied out-of-phase common-frequency sinusoidal voltages to stators S1 and S2, a doubled-frequency signal to S3, and a dc offset to the rotor plate R, as given

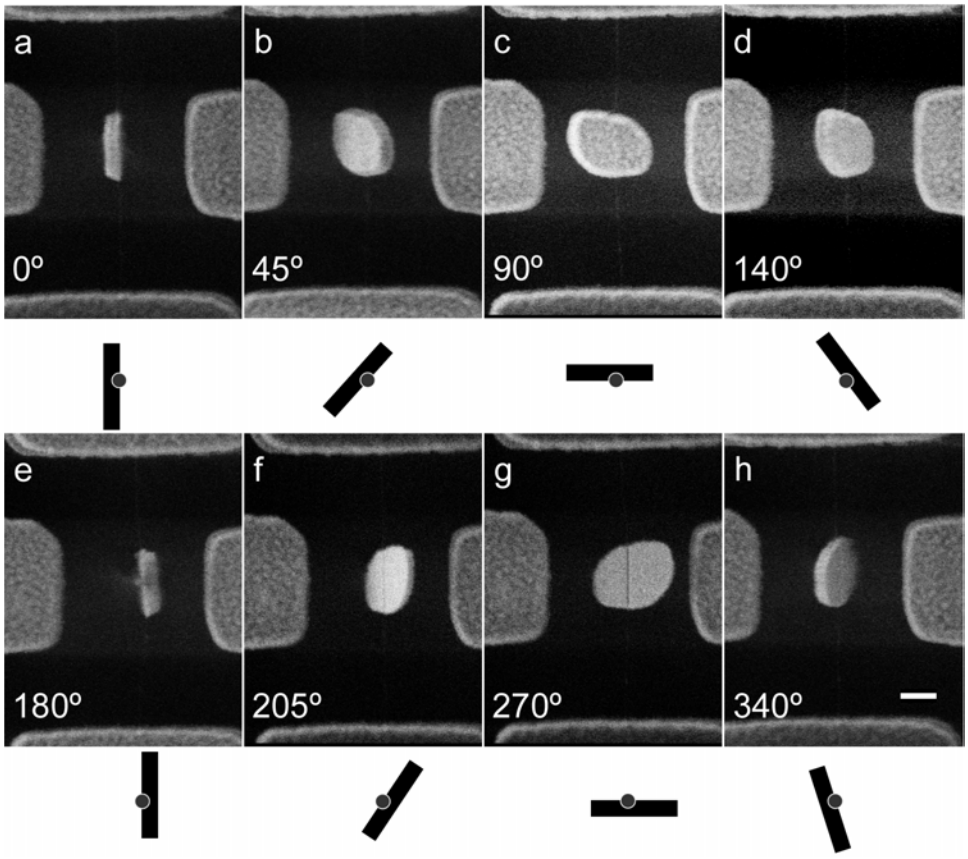

Figure 5.7: DC stepping: a series of SEM images showing the actuator rotor plate at different angular displacements. The MWCNT, barely visible, runs vertically through the middle of each frame. The schematic diagrams located beneath each SEM image illustrate a cross sectional view of the position of the nanotube-rotor plate assembly. The scale bar is 300 nm.

by:

$$\begin{aligned} \text{S1} &= V_0 \sin(\omega t) \\ \text{S2} &= V_0 \sin(\omega t - \pi) \\ \text{S3} &= V_0 \sin(2\omega t + \pi/2) \\ \text{R} &= -V_0 \end{aligned}$$

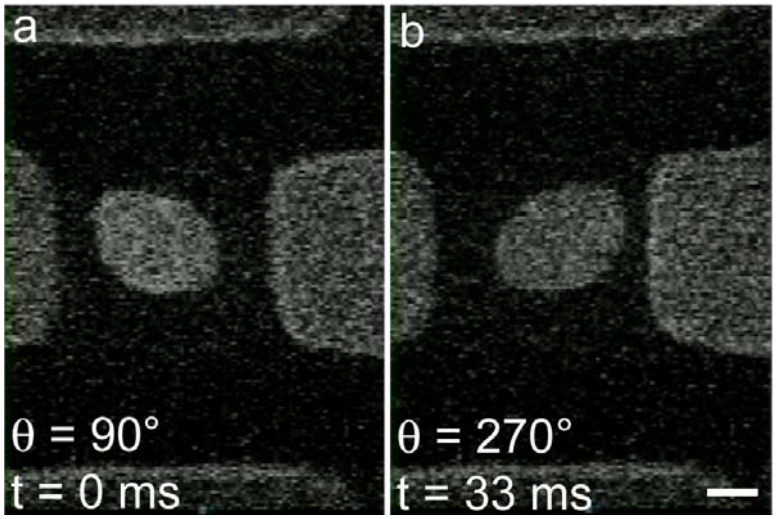

Figure 5.8: AC driving: two SEM images captured from a video recording of an ac-voltage-driven actuator "flipping" between the extremal horizontal positions (90° and 270°). The two images are taken one video frame (33 ms) apart. Rapid, large-amplitude rotor plate oscillations could be sustained nearly indefinitely with no noticeable wear or degradation in actuator operation. The MWCNT is not visible in these images, but it runs vertically through the middle of each frame. The scale bar is 300 nm.

Although the resulting spatial and temporal drive forces are actually quite complex, roughly speaking this sequence allowed the rotor plate to be sequentially electrostatically attracted to the next available stator. Using this drive sequence we were reliably able to alternately flip the rotor plate between the extremal horizontal (90° and 270°) positions.

Although in principle very high frequency operation should be possible (restricted only by the stripline bandwidth of the leads and, ultimately, inertial effects of the rotor plate), our SEM image capture rate limited direct real-time observations of rotor plate oscillations to frequencies of typically several Hertz. We found that the transitions between the extremal horizontal positions could be made faster than the image video capture rate of 33 msec. Figure 5.8 shows two images of the actuator, recorded 33 msec apart, showing the rotor plate respectively in the 90° and 270° positions. We were able to rotationally drive actuators in this fashion for many thousands of cycles, with no apparent wear or degradation

in performance. In this configuration, the MWCNT clearly serves as a reliable, presumably wear-free rotational degree of freedom granting NEMS element. This characterization was performed in a pressure range of 10^{-6} to 10^{-5} Torr, although we anticipate reliable operation at higher pressures. We note that our actuator is the first true MWCNT-based NEMS device, in that it fully integrates electronic control and mechanical response. This distinguishes it from previous nanotube-based mechanical devices which require relatively large and complex external control systems (such as piezo-driven manipulators) to achieve operation [86, 87, 39, 88, 89].

Our MWCNT-based actuators have obvious MEMS/NEMS applications potential. The rotational metal plate could serve as a mirror, with obvious relevance to ultra-high-density optical sweeping and switching devices (our total actuator size is just at the limit of visible light focusing). The rotating plate could also serve as a paddle for inducing fluid motion in microfluidics systems, as a gated catalyst in wet chemistry reactions, as a bio-mechanical element in biological systems, or as a general (potentially chemically functionalized) sensor element. It is also possible that the charged oscillating metallic plate could be used as a transmitter of electromagnetic radiation. Using methods to align nanotubes, it should be possible to fabricate arrays of orientationally ordered nanotube-based actuators on substrates.

5.5 Other methods for bearing release

We have explored several alternate methods for bearing creation, since the torsional shear method, while effective in freeing the nanotube for rotational movement, also presents several limitations. We found the torsional method to be effective only on thinner

MWCNTs, of diameter less than approximately 20 nm. For thicker nanotubes, the applied electric field required to initially rotate the device exceeded the breakdown strength of the dielectric layer. For thinner nanotubes, the voltages necessary to shear the outer wall would vary depending upon the nanotube diameter and the exact dimensions of the metal rotor. Thus, individualized treatment was necessary to free each device.

Another limitation of the torsional shear method is that it does not allow us to fully investigate the rotational bearing nature of the MWCNT. Torsional stress appears to damage the outer wall of the nanotube only locally, without affecting the rest of its length. Thus the position of the rotor along the axis of the nanotube remains fixed, with the remaining sections of outer shell preventing any axial motion, as in Figure 5.12 (b). This limits the full bearing nature of the devices and prevents us from simultaneously exploiting both linear and rotational freedom. If we were able to do so, we could investigate chiral mismatch and the possibility of the axle bearing assembly undergoing a screw-like effect as it is translated rotationally [90, 91].

5.5.1 Electrically driven vaporization

Here I discuss the use of electrically driven vaporization (EDV) to selectively remove the outer walls of the multiwalled carbon nanotube, as described in Chapter 2. In principle, the controlled removal of these walls creates a desirable geometry in which the rotational freedom of the bearing can be easily characterized. Moreover, EDV removes large sections of the outer wall, after which the rotor should be able to slide along the inner core as a combined linear and rotational bearing.

We find that good electrical contact to the nanotubes is necessary for controlled

vaporization to take place. Attempts made on devices with high resistance (> 50 kΩ) result in breakage of the nanotube with no intermediate thinning observed. Devices with resistances lower than 10 kΩ reliably achieved stepwise current decays at constant bias voltages. These stepwise current decays sometimes exhibited current steps of equal magnitude (on the order of 10-20 μA, varying from device to device), but were often found to vary greatly (in the range of 5 to 25 μA) on a single device. The exact mechanism underlying these steps is still unknown.

Our first attempt to use EDV in our devices consisted of passing current from one anchor to the other, in the hope that sections of the outer walls would be removed on both sides of the rotor. We found, however, that once a shell failed on one side of the rotor (determined by scanning electron microscope (SEM) imaging of thinning of the MWCNT), all subsequent vaporization would happen on the same side, with no apparent failures occurring on the other side. This could not be remedied by reversing the bias, and would continue all the way to complete breakage of the nanotube.

We were able to vaporize sections of the MWCNT on both sides of the rotor by making electrical contact to the center of the MWCNT and passing current through each side separately. The contact was made by adding an extra lithography step in the device fabrication, during which a thin strip of metal is evaporated to form a bridge between the stator electrodes and the rotor, as shown in Figure 5.9. However, this contact must later be removed for the device to be able to function. Therefore, we tried aluminum and titanium, both of which, due to their very high etch rates in hydrofluoric acid, quickly disappear in the subsequent buffered hydrofluoric acid etch used to undercut and suspend the device. Due to the propensity of aluminum towards oxidation we found titanium to be the ideal

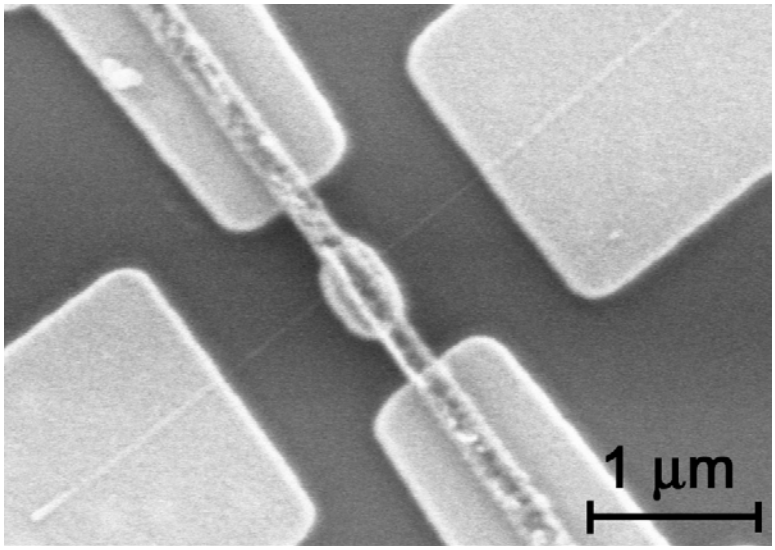

Figure 5.9: A temporary titanium short bridges the stators and rotor of a nanomotor device, allowing for the selective vaporization of the nanotube on either side of the rotor.

metal for this temporary contact.

Once a device was contacted with a titanium short we were able to pass current from the stators to either anchor in turn. It proved difficult, however, to induce equal amounts of damage on both sides. Due to contact variances, the two resistances were rarely identical, so the two sides generally required different levels of voltage and current to begin the breakdown process. Moreover, the nanotubes would sometimes completely fail without exhibiting any current steps at all, or step-wise breakdown would occur so rapidly that we could not controllably stop it. These effects may have been due to induced rapid annealing of the gold or titanium contacts. The corresponding drop in contact resistance would create a sudden rise in the voltage actually applied to the nanotube, potentially leading to catastrophic failure.

Upon testing the devices in situ in an SEM, we found that many would have significantly reduced torsional spring constants. Most would not, however, exhibit free

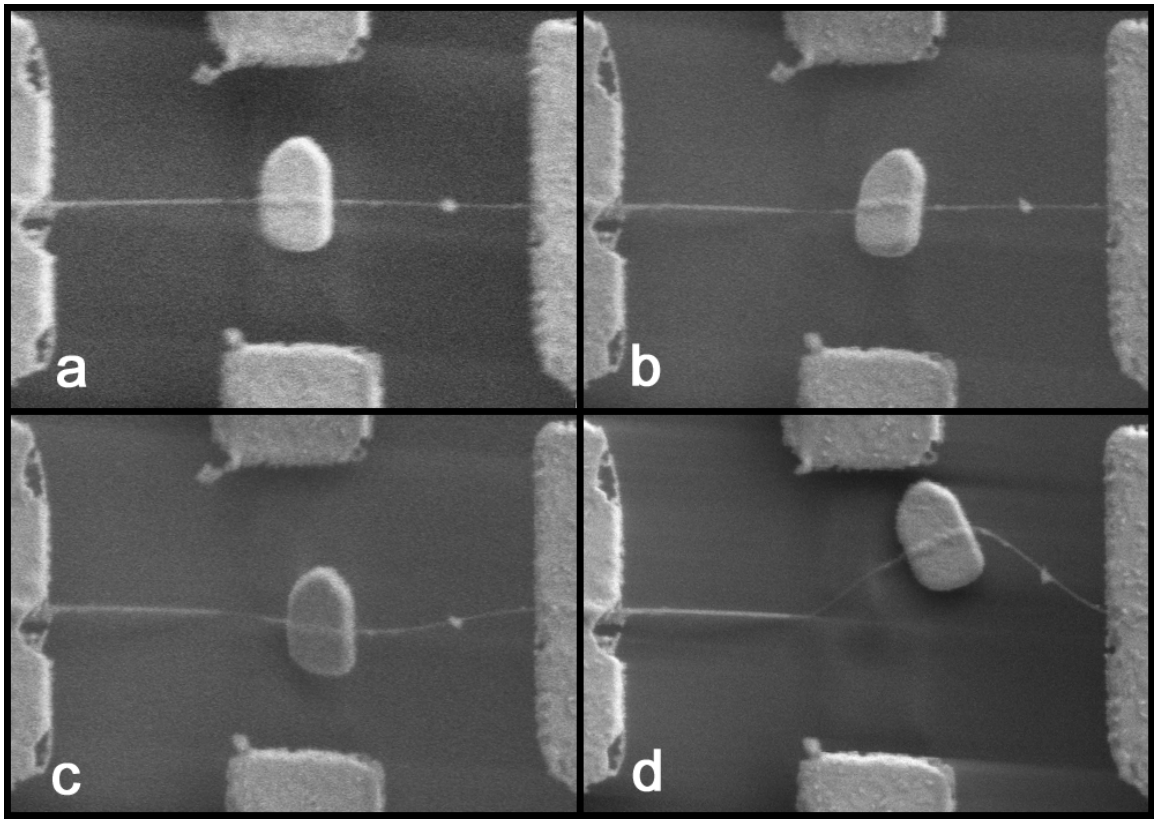

Figure 5.10: Telescopic failure of a MWCNT that has undergone EDV on both sides of the rotor paddle. The images are in sequential order, showing increasing extension: (a) No voltages applied. (b) Rotor pulled down towards substrate (voltage applied to back gate). (c) Rotor pulled towards lower stator. (d) Rotor pulled towards upper stator (though hard to see, the nanotube is still continuous).

bearing behavior - they would eventually break without showing the freedom of motion seen in the torsionally freed devices. We surmise that in these cases one side of the nanotube had been rotationally freed while the other remained intact and acted as a torsional spring.

Despite these difficulties we were still able to learn more about the bearing nature of our devices. We repeatedly saw one particularly interesting failure mode. Instead of snapping at some point along its length (as was seen, for example, in devices freed by reactive ion etching), the MWCNT would telescope out, dropping the rotor to the underlying surface, as shown in Figure 5.10. Similar telescoping behavior in MWCNTs has been observed in

TEM experiments [9]. We were able to extend the MWCNT even further by subsequently attracting the rotor to the two side stators. Other devices failed similarly, sometimes combining telescopic extension with rotation of the paddle.

We submit two possible explanations for this failure mode. EDV may be severing internal, unexposed shells [43], in which case we are seeing the result of a break in the inner core near to the EDV-induced gap in the outer walls. We find it more likely, however, that the inner core is indeed decoupled from the outer shells and free to move, both linearly and rotationally, and we simply removed too many shells, making the exposed section of the core too flexible to support the rotor. Subsequent experiments with an alternate geometry (in which EDV is performed first and the rotor is attached directly to the exposed inner core [40]) support this interpretation. With better contacts and more precise control this method should prove viable in our actuators as well.

5.5.2 Reactive ion etching

Reactive ion etching (RIE) is commonly used in semiconductor fabrication to selectively remove material in a controlled and uniform manner. This motivated us to try to reactively etch a MWCNT, hoping to controllably remove the entire outer wall irrespective of its diameter. Given the common use of oxidation to purify raw MWCNT soot we chose to use O_2 as our etching gas. Samples containing suspended MWCNT devices (with rotors and stators already in place) with varying nanotube diameters were placed in a Plasma-Therm PK-12 Parallel Plate Plasma Etcher. The samples were etched in O_2 plasmas at a pressure of 100 mTorr and a power of 15 W for up to 40 seconds.

After etching, the devices were placed in an SEM for in situ analysis of their tor-

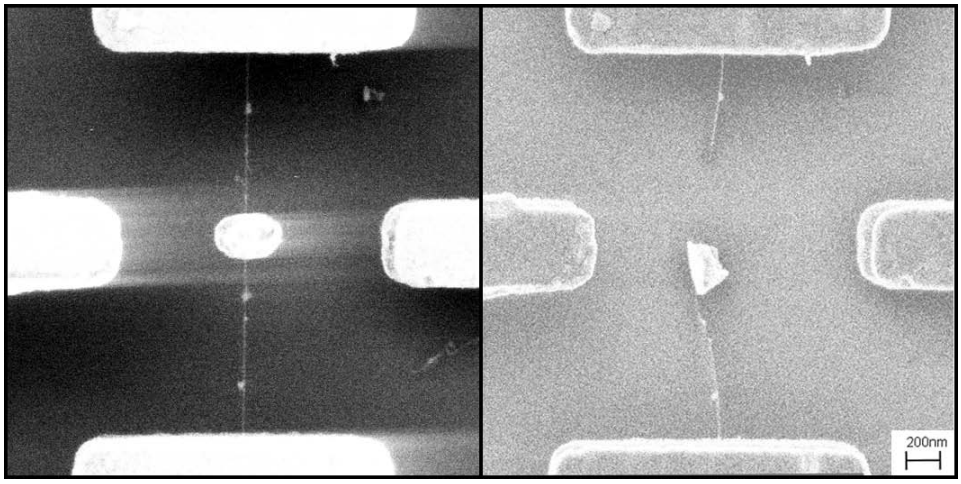

Figure 5.11: SEM micrographs of a MWCNT actuator treated by reactive ion etching. The image on the left shows it in its pristine state. The device was then subjected to RIE, after which the torsional spring constant was greatly reduced. Shortly after testing began, however, the device failed, shown in the image at right. The scale bar is 200 nm.

sional behavior. We found that devices subjected to identical plasma treatment had their torsional strength weakened to varying degrees. Some devices even appeared to be free, requiring only low applied voltages for large angular displacements, and several times the rotors were already in the vertical position (rotated 90°) when first imaged by SEM. Meanwhile, other devices, while weakened, still had appreciable torsional strength, and could only be slightly deflected with large applied voltages. We also found several devices that appeared to be stuck to the underlying silicon oxide surface. The MWCNTs were slightly extended, to the point where the rotor could not rotate without touching the substrate. From our experiences we have found that once a rotor has touched the substrate it is very difficult to overcome the van der Waals attraction and pull it out of contact.

Unfortunately, even those devices that appeared to be free were prone to failure, unlike the torsionally sheared devices reported above. After several rotations the MWCNT would snap somewhere along its length, as shown in Figure 5.11. Previous work on O_2

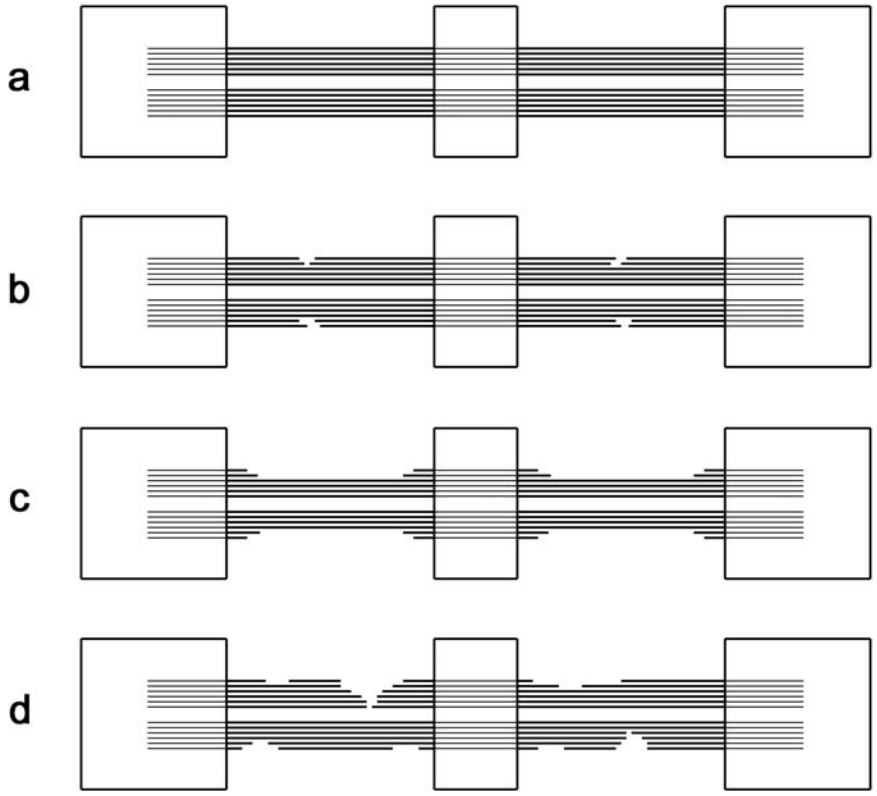

Figure 5.12: A model of bearing creation by various methods: (a) An actuator in its pristine state, with all walls intact. Anchors hold the MWCNT on each end, with a rotor paddle suspended in the middle. (b) The presumed result of torsional shearing. Though free to rotate, the rotor cannot slide along the nanotube. (c) An alternate geometry, in which the rotor can both spin and shuttle along the inner core. (d) The apparent outcome of reactive ion etching, with localized etch pits causing extensive damage to the inner core before rotational freedom can be achieved.

etching of graphite surfaces provides insight as to the mechanism of these failures [92]. It was found that instead of etching the surface uniformly, layer by layer, deep etch pits develop at defect locations, as diagrammed in Figure 5.12 (d). The presence of etch pits would explain both the sudden failure of the MWCNTs and the observed variability in the effect of the same plasma dose on different MWCNTs.

While RIE with O_2 plasma is promising and was successful in rotationally freeing the tubes, the lack of uniformity in rotational freedom from tube to tube, their abrupt snapping failure, and the common problem of adhesion to the surface demonstrate that

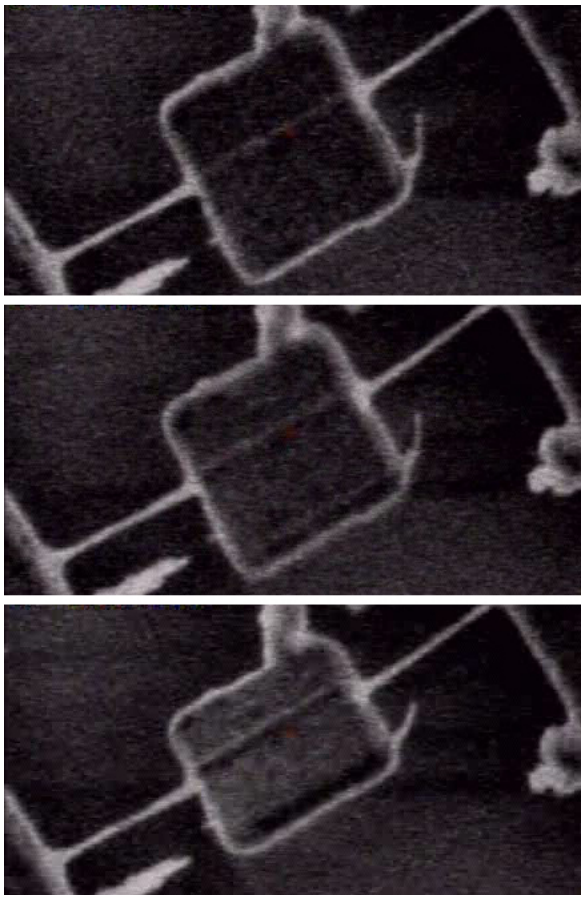

Figure 5.13: SEM micrographs of mechanical deflection of a nanomotor device prior to bearing release.

more work on refining this technique is in order.

5.5.3 Mechanical shearing

We also attempted to create free bearing structures by mechanically pushing on the rotor, allowing us to exert greater forces than available through electrostatics. Using a custom built nanomanipulator (described in Appendix B), we were able to deflect the rotor paddle, as shown in Figure 5.13. A scanning tunneling microscope tip (essentially, a very sharp wire) was used to push the upper edge of the rotor towards the silicon substrate. We were unable to provide enough deflection to free the bearing, however, and the outer wall

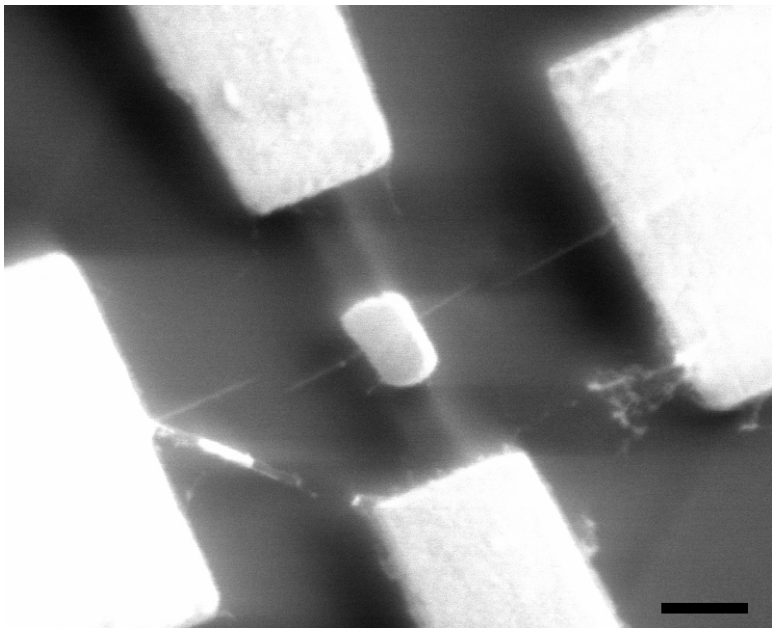

Figure 5.14: A nanomotor device after being cut by the SEM electron beam. The scale bar is 400 nm.

remained intact.

5.5.4 Electron beam cutting

Finally, we attempted to damage the outer walls of the multiwalled carbon nanotube using the electron beam cutting method. This method was successful in creating loose torsional springs, but these devices would usually break after a short period of operation. Indeed, this could be expected: the cutting process does not favor the outer walls, and instead cuts into the top surface of the nanotube, both damaging the inner walls and leaving the lower surface of the outer walls intact. Nonetheless, our attempt proved to be a useful test and inspired the measurements discussed in detail in Chapter 4.

Chapter 6

Highly aligned nanotube arrays for large scale device fabrication

6.1 Introduction

The utility of the individual rotational actuators described in the previous chapter can be significantly increased by their incorporation into multiple device arrays. For example, such arrays could serve in a variety of applications, including adaptive optics, high frequency mechanical filters, mass sensors, and microfluidic gates and pumps. In this chapter, I describe a novel method we have developed to precisely position arc-grown multiwalled carbon nanotubes into ordered arrays as a means of obtaining arrays of rotational actuators. The techniques described below can also be used to position other nanostructures into virtually any arrangement on a properly pretreated planar surface.

6.2 Existing methods and their limitations

6.2.1 Chemical vapor deposition

A fundamental challenge in the development of NEMS arrays (and of nanotube- and nanowire-based devices in general) is the large-scale controlled placement of molecular sized building blocks. Methods based on chemical vapor deposition (CVD) avoid this problem by, for example, growing nanotubes directly on the substrate where they ultimately will be located [93]. Unfortunately, such methods are unable to produce high quality multi-walled carbon nanotubes as are often required for NEMS applications [32, 9, 94]. Moreover, CVD is usually a high temperature process, which can severely limit compatibility with substrate materials or other system components. Hence there is much interest in low temperature techniques to aid in the selective placement and alignment of prefabricated nanostructures.

6.2.2 Fluidic techniques

There has been significant progress in developing fluidic techniques for aligning nanowires [95] and nanotubes [96, 97, 98], and various functionalization schemes have been explored for placing nanotubes on particular areas of a substrate [99, 100, 101]. Unfortunately, most of these methods necessitate rather complex substrate topology or involved and limiting chemistry. We have developed a combination of novel room temperature methods for both aligning and selectively depositing nanotubes onto a topologically benign surface. Using these methods, which can easily be integrated into semiconductor manufacturing processes, we have fabricated arrays of aligned torsional NEMS devices based on MWCNTs.

6.3 Fabrication process

6.3.1 Overview

Figure 6.1 outlines the fabrication process. High quality MWCNTs are grown using the arc-plasma method and are dispersed in solution. A silicon/silicon oxide substrate is coated with electron beam resist, which is then soaked in acetone to leave only a very thin polymer layer. The substrate is then selectively exposed to an electron beam in situ in an FEI Sirion XL30 scanning electron microscope, which activates the adhesive properties of the polymer layer. The MWCNT solution is then deposited onto the spinning substrate, causing the MWCNTs to align with the flow and adhere in the targeted regions. The alignment and adhesion parameters are discussed in detail in the next section. Finally, standard electron beam lithography is used to pattern paddles and anchors on top of the MWCNTs, which are then suspended by etching down the supporting oxide layer with buffered hydrofluoric acid.

Figure 6.2 (a) shows one section of a prototype array of torsional actuators that we have produced. An individual actuator, as shown in Figure 6.2 (b), consists of five main elements: two anchors, a suspended MWCNT, a suspended rectangular metal mirror or paddle, and the conducting back gate buried beneath the surface. The suspended MWCNT serves both as the torsional element and the electrical connection to the gold paddle mounted at its center. The two gold anchors hold the ends of the MWCNT in place. Asymmetric electrostatic fields applied between the gold paddle and the back gate create an attractive force which causes the paddle to undergo an angular displacement and the MWCNT to twist. If the outer MWCNT shell is compromised, free rotational motion of the actuator becomes possible.

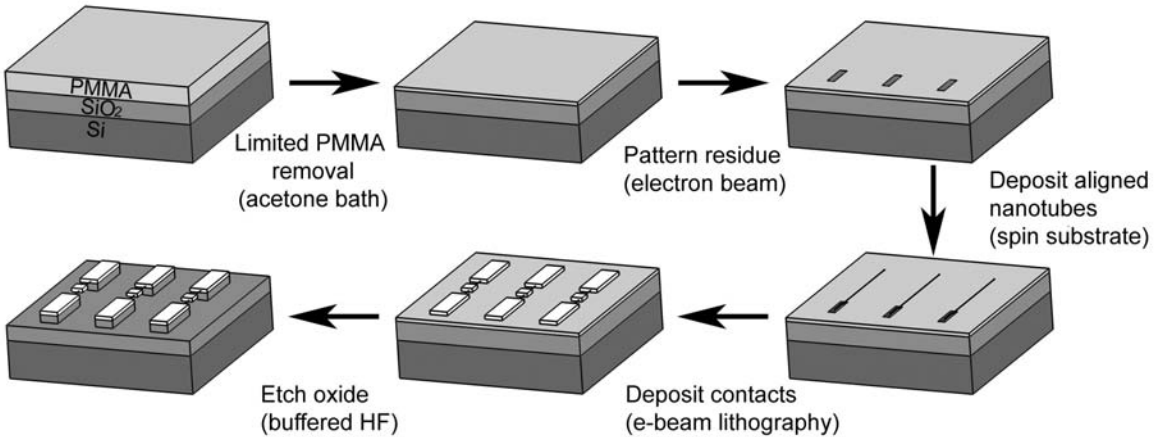

Figure 6.1: Array fabrication process. A silicon/silicon oxide wafer is coated with electron beam resist (not to scale) which is then mostly removed in an acetone bath. The remaining residue is then patterned by exposure to an electron beam in situ in an SEM. MWCNTs are deposited out of solution onto the spinning substrate, causing them to align with fluid flow and adhere to the exposed pattern. Standard electron beam lithography is then used to deposit anchors and paddles. Finally, the silicon oxide is partially etched down to suspend the nanotube-paddle assemblies.

Actuators of the type shown in Figure 6.2 have been previously individually fabricated and characterized [8, 32, 86]. Effective torsional spring constants range from 10^{-15} to 10^{-12} N·m, depending on the MWCNT geometry. Typical devices have moments of inertia of 10 to 30 kg·m, yielding resonance frequencies in the tens of MHz range (with smaller paddle sizes and shorter exposed MWCNT lengths the resonance frequencies can be extended to above 1 GHz). The key advance of the present work is the ability to produce such devices in an array configuration.

6.3.2 Alignment

We describe in detail the key enabling step in the array fabrication process, namely MWCNT targeted deposition and alignment. Our alignment method exploits the surface velocity obtained by a fluid as it flows off of a spinning substrate, and is distinct from previous alignment attempts involving either dielectrophoresis [102] or deposition from a

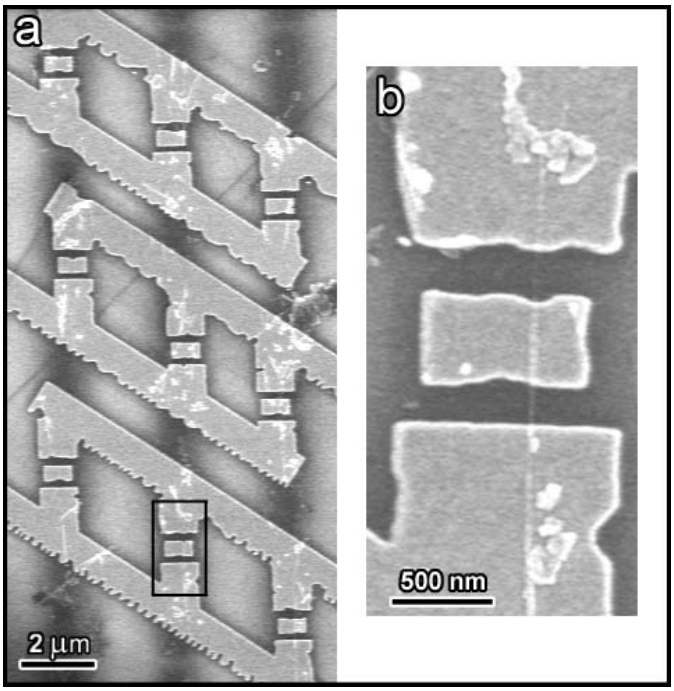

Figure 6.2: An array of nanotube devices fabricated on MWCNTs placed by fluidic alignment and beam-activated adhesion shown prior to the HF etch. (b) Increased magnification image of the nanotube device marked with a black box in (a). The two anchors occupy the top and bottom thirds of the image, with the MWCNT support shaft running vertically between them. The paddle is mounted on the MWCNT in the center of the image and can be driven by voltages applied to the conducting back gate (not visible).

solution driven across a surface by gas [96, 97] or microfluidic flow [95]. We use arc-grown MWCNTs with typical diameters of 10-25 nm as measured by transmission electron microscopy (TEM). The MWCNTs are suspended in orthodichlorobenzene (ODCB) at a concentration of 100 mg/l by ultrasonication in a VWR Model 75D Aquasonic bath for 60 seconds at level 3. TEM observation shows that this level of ultrasonication is enough to separate most MWCNT bundles into individual MWCNTs. The suspension is then pipetted drop by drop onto the center of a silicon substrate mounted on a spincoater rotating at 3000-10000 RPM. The suspension flows radially across and off of the substrate. Once the surface is dry, the next drop is deposited. We find that if the next drop is deposited while

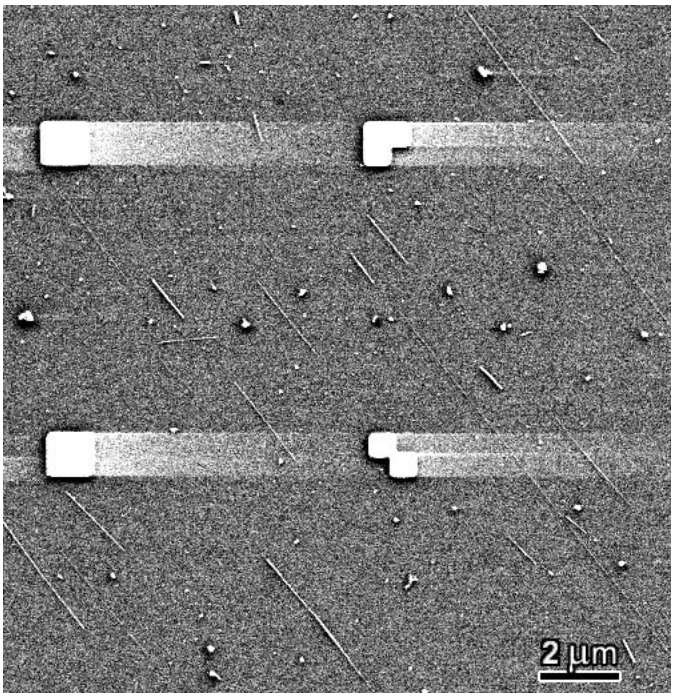

Figure 6.3: Fluidic alignment of MWCNTs by spinning the substrate. A suspension of nanotubes was pipetted onto this sample while it was spinning at 5000 RPM, with the center of rotation 6 mm below and to the right of the area shown. The substrate was in its pristine state before deposition; alignment marks were patterned and deposited afterwards.

the substrate is still wet, the deposition is less dense and contains a larger percentage of unaligned nanotubes.

Figure 6.3 shows the results of a typical deposition. MWCNTs are observed to align with the fluid flow direction (from lower right to upper left in the figure), with longer MWCNTs generally more aligned than shorter segments. From SEM images we observe that typically, 90% of MWCNTs over 1 μm in length lie within $\pm$ 1° and 95% lie within $\pm$ 5° of the direction of fluid flow, a significant improvement over previously reported results [96, 97].

6.3.3 Localized deposition

Although the MWCNTs of Figure 6.3 are aligned, they are still randomly positioned. For many multi-component engineered NEMS devices, including arrays, predetermined positional order is necessary. The deposition process can be further refined by locally treating the substrate to place MWCNTs in target locations. Previous targeting attempts via surface functionalization have been made using self-assembled monolayers (SAMs) with polar functional groups [99, 100, 101]. The success of these techniques is dependent upon the quality of the SAM, however, with degraded performance occurring when more (or less) than a monolayer is deposited [103]. Ideally, localized nanotube deposition should involve a surface layer which is simple to deposit and insensitive to variations in thickness.

Our location targeting method exploits a surface layer that is already present in standard lithographic work and does not require a single monolayer. The layer consists of the residual polymer left behind when resists used in electron beam lithography are removed by an acetone wash. In this work, the resist consisted of a copolymer of 8.5% methacrylic acid (MAA) in methyl methacrylate (MMA) formulated in ethyl lactate at 6% (available from MicroChem Corp.), and was spun-coat at 3000 RPM for 30 seconds onto a silicon substrate with 1 μm of thermally grown oxide. It was then baked on a hot plate at 185°C for 3 minutes and stripped in acetone for 5 minutes. When left untreated, the residual coating actually inhibits nanotube deposition out of ODCB, as evidenced by lower deposition rates than those seen on pristine silicon substrates.

Targeted adhesion of nanotubes by this layer is activated by exposure to the low energy electron beam of a scanning electron microscope (SEM). Figure 6.4 (a) shows the

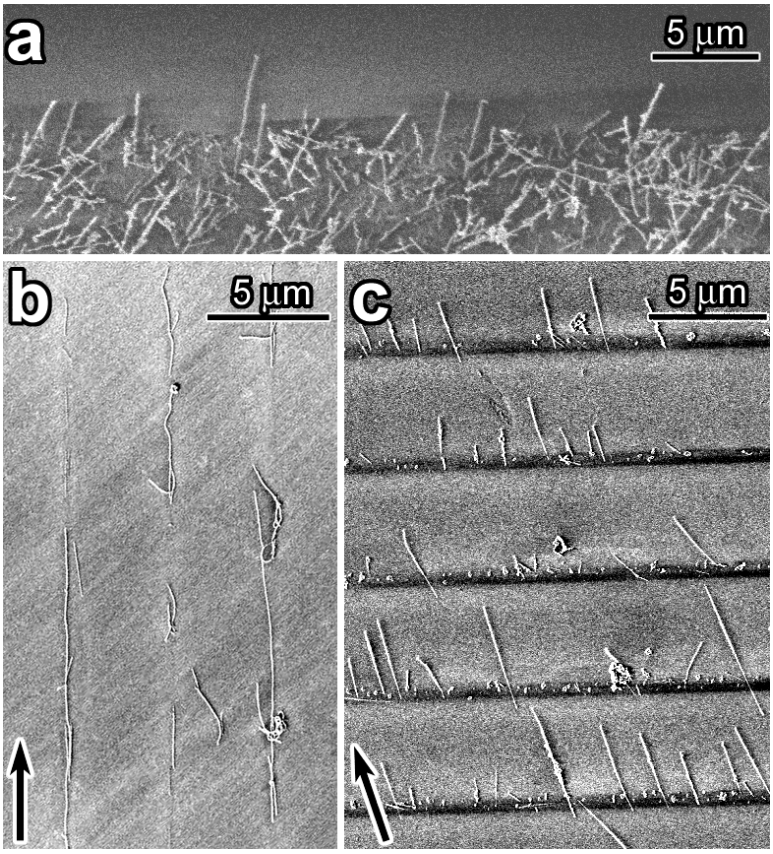

Figure 6.4: Controlled deposition of nanotubes. (a) The edge of an unaligned mat of MWCNTs deposited on an area activated by the electron beam. The edge of the beam-activated area runs horizontally through the center of the image. (b) SWCNTs placed by fluidic alignment onto beam activated lines which were oriented parallel to the direction of fluid flow. (c) MWCNTs placed by fluidic alignment $\sim 70^\circ$ to beam-activated lines. The arrows indicate the direction of flow.

edge of a patterned area onto which nanotubes have been randomly deposited with no alignment. The preferential deposition of nanotubes on the selected area (lower half of the figure) is easily apparent. By controlling the raster of the electron beam, we are able to create any desired adhesion pattern on the substrate, with the untreated residual coating inhibiting deposition elsewhere. By combining targeted adhesion and fluidic alignment, deposition of nanotubes in an ordered fashion becomes feasible. Figure 6.4 (b) shows single walled carbon nanotubes (SWCNTs) which have been deposited from a solution flowing

parallel to patterned lines of activated substrate, while Figure 6.4 (c) is an example of MWCNTs deposited from a solution flowing ∼70° to patterned lines of activated substrate; here we observe that the trailing edge of the nanotubes adheres to the targeted region. If the activated regions are dots rather than lines, then a targeted array is possible, as is the case for the two-dimensional MWCNT array underlying the devices of Figure 6.2. By changing the size and spacing of the dots we are able to control the average number of MWCNTs adhering to each dot. If non-purified nanotubes are used in the alignment and targeted deposition process, carbon onions and other byproducts of the arc discharge process adhere to the beam activated areas as well.

Characterization of selective deposition

To determine the source of selective deposition following electron beam activation, we have tested other surface coatings. Coatings of poly(methyl methacrylate) (PMMA) in anisole (2% PMMA) and in chlorobenzene (3.5% PMMA) produce similar results. Substrates with no polymer present (pristine wafers, or those which had been plasma cleaned or soaked for 12 hours in acetone) show no evidence of selective adhesion following beam exposure.

Polymer chains in PMMA experience several structural transitions when exposed to increasing doses of electron irradiation. At the low doses normally used in electron beam lithography, the polymer chains undergo scission, allowing for their selective removal by an appropriate developer. At higher doses, nearby chains become cross-linked. For an acceleration voltage of 15 keV, cross-linking prevails over scission at doses of approximately 1500 μC/cm^2 [104]. As the dosage is further increased, a highly cross-linked network is

formed ($\sim$ 10000 μC/cm^2 at 15keV) [104]. We find that the minimum dose for selective nanotube adhesion is 5000 μC/cm^2, with an optimal dose of 50,000 μC/cm^2.

Our measured doses, however, are only effective at low acceleration voltages ($\sim$1 keV), and correspond to much higher doses at 15 keV. Due to their higher interaction cross-section, low energy electrons have a higher stopping power than high energy electrons (stopping power is the rate at which electrons transfer energy to the material they are traveling through and has been studied extensively for many materials [105]). For carbon, the stopping power of 1 keV electrons is roughly seven times greater than that of 15 keV electrons [106]. Our minimum dose of 5000 μC/cm^2 at 1 keV is therefore far in excess of the equivalent cross-linking threshold dose discussed above, which suggests modification of the PMMA beyond simple cross-linking. PMMA has also been shown to graphitize when subjected to large doses of ion beam irradiation [107]. The lack of adhesion to cross-linked networks and the large effective doses being delivered are highly suggestive that the graphitization threshold has been reached. To our knowledge this is the first time this effect has been demonstrated with electron beam irradiation.

Targeted deposition is selective to the solvent used in the nanotube suspension. The effect is not observed for a majority of common solvents and solutions (dichloroethane, isopropanol, acetone, ethyl lactate, and 1% sodium dodecyl sulfate in water). Of the solvents tested, only ODCB (and to a lesser extent, methoxybenzene) resulted in effective targeted deposition. Ultrasonication of SWCNT in ODCB has been shown to create a sonopolymer which coats the surface of the nanotubes [108]. Although our method requires less ultrasonication than was reported to cause significant coating by the sonopolymer, inspection of similarly dispersed MWCNTs by TEM has shown that while the nanotubes are still mostly

pristine, there are isolated sections covered with a thin amorphous coating. We suggest that polymerized solvent adhering to the nanotubes increases their interaction with the beam activated substrate – in effect, the nanotubes must be activated along with the substrate.

6.3.4 Array fabrication

Once arrays of MWCNTs or similar structures have been deposited, further processing and device fabrication can be relatively straightforward. In our torsional actuator demonstration array, the nanotubes are first placed in an array configuration on a degenerately doped silicon wafer with 1 μm of thermally grown oxide on its top surface. The paddle and anchors are then patterned by electron beam lithography and deposited by electron beam evaporation of gold. To suspend the devices, approximately 500 nm of the silicon oxide is selectively removed with a buffered hydrofluoric acid etch. In the prototype array shown in Figure 6.2, each row of actuators is connected together to simplify the wiring arrangement and still allow for semi-independent actuation. The actuators could be made completely independent by using a more complicated wiring scheme, perhaps incorporating multiple conducting layers to avoid shorting the leads from one device to another. Multilayer processing would also allow for higher density packing of devices.

Torsional actuator arrays operating at radio frequencies might find use in optical switching or in adaptive optics applications. With each actuator serving as a high frequency mechanical filter, such an array could also be used for parallel signal processing in telecommunications. Furthermore, by tracking the frequency shift of each actuator, an array of individually functionalized actuators could be used as mass sensors for simultaneous environmental monitoring of a variety of substances.

6.4 Conclusions

In summary, we have fabricated arrays of torsional actuators using a novel nanotube positioning technique. The nanotubes are oriented by fluid flow across a spinning substrate and adhere preferentially to regions that have been activated by a focused electron beam. The adhesion is found to be due to extreme modification of a residual polymer layer already present in lithographic work. By varying the flow direction and electron beam exposure we are able to deposit nanotubes in a variety of patterns that can then be contacted by standard lithography.

Our ability to orient and preferentially place molecular structures paves the way for their integration into mass produced devices. Aside from the torsional actuator array already described, an immediate, simple application is the use of nanotubes as electrical interconnects between units of an integrated circuit (especially desirable due to their ability to carry extremely high electrical and thermal current densities). The unique physical properties of carbon nanotubes could be harnessed in other applications as well, such as high density arrays of field effect transistors, gas sensors or biosensors. Alternate geometrical configurations, including radially aligned nanotubes, crossed nanotubes, etc. could be easily fabricated using the techniques described here.

Chapter 7

Manipulation of individual nanotubes

7.1 Introduction

The methods described in the previous chapter are highly effective for placing multiple nanotubes in any desired position or orientation on a planar substrate. There remain certain cases, however, in which it is necessary to place or attach a nanotube onto a three dimensional object where fluid flow cannot be used. To enable this kind of manipulation, I have designed and assembled a piezo-based three-axis nanomanipulator, described in detail in Appendix B. The nanomanipulator can be used *in situ* in a scanning electron microscope (SEM), providing real time video feedback as individual nanotubes are picked up and moved around. In the sections below I describe several applications of this system, including the fabrication of probes for both atomic force microscopy (AFM) and scanning tunneling microscopy (STM), as well as the deposition of nanotubes onto prefabricated test

structures.

7.2 Atomic force microscopy probes

The high aspect ratio and stiffness of carbon nanotubes make them ideal for use in scanning probe microscopy, especially as probes for AFM. Several methods have been used to fix nanotubes to the end of an AFM tip, including gluing [62], growth via chemical vapor deposition [109], and, recently, by dielectrophoresis [110]. In addition, electron beam deposition has been used to obtain a stronger attachment of the nanotubes to the AFM tip [111, 112].

High spatial resolution for AFM imaging requires not only a strong bond between nanotube and probe but also precise control of the length of the nanotube [113, 114, 115]. Long nanotube tips are suitable for imaging deep holes but are more likely to bend, while short nanotubes are, in general, more useful for imaging flat samples. Thus, there is a trade off between horizontal resolution and the ability to probe tight corners, with the ideal length of the nanotube tip dependent upon the roughness of the sample in question.

Here we report on the successful positioning of an individual multiwalled carbon nanotube onto the end of an AFM tip. We retrieve a single nanotube from the edge of a razor blade onto which nanotubes had been deposited using an AFM tip mounted on a nanomanipulator inside an SEM [116]. The nanotube can be cut down to any length using the cutting process described in Chapter 4. We demonstrate the performance of these tips by imaging DNA molecules in air with amplitude modulation mode AFM.

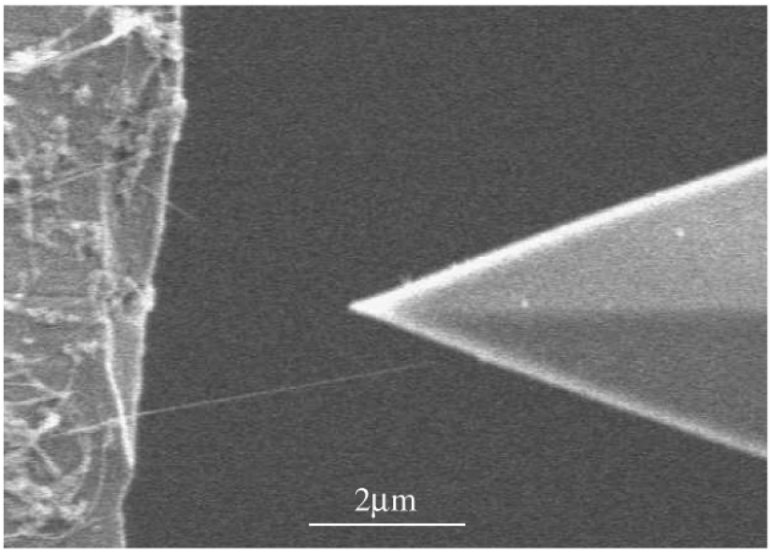

Figure 7.1: SEM micrograph of an AFM tip next to a nanotube-coated razor blade.

7.2.1 Fabrication of nanotube-tipped probes

The multiwalled carbon nanotubes used here are prepared by the standard arc-discharge technique [3]. After purification, a 10 μl ethanol suspension of nanotubes is deposited between two razor blades placed on a clean glass microscope slide, separated by a 400 μm gap. The carbon nanotubes are aligned on the edges of the razor blades by a 70 V, 1 kHz AC signal applied across the gap [117]. A nanotube-coated razor blade is then mounted inside the SEM opposite a commercially purchased AFM tip/cantilever, which is mounted on the nanomanipulator and can be translated through all three axes.

The AFM tip is then moved into the vicinity of any desired carbon nanotube protruding from the edge of the razor blade, as seen in Figure 7.1. This method allows us to select the diameter (10 – 30 nm) of the nanotube to be mounted. The AFM tip is then brought underneath the nanotube and slowly raised until the nanotube contacts the top surface of the tip.

Contact between the nanotube and the AFM tip is easily observed by the abrupt

change in shape of the nanotube as it bends and adheres to the tip through van der Waals forces. This adhesion is fairly weak, however, and can be broken simply by moving the AFM tip away. To improve the adhesion, the nanotube is welded to the tip surface through electron beam deposition [118]. In this process, the SEM electron beam is focused onto the junction between tip and nanotube. Often, the dissociation of organic species already present in the SEM chamber causes enough deposition of amorphous carbon onto the junction [119, 120] to mechanically pin the nanotube to the AFM tip surface. To obtain a stronger bond, however, a platinum-hydrocarbon gas may be bled into the chamber via a commercially available Gas Injection System (GIS). Upon striking the gas molecules, the electron beam disassociates them and deposits an amorphous platinum-carbon material onto the junction, creating a strong mechanical bond. To verify that enough material has been deposited, the AFM nanotube tip is slowly displaced laterally to verify its attachment. Once the nanotube is fixed, small displacements of the AFM tip allow us to align the nanotube and to straighten it with respect to the AFM silicon tip axis.

The electron beam is then used to cut the nanotube tip to any desired length, using the process as described in detail in Chapter 4. The software capabilities of the SEM are used to initiate a perpendicular raster of the electron beam at the desired distance away from the AFM silicon tip apex. The beam can be used to cut all the way through the nanotube. However, if the cutting process is interrupted before completion, the nanotube can be severed simply by pulling on it, as shown in Figure 7.2.

This method provides reliable and reproducible AFM nanotube tips with a precision in length of about 2 nm. More than 40 nanotube tips of lengths varying from 50 nm to 4 μm have been fabricated. Several of them can be seen in Figure 7.3. Multiwalled carbon

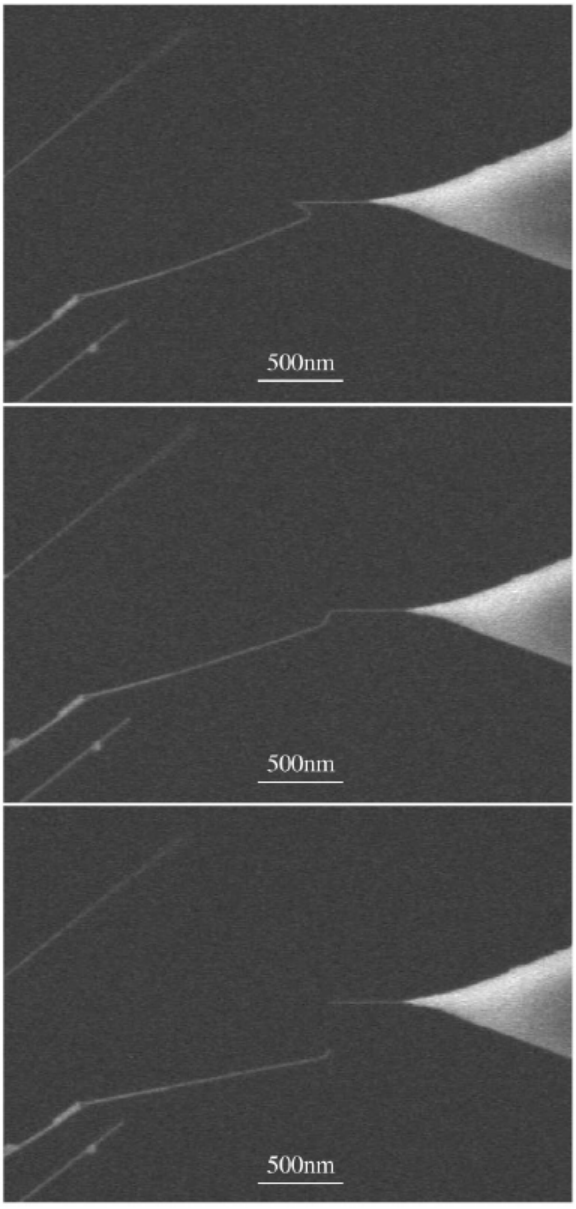

Figure 7.2: SEM micrographs of a partially cut carbon nanotube severed by tensile stress.

nanotubes (instead of single-walled carbon nanotubes) have been used because they are less flexible and create less thermal vibration for a given length.

7.2.2 Characterization of nanotube-tipped AFM probes

The nanotube-tipped AFM probes were mounted on a Nanoscope III AFM to characterize their imaging properties. Double-stranded DNA on mica was imaged in amplitude modulation (tapping) mode. We used a set point amplitude oscillation of 7 nm and a free amplitude of 12 nm. The engaging process was stopped when the force analysis started to show an interaction between the tip and the sample. CNT tips produce sharper images of DNA molecules ($\sim 6 \pm 0.8$ nm in width) than regular silicon tips ($\sim 10 \pm 1$ nm in width). However, the quality of the image appears to depend upon the CNT length. Long CNT tips (≥ 100 nm) produce less sharp images (apparent width of DNA $\sim 8 \pm 1$ nm) and tend to cause double-tip artifacts, as shown in Figure 7.4 (a). These may be due to bending and oscillation of the nanotube tip during the tapping process. Shorter CNT tips generate the sharpest DNA images (apparent widths of ~ 6 nm $\pm$ 0.8 nm), as shown in Figure 7.4 (b).

7.3 Scanning tunneling microscopy probes

Using a similar process, we have also fabricated scanning tunneling microscopy (STM) probes tipped with multiwalled carbon nanotubes. Since STM probes are much easier to manipulate than AFM probes (they are essentially thin tungsten wires, etched on one end to make them very sharp), we are able to load them into other systems, including transmission electron microscopes, where we can characterize and process them further. Figure 7.5 shows a TEM image of the end of one such probe which has been subjected

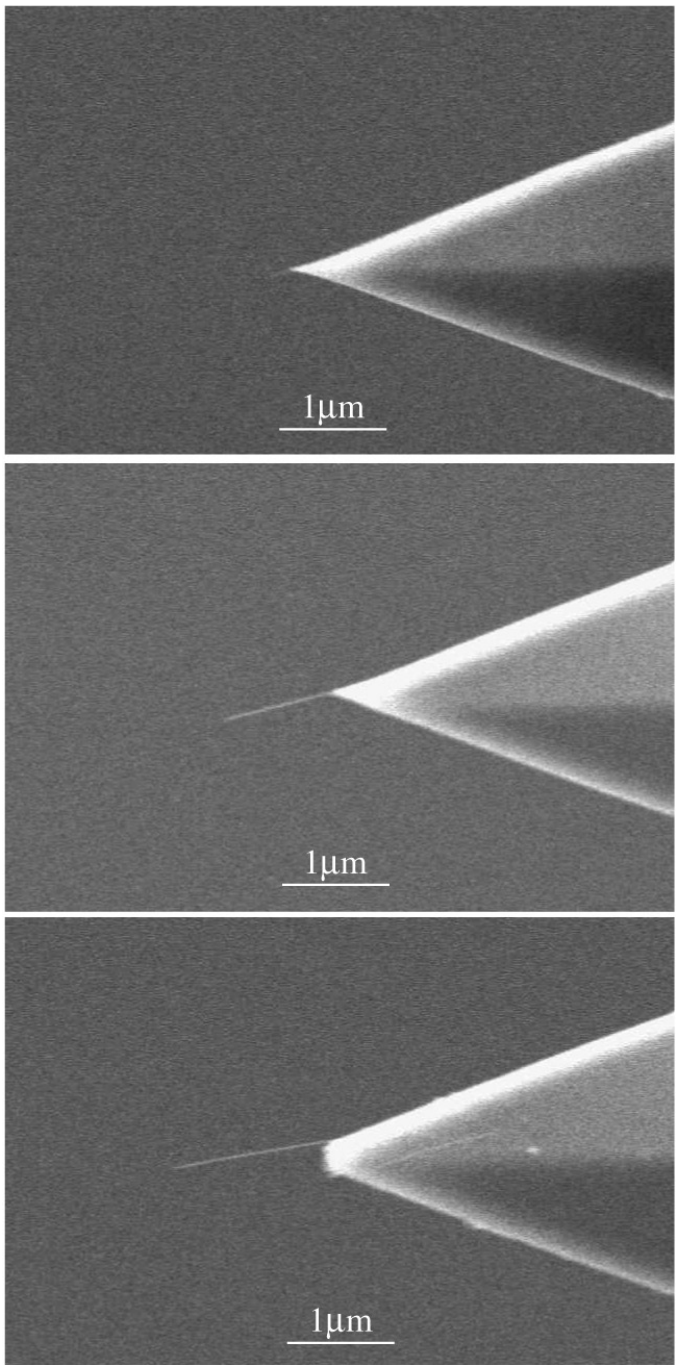

Figure 7.3: Nanotube-tipped AFM tips of varying length (0.1, 1.0, 1.5 μm) fabricated using the nanomanipulator and SEM gas injection system. The nanotubes were cut to length using the low energy electron beam cutting process.

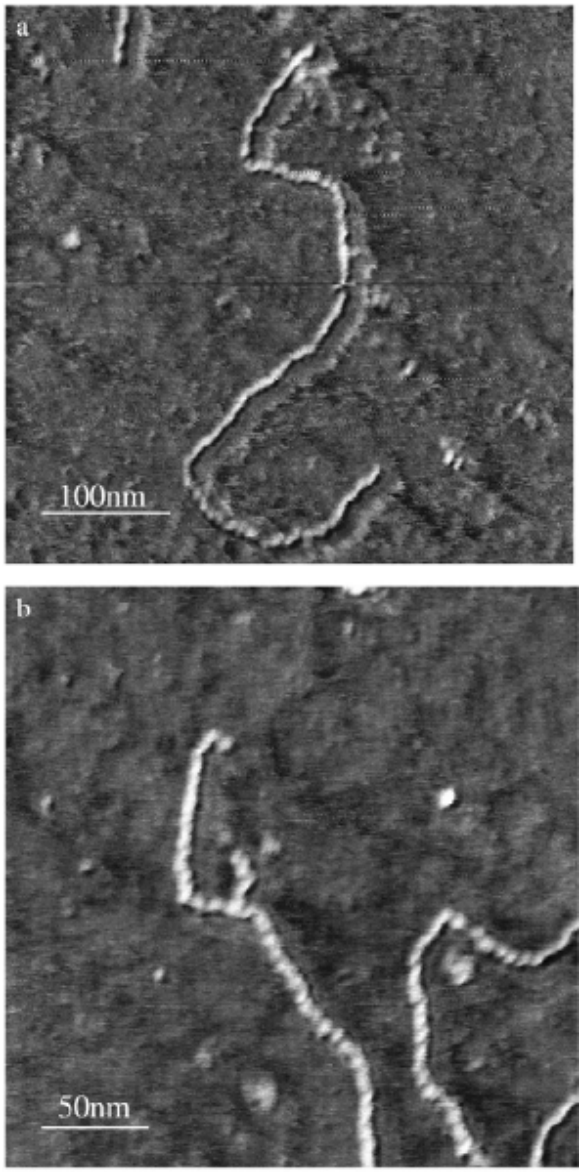

Figure 7.4: Nanotube-tipped AFM images of double-stranded DNA on mica imaged in air. The images were acquired with nanotube tips of length (a) 300 nm and (b) 50 nm.

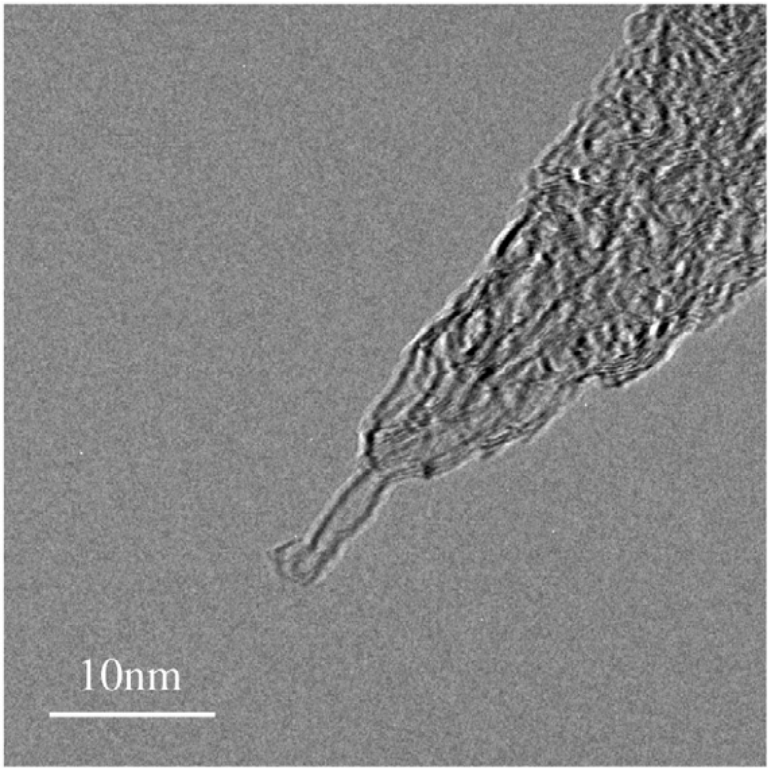

Figure 7.5: TEM micrograph of a nanotube-tipped STM probe fabricated using the nanomanipulator and SEM gas injection system (GIS). The nanotube has been subjected to a post-fabrication current treatment *in situ* in the TEM which has reformed it into a sharper tip.

to a post-fabrication current treatment. By passing large amounts of current through the nanotube (while it is in contact with another electrode inside of the TEM), we are able to reform the end into a significantly sharper feature.

7.4 Manipulation and integration of individual nanotubes into prefabricated devices

Due to their versatility, STM probes can be used to transfer nanotubes from one sample to another, or to place nanotubes in precise positions on prefabricated test structures. In this case, the nanotube is attached to an STM probe with a minimally thin

layer of amorphous platinum-carbon composite (as described in Section 7.2.1) so that it can later be released. The nanotube-tipped STM probe is then maneuvered into position such that the free end of the nanotube touches the object onto which it is to be deposited. This free end is then welded to the object with a larger amount of platinum-carbon composite. Then the STM probe is moved such that the nanotube attains its desired position. Finally, the probe is either sharply retracted, releasing the nanotube from the probe, or another welding step is taken to assure that the nanotube will be fixed on both ends to its new location.

This technique has been used to place both carbon and boron nitride nanotubes on prefabricated test fixtures to measure their thermal conductance properties [121]. Figure 7.6 shows a boron nitride nanotube spanning one such device. The deposited nanotube can be bent and reshaped by nudging it with the nanomanipulator, enabling measurements of the geometric dependence of thermal conductance.

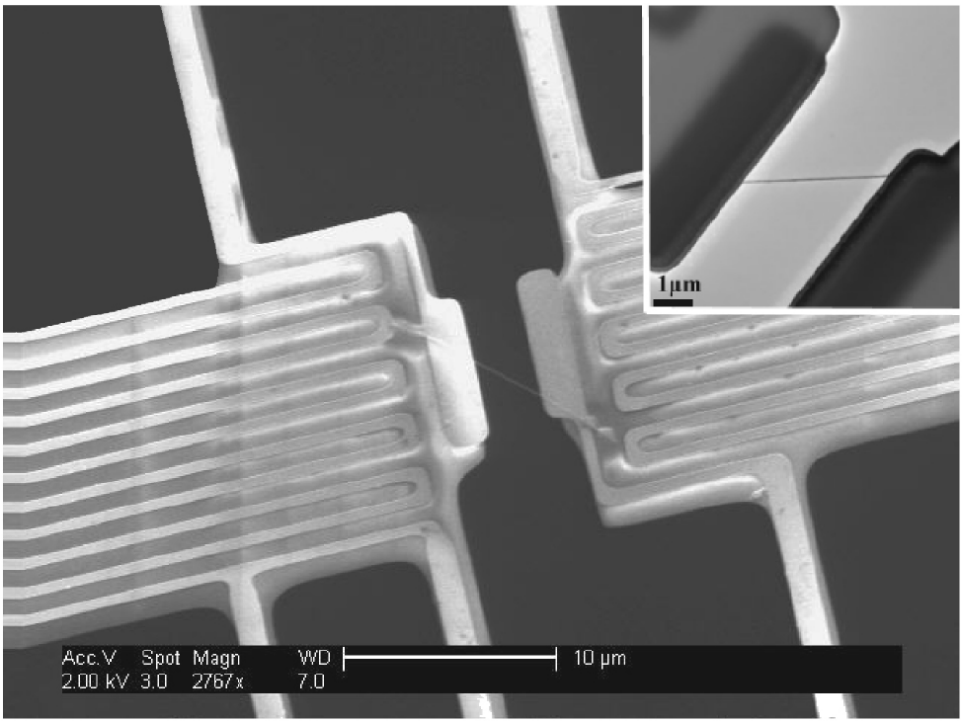

Figure 7.6: SEM micrograph of a microfabricated thermal test fixture onto which a nanotube has been deposited. The scale bar is 10 μm. The inset shows the corresponding transmission electron microscope image of the same device (the scale bar is 1 μm). Adapted from [121].

Bibliography

[1] S. Iijima, Nature **354**, 56 (1991).

[2] L. X. Zheng et al., Nature Materials **3**, 673 (2004).

[3] T. W. Ebbesen and P. M. Ajayan, Nature **358**, 220 (1992).

[4] T. Guo et al., Journal of Physical Chemistry **99**, 10694 (1995).

[5] R. Saito, G. Dresselhaus, and M. S. Dresselhaus, *Physical Properties of Carbon Nanotubes*, World Scientific Publishing Company, 1998.

[6] E. T. Thostenson, Z. F. Ren, and T. W. Chou, Composites Science and Technology **61**, 1899 (2001).

[7] B. C. Edwards, Acta Astronautica **47**, 735 (2000).

[8] S. J. Papadakis et al., Physical Review Letters **93** (2004).

[9] J. Cumings and A. Zettl, Science **289**, 602 (2000).

[10] P. Tangney, S. G. Louie, and M. L. Cohen, Physical Review Letters **93**, 065503/1 (2004).

[11] P. L. McEuen and J.-Y. Park, MRS Bulletin **April**, 272 (2004).

[12] M. Gross, Chem. Br. **No. 5** (2002).

[13] C. L. Kane and E. J. Mele, Physical Review Letters **78**, 1932 LP (1997).

[14] Z. Yao, C. L. Kane, and C. Dekker, Physical Review Letters **84**, 2941 (2000).

[15] E. Pop et al., Physical Review Letters **95**, 155505 (2005).

[16] P. C. Collins, M. S. Arnold, and P. Avouris, Science **292**, 706 (2001).

[17] P. G. Collins, K. Bradley, M. Ishigami, and A. Zettl, Science **287**, 1801 (2000).

[18] S. Heinze, M. Radosavljevic, J. Tersoff, and P. Avouris, Physical Review B **68** (2003).

[19] T. Durkop, S. A. Getty, E. Cobas, and M. S. Fuhrer, Nano Letters **4**, 35 (2004).

[20] A. Y. Kasumov et al., Europhysics Letters **43**, 89 (1998).

[21] S. Frank, P. Poncharal, Z. L. Wang, and W. A. de Heer, Science **280**, 1744 (1998).

[22] A. Bachtold et al., Nature **397**, 673 (1999).

[23] P. G. Collins, M. Hersam, M. Arnold, R. Martel, and P. Avouris, Physical Review Letters **86**, 3128 (2001).

[24] P. G. Collins and P. Avouris, Applied Physics a-Materials Science & Processing **74**, 329 (2002).

[25] B. Bourlon et al., Physical Review Letters **92** (2004).

[26] B. Bourlon, C. Miko, L. Forro, D. C. Glattli, and A. Bachtold, Physical Review Letters **93** (2004).

[27] L. Langer et al., Physical Review Letters **76**, 479 (1996).

[28] H. J. Li, W. G. Lu, J. J. Li, X. D. Bai, and C. Z. Gu, Physical Review Letters **95**, 086601 (2005).

[29] S. J. Tans, A. R. M. Verschueren, and C. Dekker, Nature **393**, 49 (1998).

[30] T. Rueckes et al., Science **289**, 94 (2000).

[31] E. Nagao, H. Nishijima, S. Akita, Y. Nakayama, and J. A. Dvorak, J Electron Microsc (Tokyo) **49**, 453 (2000).

[32] A. M. Fennimore et al., Nature **424**, 408 (2003).

[33] H. B. Peng, C. W. Chang, S. Aloni, T. D. Yuzvinsky, and A. Zettl, Physical Review Letters **97**, 087203 (2006).

[34] J. A. Misewich et al., Science **300**, 783 (2003).

[35] S. B. Chikkannanavar and D. E. Luzzi, Nano Letters **5**, 151 (2005).

[36] A. Y. Kasumov, I. Khodos, P. M. Ajayan, and C. Colliex, Europhysics Letters **34**, 429 (1996).

[37] A. Kis et al., Nature Materials **3**, 153 (2004).

[38] K. Koga, T. Ikeshoji, and K. Sugawara, Physical Review Letters **92** (2004).

[39] J. Cumings, P. G. Collins, and A. Zettl, Nature **406**, 586 (2000).

[40] B. Bourlon, D. C. Glattli, C. Miko, L. Forro, and A. Bachtold, Nano Letters **4**, 709 (2004).

[41] A. M. Fennimore, T. D. Yuzvinsky, B. C. Regan, and A. Zettl, AIP Conference Proceedings **723**, 587 (2004).

[42] T. D. Yuzvinsky, A. M. Fennimore, W. Mickelson, C. Esquivias, and A. Zettl, Applied Physics Letters **86** (2005).

[43] J. Y. Huang et al., Physical Review Letters **94**, 236802 (2005).

[44] T. D. Yuzvinsky et al., Applied Physics Letters **87**, 083103 (2005).

[45] P. M. Ajayan, V. Ravikumar, and J.-C. Charlier, Physical Review Letters **81**, 1437 (1998).

[46] N. G. Chopra, F. M. Ross, and A. Zettl, Chemical Physics Letters **256**, 241 (1996).

[47] V. H. Crespi, N. G. Chopra, M. L. Cohen, A. Zettl, and S. G. Louie, Physical Review B **54**, 5927 (1996).

[48] F. Banhart, J. X. Li, and A. V. Krasheninnikov, Physical Review B **71**, 241408(R) (2005).

[49] J. Y. Huang et al., Nature **439**, 281 (2006).

[50] K. Molhave et al., Nano Letters **6**, 1663 (2006).

[51] F. Banhart, Reports on the Progess in Physics **62**, 1181 (1999).

[52] J. D. Romano and R. H. Price, American Journal of Physics **64**, 1150 (1996).

[53] V. A. Petrov, I. I. Petrova, V. Y. Chekhovskoi, and A. E. Sheindlin, High Temperatures - High Pressures **2**, 161 (1970).

[54] C. A. Klein, Reviews of Modern Physics **34**, 56 (1962).

[55] G. H. Kinchin, Proceedings of the Royal Society of London **A217**, 9 (1953).

[56] B. Larade, J. Taylor, H. Mehrez, and H. Guo, Physical Review B **64**, 075420 (2001).

[57] J. B. Neaton, K. H. Khoo, C. D. Spataru, and S. G. Louie, Computer Physics Communications **169**, 1 (2005).

[58] J. Chen et al., Annals of the New York Academy of Sciences **960**, 69 (2002).

[59] J. Chen, M. A. Reed, A. M. Rawlett, and J. M. Tour, Science **286**, 1550 (1999).

[60] J. Gaudioso, L. J. Lauhon, and W. Ho, Physical Review Letters **85**, 1918 (2000).

[61] H. W. Zandbergen et al., Nano Letters **5**, 549 (2005).

[62] H. J. Dai, J. H. Hafner, A. G. Rinzler, D. T. Colbert, and R. E. Smalley, Nature **384**, 147 (1996).

[63] S. C. Tsang, Y. K. Chen, P. J. F. Harris, and M. L. H. Green, Nature **372**, 159 (1994).

[64] J. X. Li and F. Banhart, Nano Letters **4**, 1143 (2004).

[65] A. Rubio, S. P. Apell, L. C. Venema, and C. Dekker, European Physical Journal B **17**, 301 (2000).

[66] J. Y. Park, Y. Yaish, M. Brink, S. Rosenblatt, and P. L. McEuen, Applied Physics Letters **80**, 4446 (2002).

[67] J. Goldstein, *Scanning electron microscopy and X-ray microanalysis : a text for biologists, materials scientists, and geologists*, Plenum Press, New York, 2nd edition, 1992.

[68] H. G. Heide, Laboratory Investigation **14**, 1134 (1965).

[69] D. Joy, C. Joy, and D. Armstrong, in *Electron probe microanalysis : applications in biology and medicine*, edited by K. Zierold and H. K. Hagler, pages 127–136, Springer-Verlag, Berlin ; New York, 1989.

[70] Y. Talmon, H. T. Davis, L. E. Scriven, and E. L. Thomas, Journal of Microscopy-Oxford **117**, 321 (1979).

[71] B. W. Smith and D. E. Luzzi, Journal of Applied Physics **90**, 3509 (2001).

[72] J. Marti and M. C. Gordillo, Journal of Chemical Physics **119**, 12540 (2003).

[73] F. Banhart, T. Fuller, P. Redlich, and P. M. Ajayan, Chemical Physics Letters **269**, 349 (1997).

[74] J. Schutten, F. J. Deheer, H. R. Moustafa, A. J. Boerboom, and Kistemak.J, Journal of Chemical Physics **44**, 3924 (1966).

[75] J. W. Judy, Smart Materials & Structures **10**, 1115 (2001).

[76] L. S. Fan, Y. C. Tai, and R. S. Muller, Sensors and Actuators **20**, 41 (1989).

[77] H. G. Craighead, Science **290**, 1532 (2000).

[78] M. L. Roukes, in *Tech. Digest of the 2000 Solid-State Sensor and Actuator Workshop*, edited by L. Bousse and M. Schmidt, pages 367–376, Transducer Research Foundation, Cleveland, 2000.

[79] D. W. Carr, S. Evoy, L. Sekaric, H. G. Craighead, and J. M. Parpia, Applied Physics Letters **75**, 920 (1999).

[80] R. Lifshitz and M. L. Roukes, Phys. Rev. B **61**, 5600 (2000).

[81] J. C. Charlier and J. P. Michenaud, Physical Review Letters **70**, 1858 (1993).

[82] A. N. Kolmogorov and V. H. Crespi, Physical Review Letters **85**, 4727 (2000).

[83] S. J. Tans et al., Nature **386**, 474 (1997).

[84] M. Bockrath et al., Science **275**, 1922 (1997).

[85] B. I. Yakobson, C. J. Brabec, and J. Bernholc, Phys. Rev. Lett. **76**, 2411 (1996).

[86] P. A. Williams et al., Physical Review Letters **89** (2002).

[87] P. A. Williams et al., Applied Physics Letters **82**, 805 (2003).

[88] M. F. Yu, B. I. Yakobson, and R. S. Ruoff, Journal of Physical Chemistry B **104**, 8764 (2000).

[89] P. Poncharal, Z. L. Wang, D. Ugarte, and W. A. de Heer, Science **283**, 1513 (1999).

[90] R. Saito, R. Matsuo, T. Kimura, G. Dresselhaus, and M. S. Dresselhaus, Chemical Physics Letters **348**, 187 (2001).

[91] Y. E. Lozovik, A. Minogin, and A. M. Popov, Physics Letters A **313**, 112 (2003).

[92] J. I. Paredes, A. Martinez-Alonso, and J. M. D. Tascon, Carbon **38**, 1183 (2000).

[93] Y. C. Tseng et al., Nano Letters **4**, 123 (2004).

[94] J.-P. Salvetat et al., Applied Physics A **69**, 255 (1999).

[95] Y. Huang, X. F. Duan, Q. Q. Wei, and C. M. Lieber, Science **291**, 630 (2001).

[96] H. J. Xin and A. T. Woolley, Nano Letters **4**, 1481 (2004).

[97] M. D. Lay, J. P. Novak, and E. S. Snow, Nano Letters **4**, 603 (2004).

[98] J. Hedberg, L. Dong, and J. Jiao, Applied Physics Letters **86**, 143111 (2005).

[99] M. Burghard, G. Duesberg, G. Philipp, J. Muster, and S. Roth, Advanced Materials **10**, 584 (1998).

[100] J. Liu et al., Chemical Physics Letters **303**, 125 (1999).

[101] S. G. Rao, L. Huang, W. Setyawan, and S. H. Hong, Nature **425**, 36 (2003).

[102] K. Yamamoto, S. Akita, and Y. Nakayama, Journal of Physics D-Applied Physics **31**, L34 (1998).

[103] E. Valentin et al., Microelectronic Engineering **61-2**, 491 (2002).

[104] Y. Koval, Journal of Vacuum Science & Technology B **22**, 843 (2004).

[105] See, for example, the NIST stopping power and range tables available at http://phyiscs.nist.gov/PhysRefData/Star/Text/contents.html (and references contained therein) .

[106] D. C. Joy, L. Suichu, R. Gauvin, P. Hovington, and N. Evans, Scanning Microscopy **10**, 653 (1996).

[107] J. Davenas, P. Thevenard, G. Boiteux, M. Fallavier, and X. L. Lu, Nuclear Instruments & Methods in Physics Research Section B-Beam Interactions with Materials and Atoms **46**, 317 (1990).

[108] S. Niyogi et al., Journal of Physical Chemistry B **107**, 8799 (2003).

[109] C. V. Nguyen et al., Nanotechnology **12**, 363 (2001).

[110] J. Tang et al., Nano Letters **5**, 11 (2005).

[111] S. Akita et al., Applied Physics Letters **79**, 1691 (2001).

[112] P. A. Williams et al., Applied Physics Letters **80**, 2574 (2002).

[113] E. S. Snow, P. M. Campbell, and J. P. Novak, Applied Physics Letters **80**, 2002 (2002).

[114] S. Akita and Y. Nakayama, Japanese Journal of Applied Physics Part 1-Regular Papers Short Notes & Review Papers **41**, 4887 (2002).

[115] N. de Jonge, Y. Lamy, and M. Kaiser, Nano Letters **3**, 1621 (2003).

[116] H. Nishijima et al., Applied Physics Letters **74**, 4061 (1999).

[117] X. Q. Chen, T. Saito, H. Yamada, and K. Matsushige, Applied Physics Letters **78**, 3714 (2001).

[118] M. F. Yu et al., Science **287**, 637 (2000).

[119] A. Folch, J. Servat, J. Esteve, J. Tejada, and M. Seco, Journal of Vacuum Science & Technology B **14**, 2609 (1996).

[120] H. W. P. Koops, C. Schossler, A. Kaya, and M. Weber, Journal of Vacuum Science & Technology B **14**, 4105 (1996).

[121] C. W. Chang et al., Physical Review Letters **97**, 085901 (2006).

Appendix A

Acronyms and Chemical Names

AFM	Atomic Force Microscope/Microscopy
BOE	Buffered Oxide Etch
CNT	Carbon Nanotube
CVD	Chemical Vapor Deposition
DCE	Dichloroethane
DIP	Dual In-line Package
DOS	Density Of States
EBL	Electron Beam Lithography
FEA	Finite Element Analysis
GIS	Gas Injection System
HF	Hydrofluoric Acid
HOPG	Highly Ordered Pyrolytic Graphite
IPA	Isopropyl Alcohol
KOH	Potassium Hydroxide

(P)LCC	(Plastic) Leaded Chip Carrier
MAA	Methacrylic Acid
MEMS	Microelectromechanical System
MIBK	Methyl Isobutyl Ketone
MMA	Methyl Methacrylate
MWCNT	Multi-Walled Carbon Nanotube
NDR	Negative Differential Resistance
NEMS	Nanoelectromechanical System
ODCB	Orthodichlorobenzene
PMMA	Polymethylmethacrylate
RIE	Reactive Ion Etch
RPM	Revolutions per Minute
SWCNT	Single Walled Carbon Nanotube
SAM	Self-Assembled Monolayer
SEM	Scanning Electron Microscope/Microscopy
STM	Scanning Tunneling Microscope/Microscopy
TEM	Transmission Electron Microscope/Microscopy

Appendix B

Nanomanipulator

B.1 Nanomanipulator Design

In this section I describe a stick-slip piezo based nanomanipulator incorporating both commercially available elements and a custom built framework for use inside a scanning electron microscope. The piezo units were purchased from Attocube GMBH. The frame, body, and sample holder parts were machined either by me or the Physics Department Machine Shop from my designs. I also made the requisite electronic feedthroughs and a control box (with help from Cristian Esquivias) to interface with the supplied Attocube control unit. Andras Kis and Andrei Afanasiev later put together a LabVIEW interface with much needed joystick control.

B.1.1 Overview

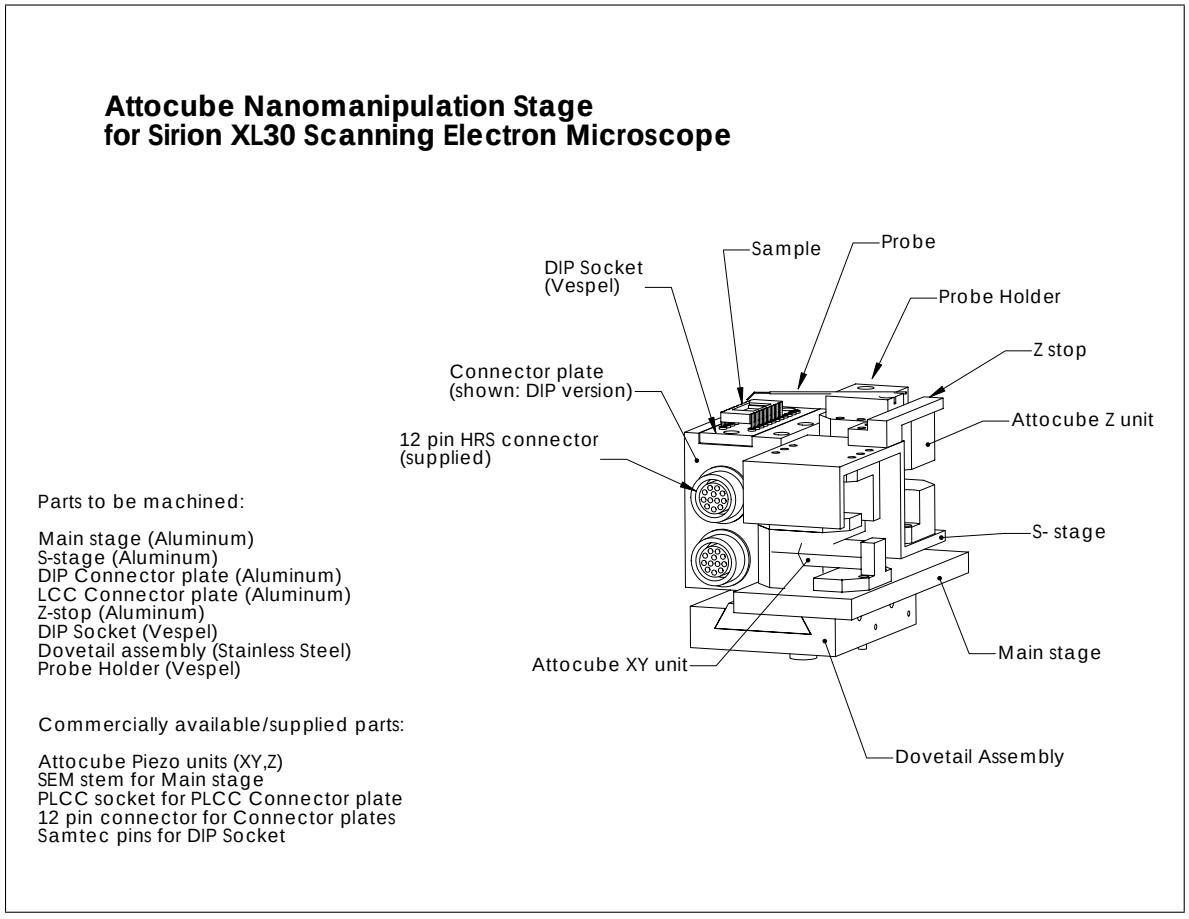

Figure B.1: An overview of the assembled nanomanipulator, with key components labeled.

B.1.2 Main stage elements

The main stage elements comprise three parts: the main body, which acts as a base for the rest of the assembly; the "S-stage," which is mounted on the Attocube XY units and supports the Attocube Z unit, and the vertical Z stop, which is mounted on the main body and prevents the Z unit from exceeding its normal range and separating into two parts.

Main body design:

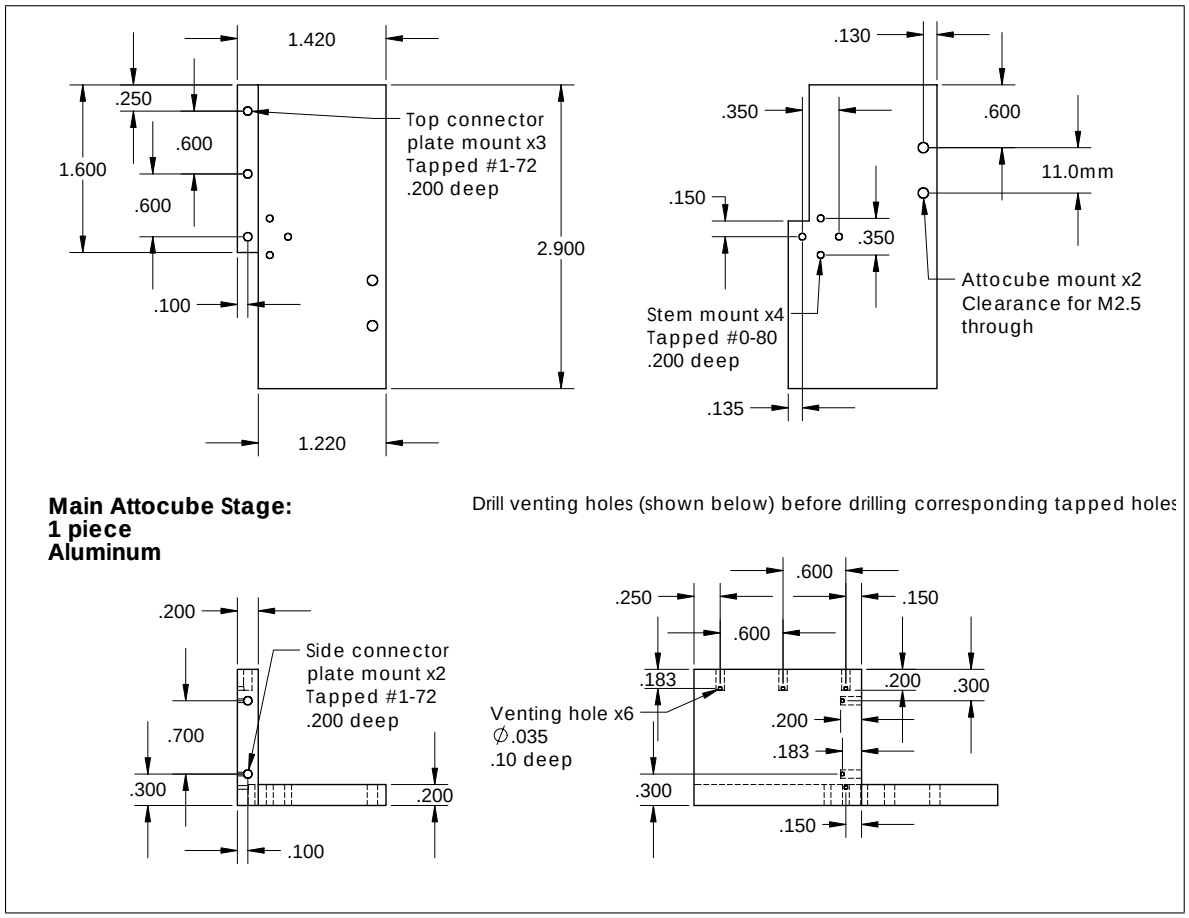

Figure B.2: Schematic drawing of the main body of the nanomanipulator stage. The main body supports both the Attocube XY piezo unit (which in turn supports the "S"-stage and Z piezo unit), which moves the probe, and the DIP or PLCC connectors, which hold the experimental sample. The main body itself is mounted on a dovetail slide for easy loading.

"S"-stage design:

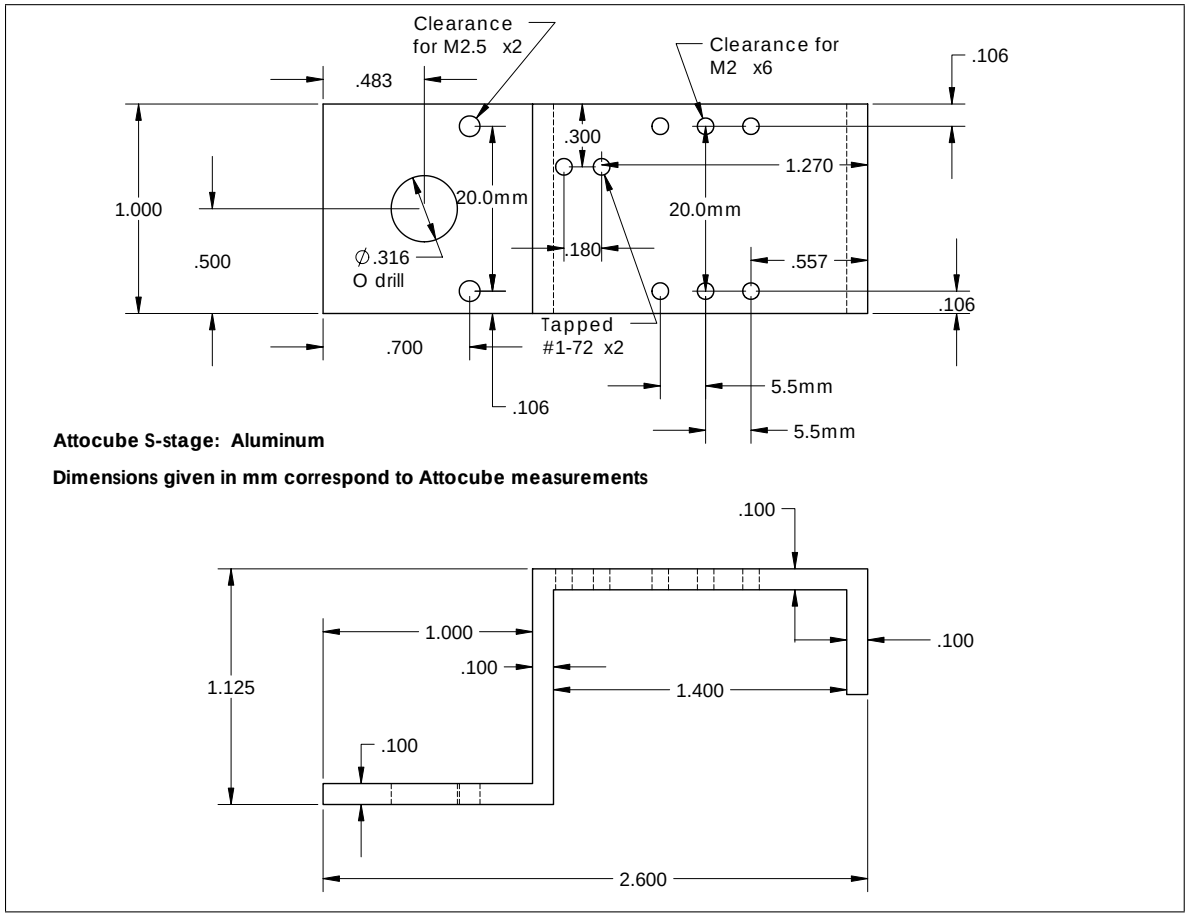

Figure B.3: Schematic drawing of the "S"-stage, which sits on top of the X and Y piezo units and supports the Z piezo unit.

“Z-stop” design:

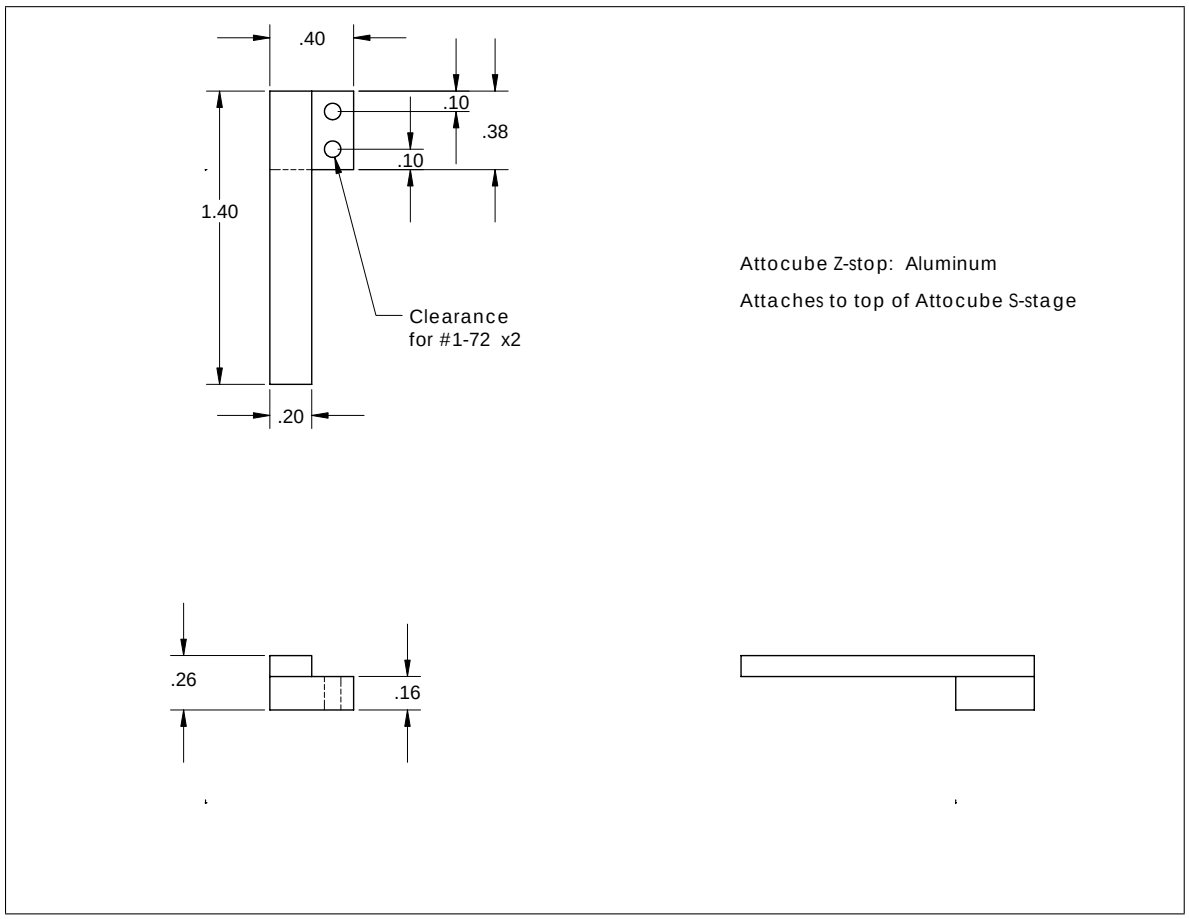

Figure B.4: Schematic drawing of the “Z-stop,” which is attached to the “S”-stage and prevents the Z piezo unit from exceeding its operational limits. If the stop is removed, the sliding section of the Z piezo unit can pop off of the top of the piezo stack and potentially cause damage.

B.1.3 Sample holders

The Nanomanipulator design is modular and different sample holders can be easily installed. The DIP socket can accept a variety of different chip carriers and prefabricated packages; the LCC socket is more limited but boasts the lowest profile of any mass produced chip carrier. To allow for the use of these samples holders without mounting the entire Nanomanipulator, a stand-alone stage was also designed.

DIP connector design:

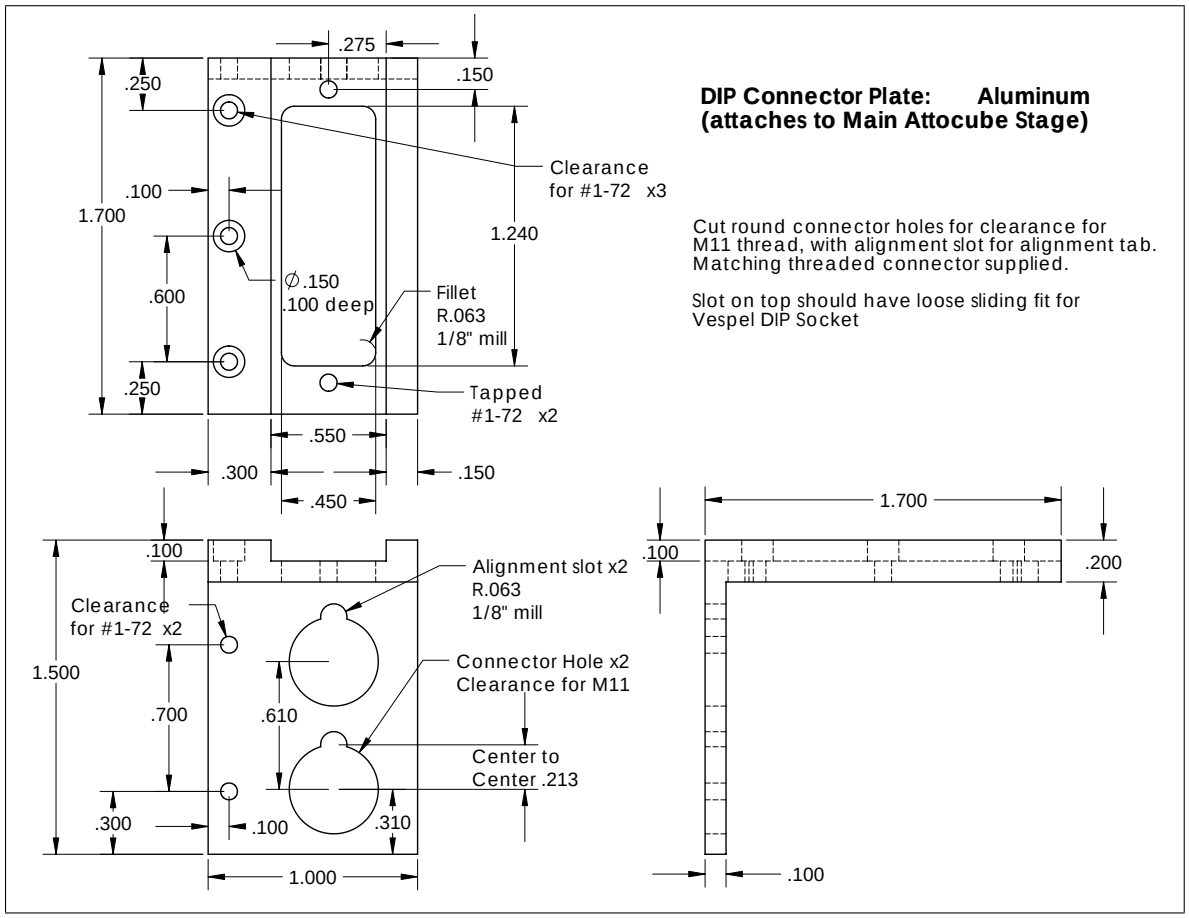

Figure B.5: Schematic drawing of the DIP (Dual In-line Package) connector. Two 12-pin cylindrical HRS connectors are inserted into the large side slots. Wires are soldered from the connectors to the pins extended down from the Vespel DIP socket.

Vespel DIP socket design:

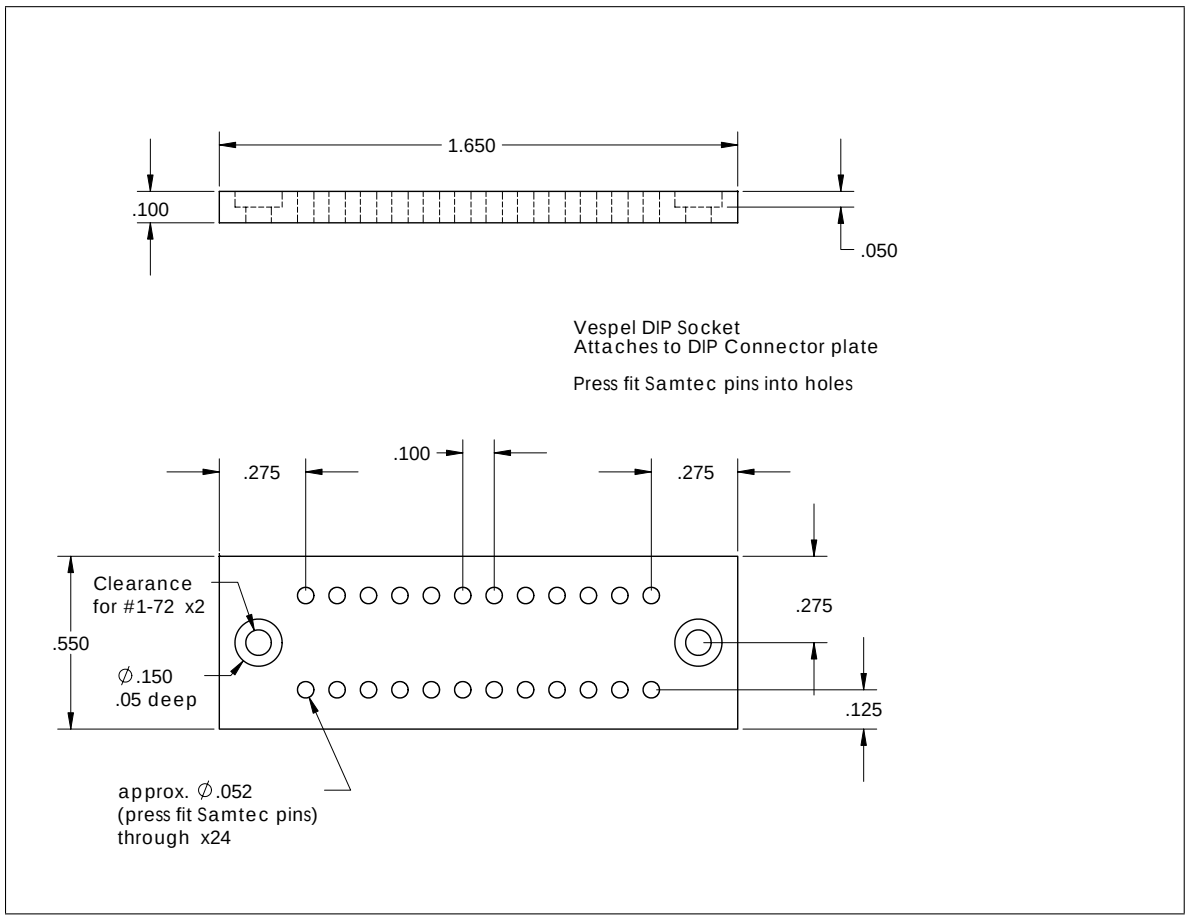

Figure B.6: Schematic drawing of the Vespel DIP socket, which is mounted in the respective slot on the DIP connector. Standard gold-plated Samtec SS sockets (removed from their plastic housings with a razor blade) are press fit into the small holes and can accept many different pin shapes and sizes.

PLCC connector design:

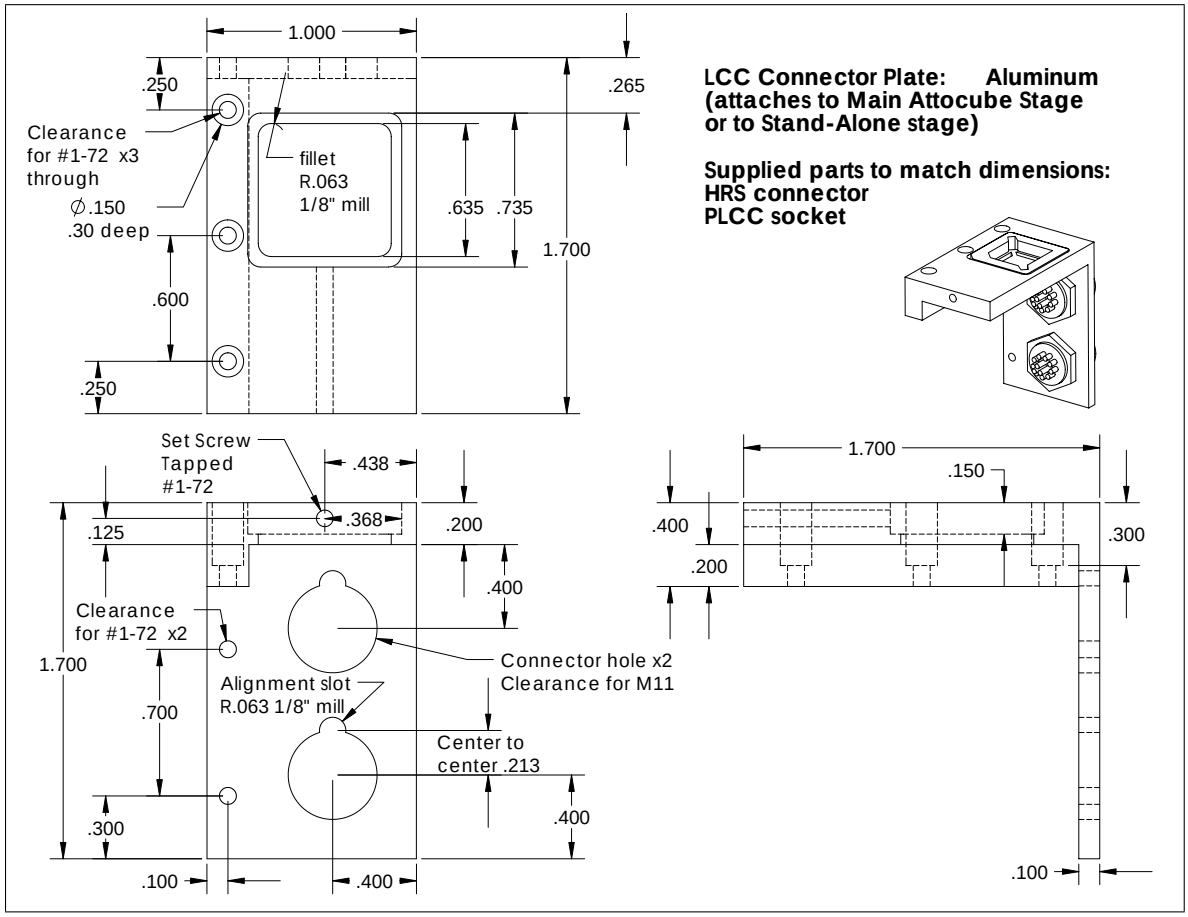

Figure B.7: Schematic drawing of the PLCC connector. A commercially available low-profile PLCC (Plastic Leaded Chip Carrier) socket is inserted into the top slot. Two 12-pin cylindrical HRS connectors are inserted into the large side slots. Wires are soldered from the connectors to the pins extended down from the PLCC socket. The PLCC connector can either be mounted on the nanomanipulator main body or on the stand-alone stage.

Stand-alone stage design:

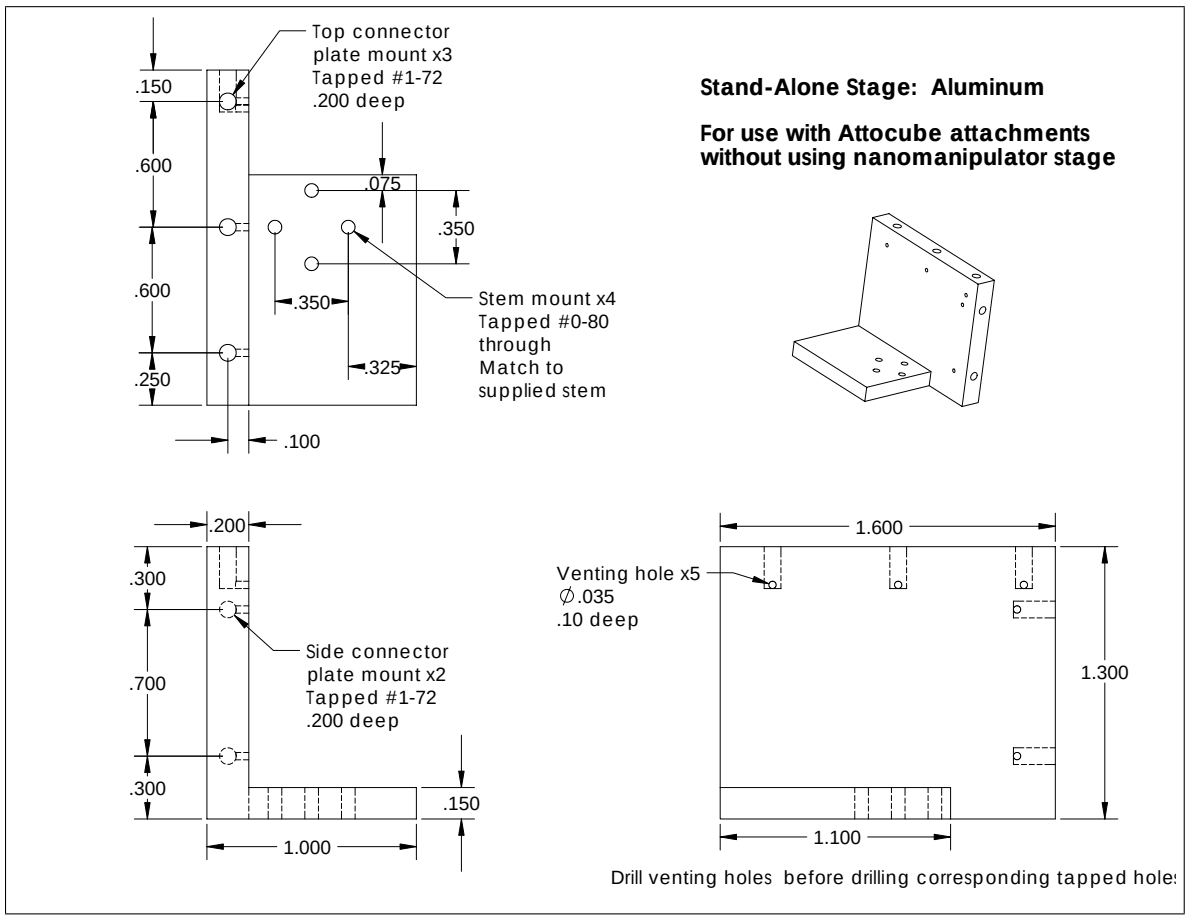

Figure B.8: Schematic drawing of the stand-alone stage, used for electronic transport measurements in the SEM when the nanomanipulator is not necessary. Either the DIP or PLCC connector can be mounted on the stand-alone stage, which itself is mounted on a dovetail slide for easy loading.

B.1.4 AFM and STM tip holders

A variety of probe holders were designed to mount AFM or STM tips in various orientations. The AFM tip holders rely upon small beryllium-copper (Be-Cu) springs (not shown in the schematics below) to gently press and hold the tips in position. STM tips are held by insertion into a thin walled tube with inner diameter slightly larger than the wire gauge used in STM tip fabrication.

Standard AFM tip holder design:

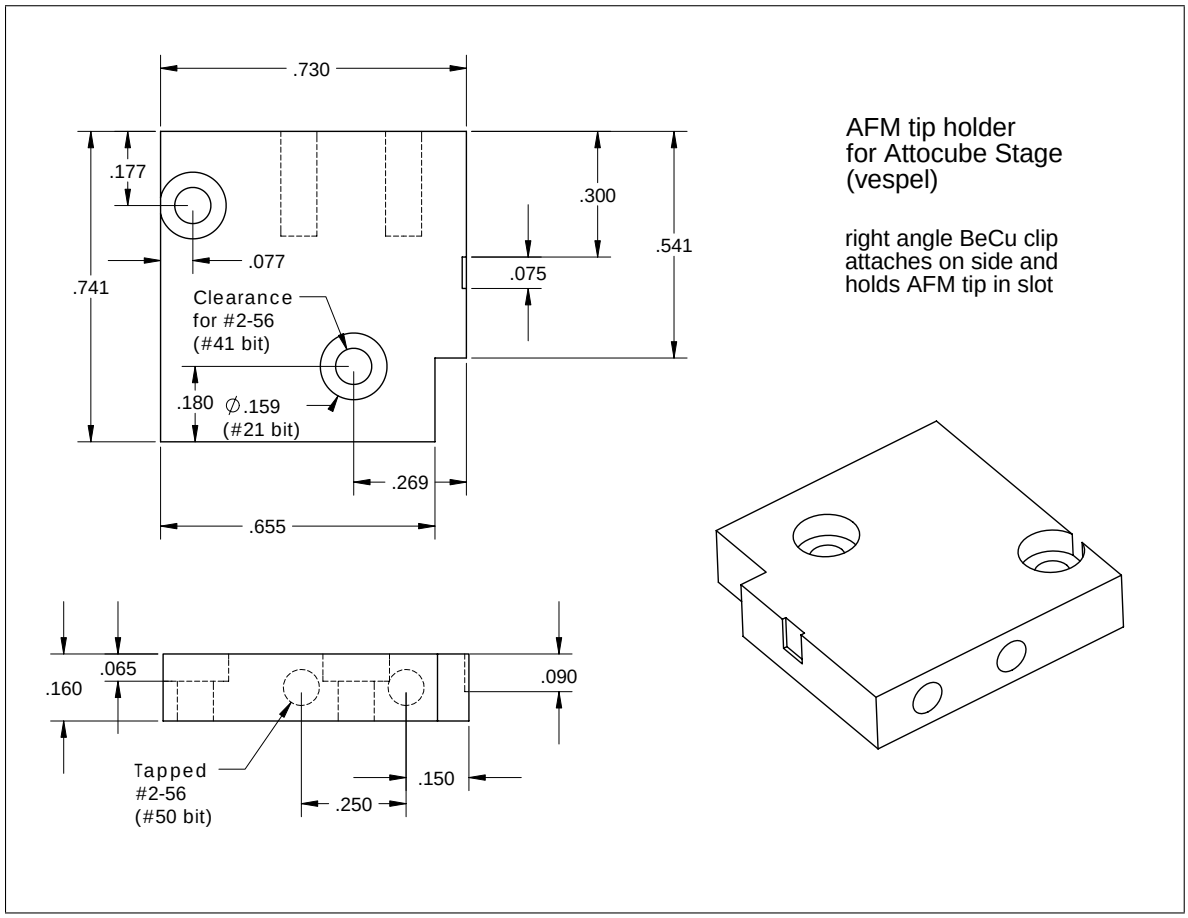

Figure B.9: Schematic drawing of the standard AFM tip holder. The tip holder is mounted on top of the Z piezo unit. A beryllium copper strip bent at 90° is screwed to the tip holder and secures the AFM tip in the shallow side slot. An inverted AFM tip holder was also designed for work in which the underside of the AFM tip must be accessible (see next page).

Inverted AFM tip holder design:

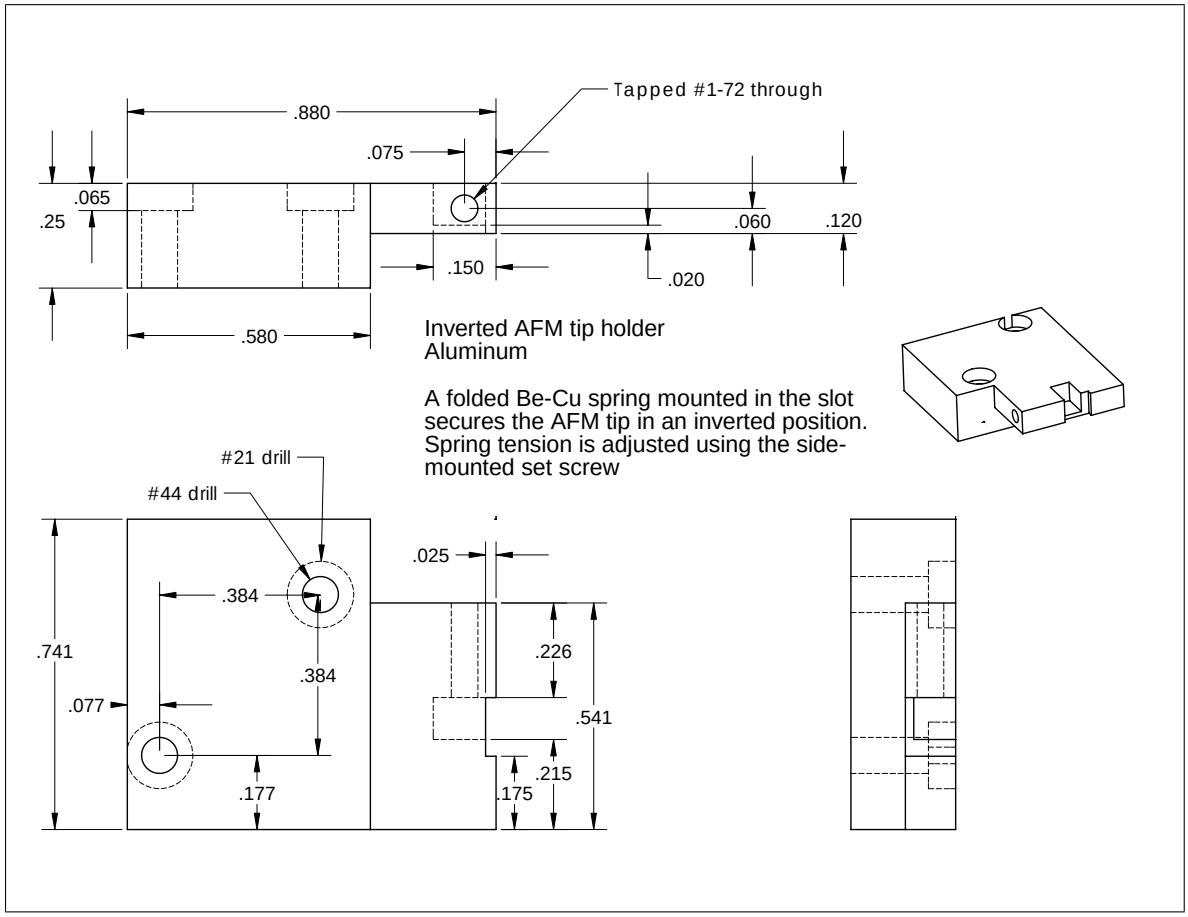

Figure B.10: Schematic drawing of the inverted AFM tip holder. The tip holder is mounted on top of the Z piezo unit. A short beryllium copper strip folded nearly in half secures the AFM tip against the wall of the shallow side slot. A standard AFM tip holder was also designed for work in which the top side of the AFM tip must be accessible (see previous page).

STM tip holder design:

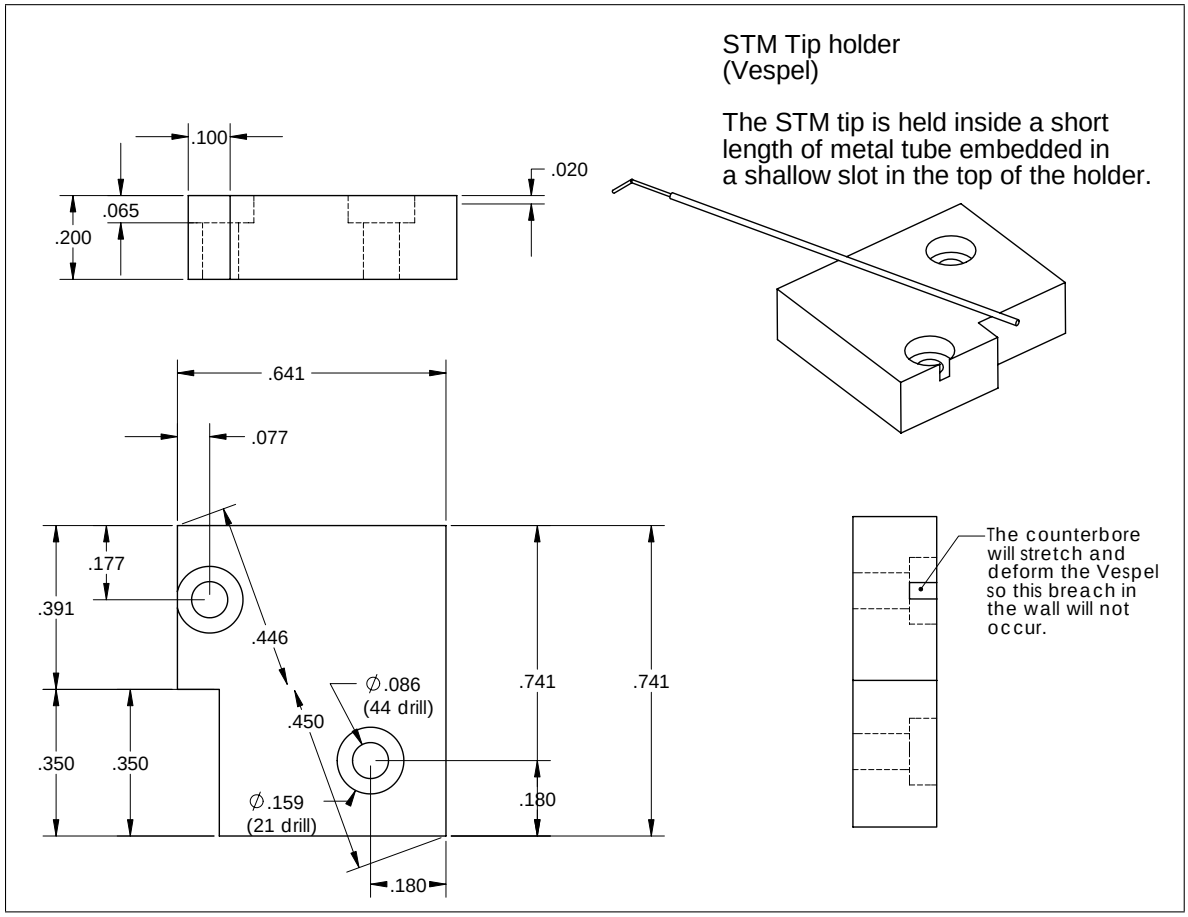

Figure B.11: Schematic drawing of the STM tip holder. STM tips are inserted into a hollow metal tube which has been press fitted into a shallow, narrow slot cut into the top of the holder. STM tips should be bent down at an angle for any manipulation work on a flat substrate.

B.1.5 Dovetail

The sample holder mounting mechanism supplied with the Sirion XL30 SEM is far from ideal: a non-standard metric threaded rod is screwed into the microscope stage body and tightened with a finger nut each time a new sample is loaded. Not only is it difficult to load a sample in a particular orientation, but there is also a high probability of seizing and thread damage due to misthreading or errant debris. To ameliorate this condition a universal dovetail system was developed and is now permanently installed in the SEM.

Dovetail overview:

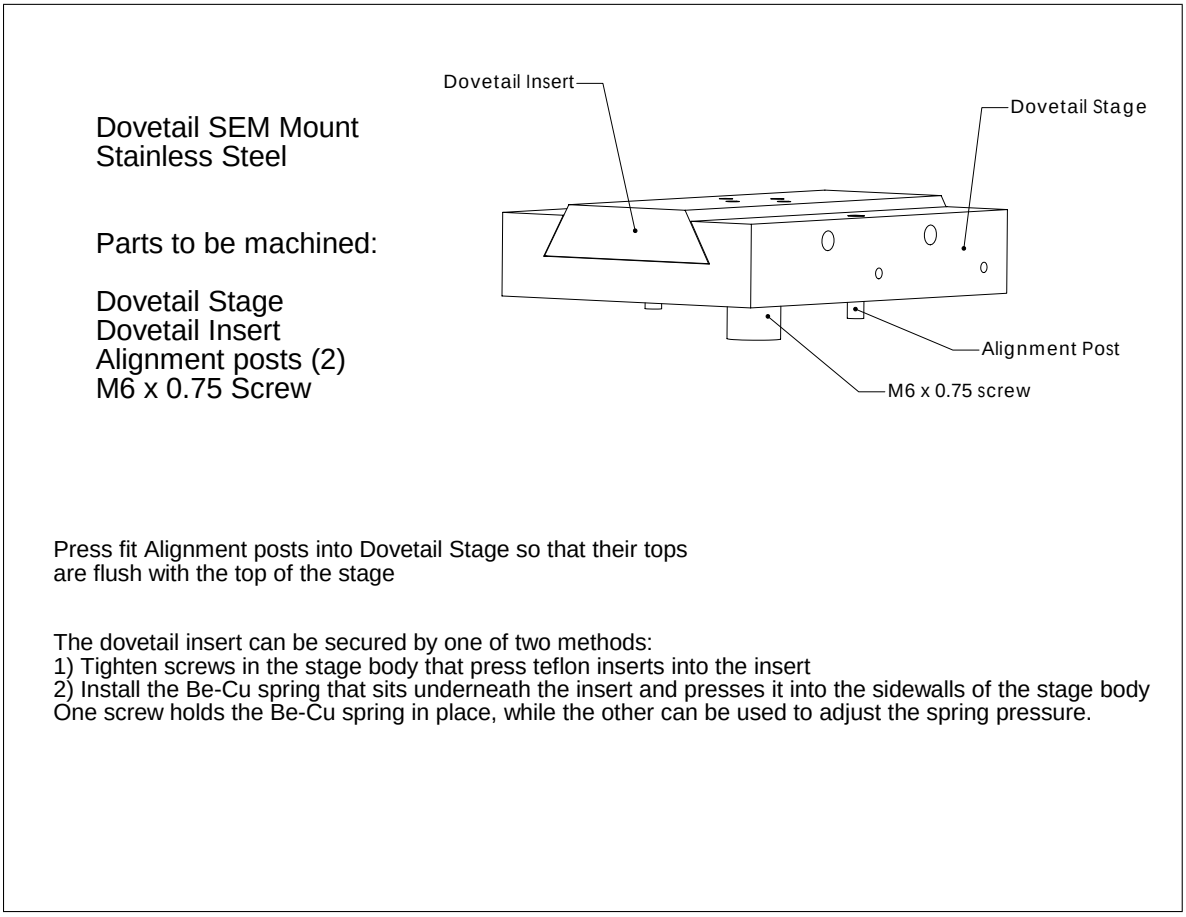

Figure B.12: Overview of the Dovetail assembly.

Design of Dovetail slot:

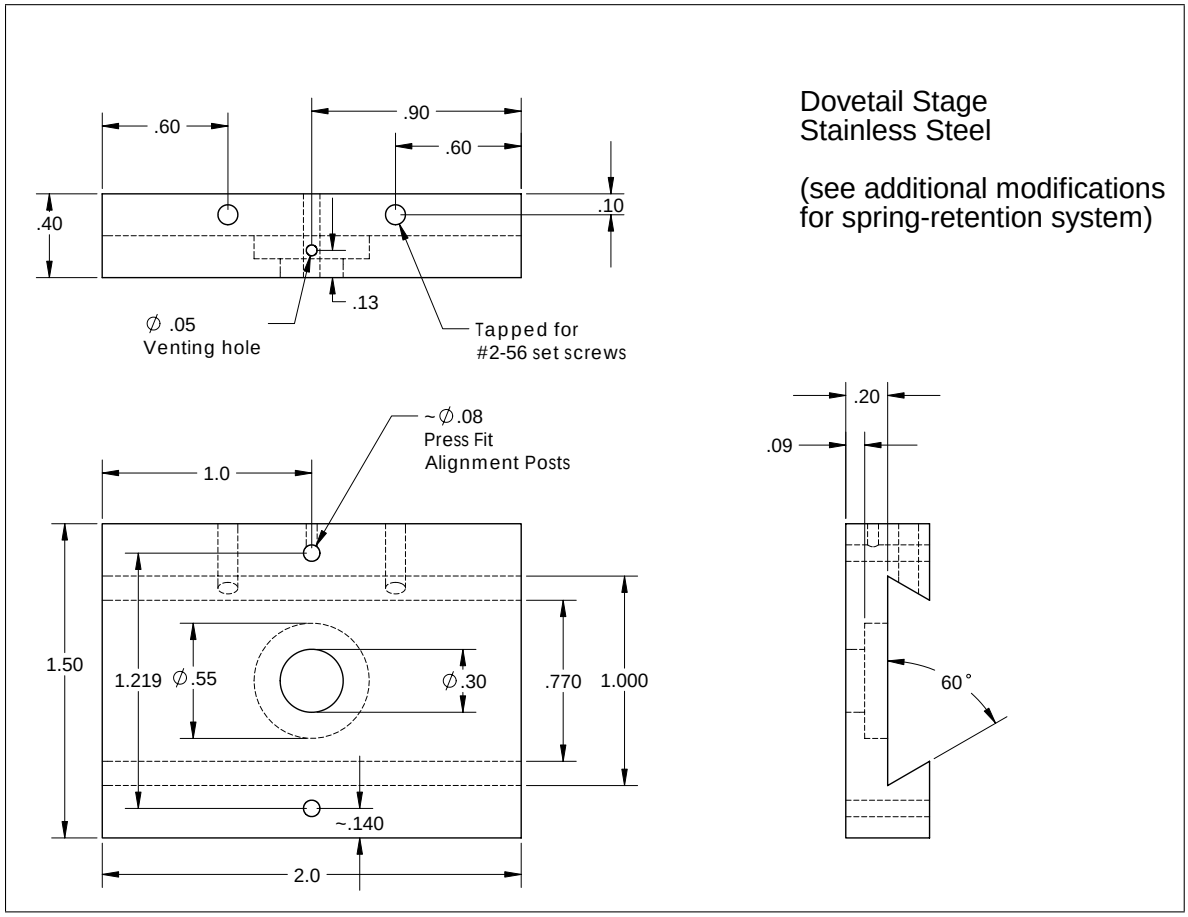

Figure B.13: Schematic drawing of the Dovetail slot. Two cylindrical posts are press fitted into the slot body to align the slot and the slot is secured in the SEM via a specially machined metric screw (see following pages).

Dovetail slot modifications:

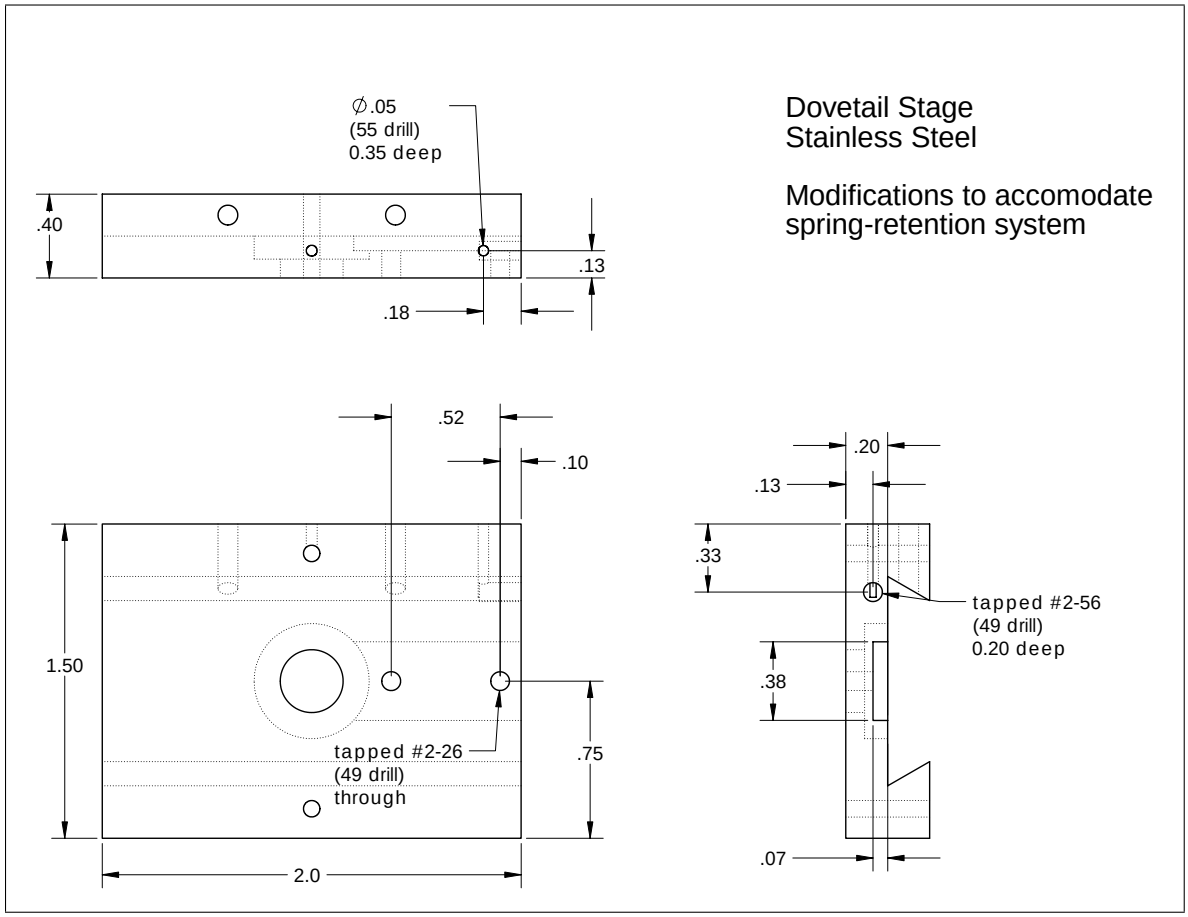

Figure B.14: Schematic drawings of Dovetail slot modifications to accommodate the spring-retention system. A beryllium copper sheet (the spring) secured to the bottom of the slot keeps the dovetail slide in place when loaded. The threaded hole nearest the edge is used to secure the sheet, while a screw in the second hole is used to prop up the sheet and provides the locking effect.

Design of Dovetail accessories:

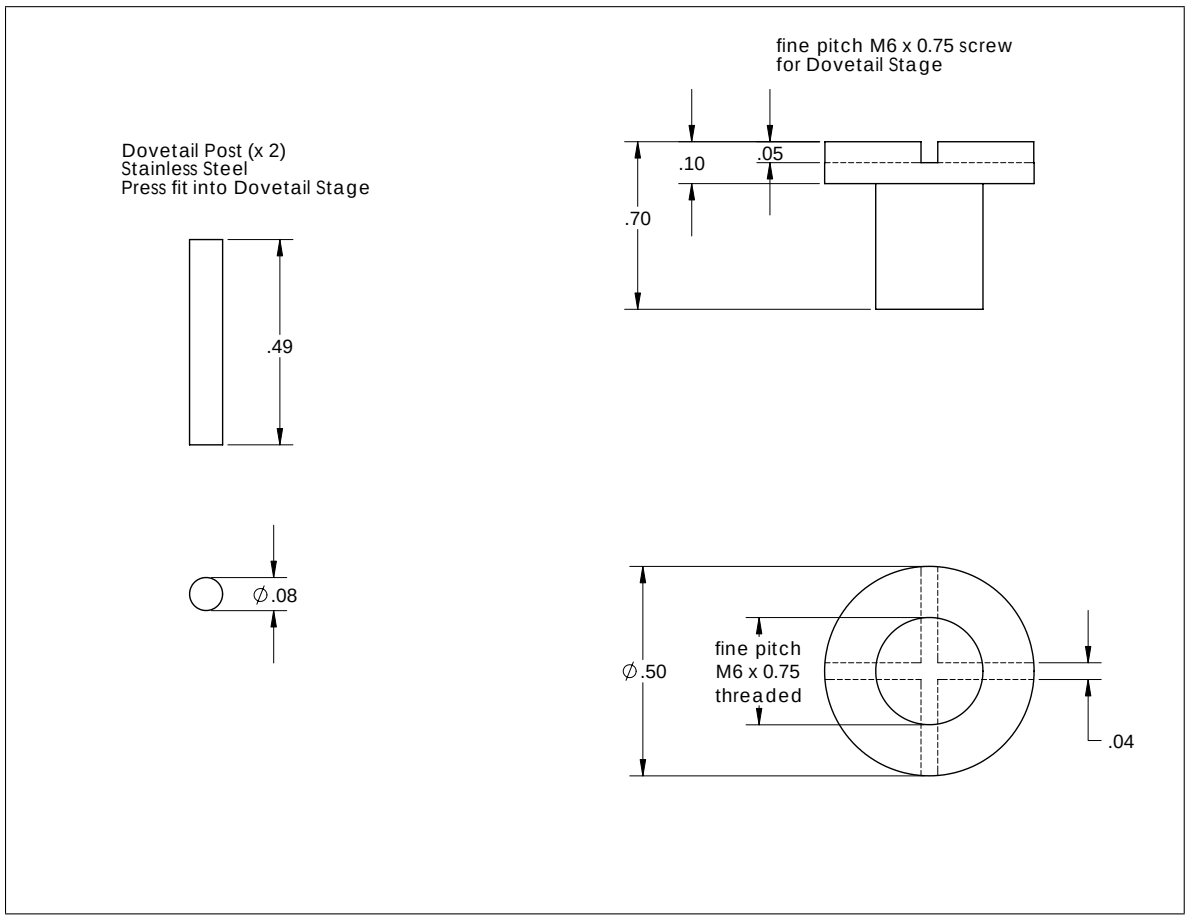

Figure B.15: Schematic drawings of Dovetail accessories. The posts align the slot with matching holes in the SEM stage. The screw secures the slot to the SEM stage.

Design of Dovetail slide for Nanomanipulator:

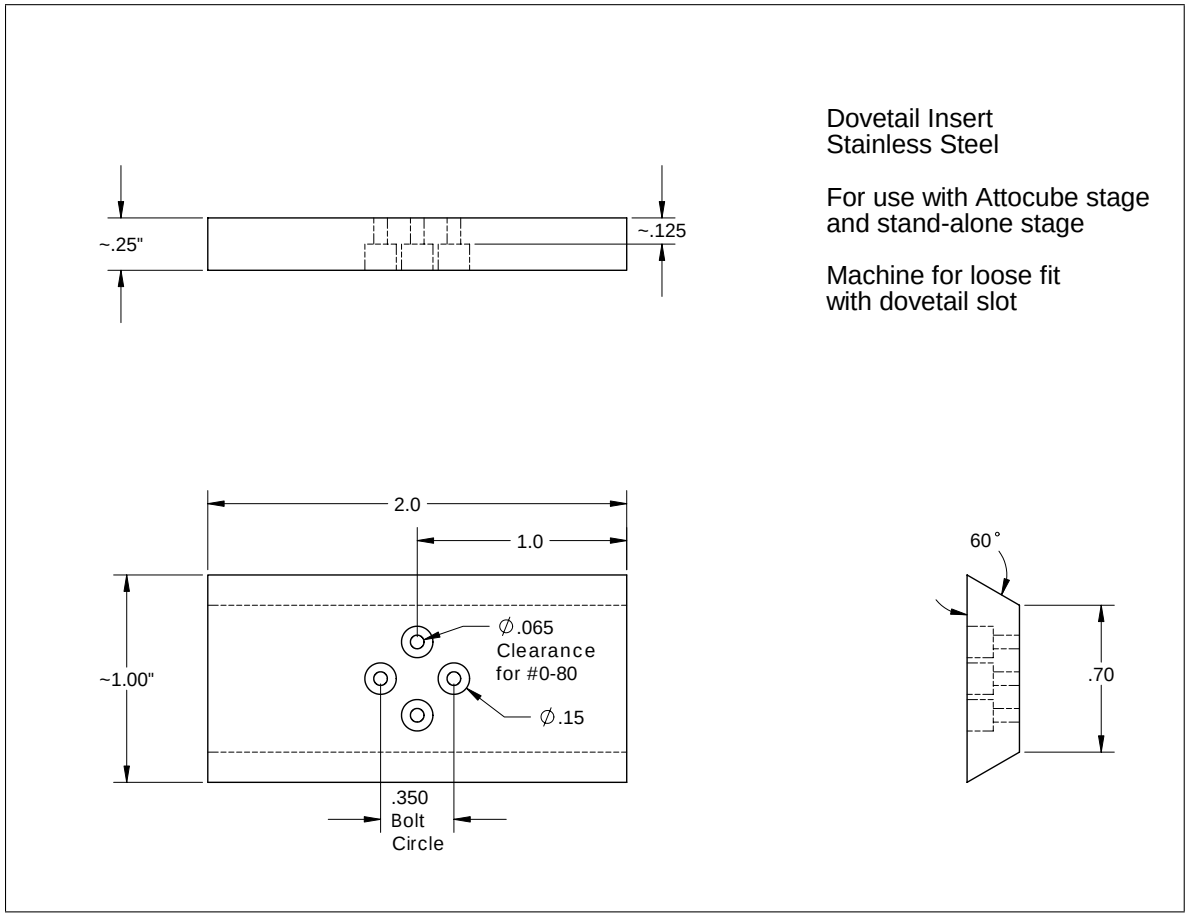

Figure B.16: Schematic drawing of the Dovetail slide used with the Nanomanipulator. Four screws secure the slide to the main body of the nanomanipulator.

Design of Dovetail slide for SEM accessories:

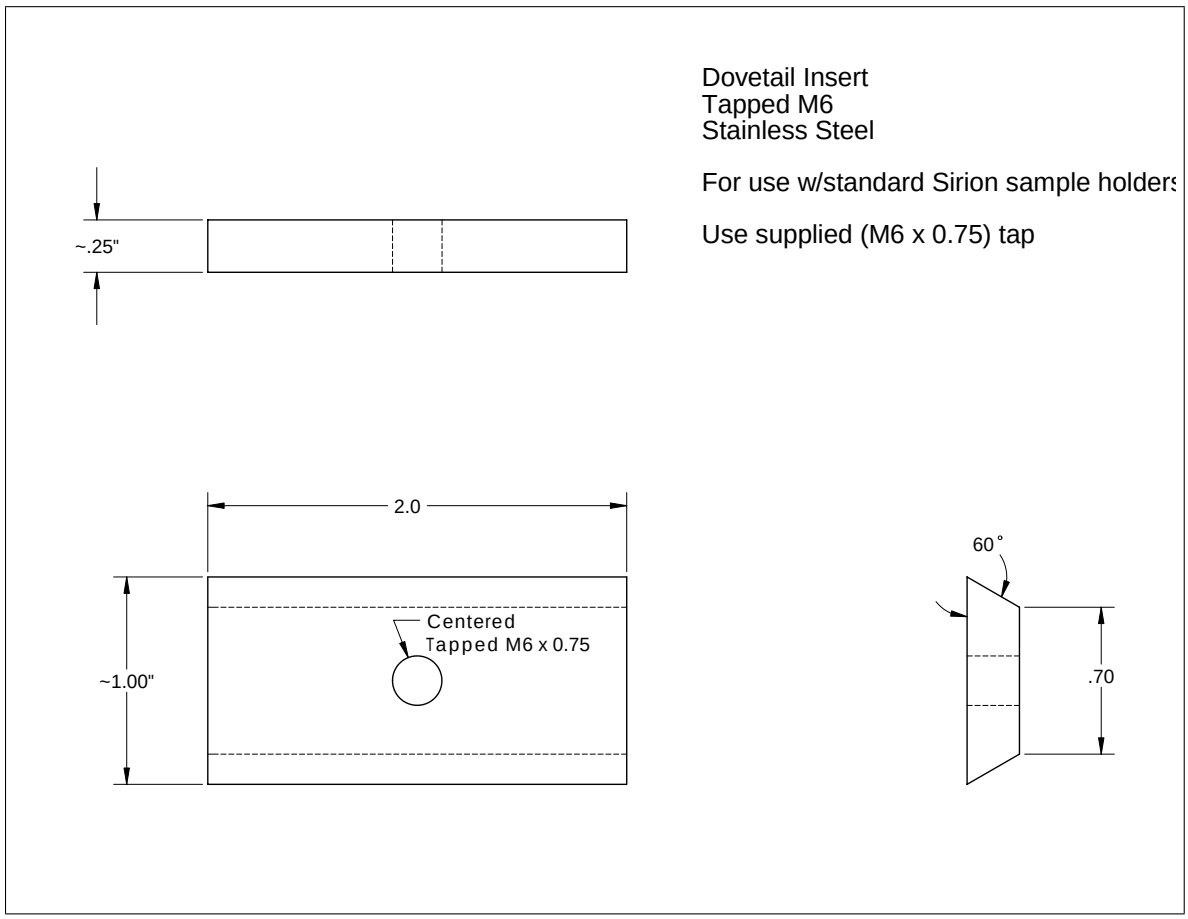

Figure B.17: Schematic drawing of the Dovetail slide for SEM accessories. The tapped hole in the center of the slide mimics the standard SEM mount and allows for use of SEM accessories without removing the Dovetail slot. This also makes SEM accessories easier to use (they can be screwed into a slide once and forever) and greatly reduces the likelihood of damage to the SEM stage.